POLITECNICO DI TORINO

Master's Degree in Mechanical Engineering

Politecnico di Torino

Master's Degree Thesis

Development of an Analytical Method for TMF of ICE Turbo Charger

Supervisors

Prof. Chiara GASTALDI

Prof. Cristiana DELPRETE

Tutor

Ing. Antonio CRUPI

Candidate

Francesco NICOLETTI

April 2024

Contents

List of Figures

List of Tables

RINGRAZIAMENTI

In primis devo un ringraziamento a tutti i miei parenti e familiari, a mio fratello Massimo e ai miei genitori Elisabetta e Giovanni per avermi dato i mezzi per arrivare fino a qui e per avermi sempre supportato con ottimismo negli alti e bassi.

Un dovuto ringraziamento alla professoressa Gastaldi e alla professoressa Delprete, per le possibilità che mi hanno offerto, per i suggerimenti e per il prezioso aiuto nello sviluppo di questo lavoro.

Un ringraziamento ad Antonio, che mi ha guidato nel mio percorso di tesi, ma anche a Michele, Daniele, Mario e tutti i colleghi presso *Dumarey* che mi hanno supportato con la loro esperienza e inesauribile disponibilità.

Grazie a Giulia, che mi supporta e sopporta nella buona e nella cattiva sorte. Che le passate avversità siano la forza per il futuro.

Un ringraziamento speciale a mio nonno Francesco e a mia nonna Liliana, per me dall'infanzia ad oggi una guida e un riferimento.

Grazie a chi c'è, chi c'è stato e chi ci sarà.

Come mi disse una cara maestra, *Ad Maiora Semper*.

1 Introduction

With increasingly competitive and demanding requirements in terms of efficiency, performance and costs, a constant effort to optimize analysis and production processes is indispensable to meet internal, market, and customer demands. It becomes essential to reduce margins of uncertainty to provide clear answers. Unfortunately, in the realm of physical phenomena, high degrees of uncertainty are inherent to the phenomena themselves, prompting the search and the development of increasingly predictive models and methods to simulate phenomena in order to reduce any real event to a simulation easily replicable at a lower cost.

A particular case is that of *thermo-mechanical fatigue* (TMF), a definition that includes a condition where we see a juxtaposition of thermal and mechanical loads. This is a case study that is different from a classical problem of isothermal fatigue and adds a level of complexity in the estimation of fatigue life. It is therefore impossible to predict with an absolute degree of certainty how a particular material behaves with given loading conditions. Failure of a component due to fatigue can have disastrous effects and is often characterized by unpredictable circumstances, due to the fact that it happens with loads often significantly lower than the breaking point of the material. Micro-structural phenomena related to thermo-mechanical fatigue only increase the risk of such occurrences.

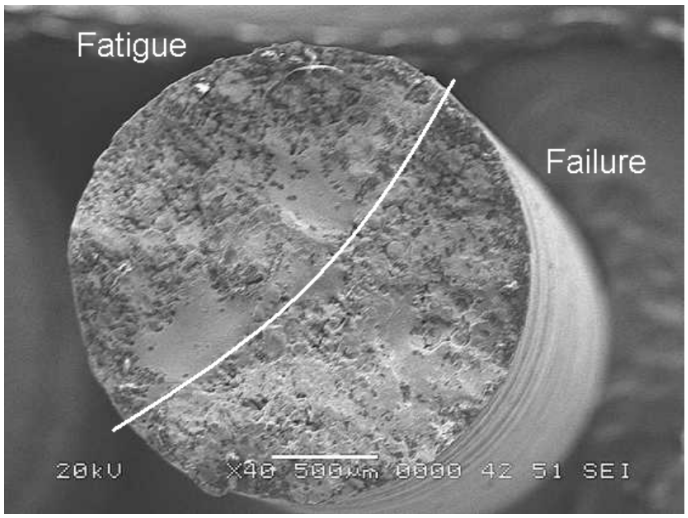

Figure 1: Crack propagation and failure zone of a cast iron test subject.

In this case, it is crucial to continuously innovate and extend the boundaries of TMF analysis in a way that is compatible with the requirements of the industry as well

as safety standards. Computer Aided Engineering tools provide the means to bring said developments forwards, and research constantly strives to better understand how certain phenomena work and the most effective ways to model them reliably. Both contributions are necessary to understanding and predicting TMF behaviour. Particularly, numerical models, such as finite element analysis (FEA), help simulate the complex stress and temperature fields within the material and predict fatigue life under different loading conditions by applying prior knowledge developed through research and testing.

This thesis work was conducted under the guidance of *Dumarey Automotive Italia S.p.A.* with the purpose of comparing different models and methods to approach the issue of Thermo-Mechanical Fatigue and develop a tool in *Python* with the purpose of employing said methods to aid the workflow of TMF analysis and guide design choices through different stages of the process.

2 Thermo-Mechanical Fatigue

Thermo-mechanical fatigue (TMF) is a phenomenon that occurs in materials subjected to cyclic loading at elevated temperatures, often in combination with fluctuating temperatures. This type of fatigue is particularly relevant in engineering applications where materials experience both mechanical stress and thermal cycling, such as in gas turbines, aerospace components, automotive engines, and power plants.

Fatigue occurs when a material undergoes cyclic loading, causing it to progressively weaken and eventually fail, even if the stress levels are below the material's yield strength. This cyclic loading induces microscopic damage in the material, such as dislocation movements, crack initiation, and propagation. In TMF, the material is also subjected to cyclic changes in temperature. These temperature fluctuations can lead to thermal stresses within the material, especially when there is a significant temperature gradient across its cross-section. The repeated expansion and contraction due to temperature changes can exacerbate existing defects or create new ones, further contributing to fatigue damage. The combination of these effects can lead to accelerated fatigue damage compared to purely mechanical or thermal loading.

High Cycle Fatigue (HCF) and *Low Cycle Fatigue* (LCF) are two distinct forms of fatigue failure that occur in materials subjected to cyclic loading. The main contributor to TMF is Low Cycle Fatigue. When talking about Thermo-mechanical fatigue, LCF mainly concerns ranges within 1 and 10^4 cycles, due to the complexity of loading types and how they interact with each other leading to several phenomena related to cyclic plasticity. LCF involves significant plastic deformation during each loading cycle, leading to the accumulation of plastic strain in the material. This plastic deformation results in cyclic hardening or softening, depending on the material and loading conditions. This is a topic that concerns the automotive field, especially in exhaust manifolds, cylinder heads and all components of an ICE that are designed to work in such harsh conditions.

This case study is focused on a turbocharger of an ICE, in particular the turbocharger casing made of a Si-Mo cast iron designed for high temperatures. The most cost-intensive key component of a turbocharger is the turbine housing that provides the kinetic energy required for charging. Inhomogeneous temperature distributions and the interaction with neighbouring components constrain the thermal expansion and contraction of the component, causing multiaxial stresses and inelastic strains during operation [1].

This chapter is thus dedicated to a discussion about the main matters concerning thermo-mechanical fatigue and all phenomena that come into play when including the effect that temperature has on the material response and behaviour.

2.1 Cyclic Response of a Material

This section describes the main phenomena concerning material response to cyclic loading in the plastic field. This is important to understand the phenomena that come into play with given loading conditions and how different models will consequently take them into account. Understanding material behaviour in the plastic field is crucial, as fatigue crack growth is mainly linked to crack tip plastic deformation [2].

The cyclic mechanism of plastic deformation may include *cyclic hardening/softening*, *ratchetting*, *mean stress relaxation* and *Bauschinger effect*.

2.1.1 Cyclic Hardening and Softening

Cyclic hardening and softening are material behaviours observed during cyclic loading, particularly in the context of low cycle fatigue (LCF) where significant plastic deformation occurs. These phenomena describe the changes in the mechanical properties of a material as it undergoes repeated cycles of loading and unloading.

Cyclic hardening refers to the increase in the stress range of the material observed after each loading-unloading cycle in LCF. During cyclic loading, plastic deformation causes dislocations to rearrange and accumulate at a grain's boundary or near other dislocations. Dislocations hinder the movement of other dislocations, making it more difficult for subsequent deformation to occur. As a result, the material exhibits an increase in strength or hardness and the overall yield stress increases. This phenomenon can result in a gradual increase in the amount of applied stress required to initiate plastic deformation and ultimately failure. This case is represented in Figure 2 (b).

Cyclic softening refers to the decrease in stress range observed after each loading-unloading cycle in LCF. Unlike strain hardening, redistribution can result in the formation of dislocation structures that facilitate easier deformation in subsequent cycles, leading to a decrease in strength or hardness. This effect results in a reduction in the yield stress and ultimate tensile strength. This case is represented in Figure 2 (a).

The cyclic hardening or softening behaviour of a metal depends on the stability of its microstructure, grain size and ageing, all dependent on the material and requires dedicated research. Temperature is another factor that influences hardening/softening, with a tendency towards softening at higher temperatures. This is relevant to TMF due to the high temperature ranges to which the material is subjected.

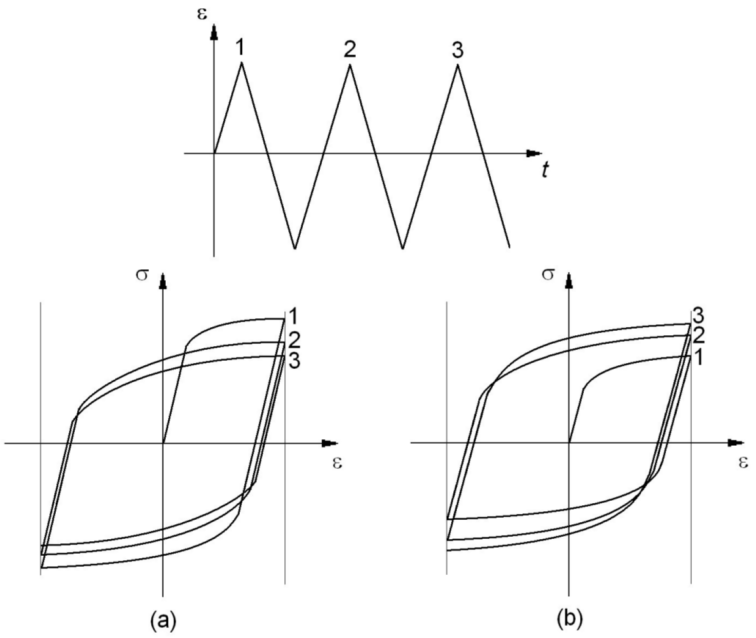

Figure 2: Cyclic softening and hardening represented in the stress-strain diagram.

2.1.2 Ratchetting

Ratchetting is a phenomenon observed in materials subjected to cyclic loading, particularly under asymmetric loading conditions. It refers to the gradual accumulation of plastic deformation or strain in a material over successive loading cycles, leading to a net increase in strain without full recovery between cycles. Ratchet strains may be composed of either time-independent plasticity or time-dependent creep [3]. This is the opposite of the previous case: when maximum and minimum stress are controlled, in case of a non-zero mean stress, a plastic strain accumulation takes place. This phenomenon decreases in magnitude after the transient cycles. Ratchetting is often associated with an increase in strain by a constant amount in each cycle, with a smaller relative increase with each cycle until the hysteresis loops reach a regime state. *Chaboche*'s kinematic hardening model is an efficient model for ratchetting prediction [4], and will be described in the section dedicated to constitutive models. Propagation occurs when accumulated ratchetting strain reaches a critical value [2].

Ratchetting will be further explored in a later chapter by the *ratchetting function* W_i, described by different models.

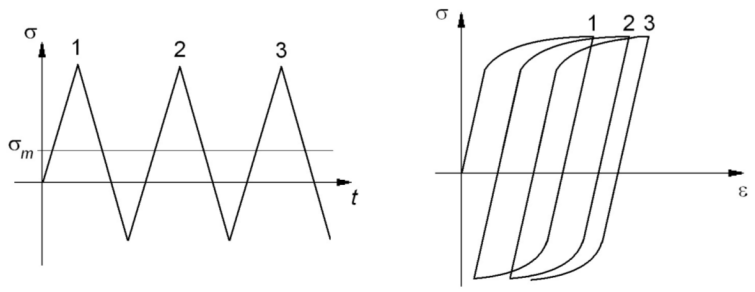

Figure 3: Ratchetting represented in the stress-strain diagram.

2.1.3 Mean Stress Relaxation

Mean stress relaxation is a phenomenon observed in materials subjected to cyclic loading, where mean stress acting on the material gradually decreases over time with fixed strain range. This occurs due to the redistribution of internal stresses and strains in the material, causing changes in its mechanical properties and behaviour.

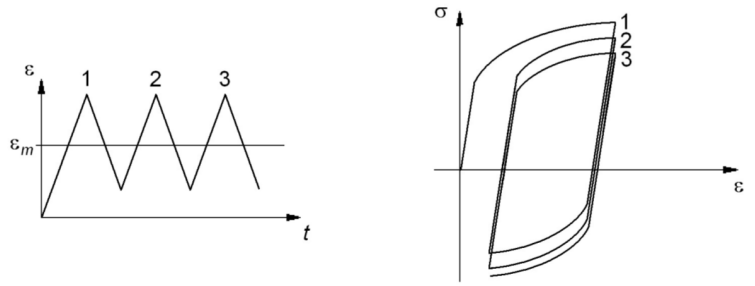

Figure 4: Mean stress relaxation in the stress-strain diagram.

Over time, the material undergoes internal rearrangement of dislocations and other defects, as well as redistribution of stresses and strains, leading to relaxation of the mean stress. This means that non-zero mean stress will shift towards zero as cyclic loadings are applied. This can lead to an extension of the fatigue life and improved durability of structures and components subjected to cyclic loading conditions.

2.1.4 Bauschinger Effect

The *Bauschinger Effect* is a mechanical phenomenon observed in materials undergoing plastic deformation. It refers to the change in material behaviour when it transitions from tension to compression without complete unloading, leading to different

mechanical responses during subsequent loading cycles. This results in a change in material properties that influences the response. The consequence is that the yield strength in the opposite direction is lower than the initial direction. Once again, this is a phenomenon that is only relevant in the plastic field.

When a load is applied beyond the elastic limit, the plastic limit in the opposite load direction is reduced, and the higher strain is above the yield point, the greater is the yield limit reduction. The *Bauschinger effect* is explained in terms of "*back stress*" where residual stresses remain in the material after unloading, influencing subsequent mechanical behaviour. These residual stresses can affect the ease with which dislocations move and rearrange during subsequent loading cycles, leading to differences in tension and compression responses.

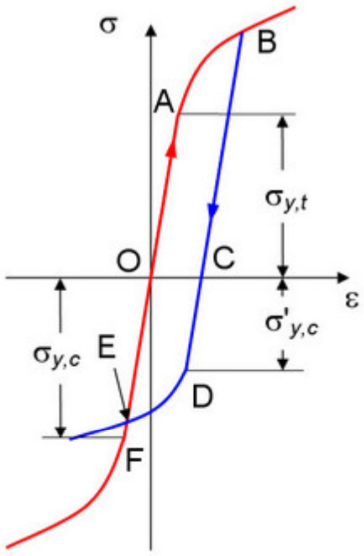

Figure 5: Bauschinger effect in the stress-strain diagram.

A possible explanation for this phenomenon comes from the *Orowan* theory, stating that during plastic deformation dislocations interact with dislocations, grain boundaries, precipitates or other obstacles. This superposition of residual stress fields generates backstress near the contact point obstructing progress of subsequent dislocations at larger distances. Stress is compressive on the side of the dislocation, and it is tensile on the opposite side. Therefore, when load is reversed, back stress repels dislocations from the obstacles in the direction of reverse strain, helping dislocations move and dropping yield stress by the same amount of the back stress. This phenomenon increases in areas with high dislocation density, as the entity of

back stress increases. On the other hand, however, more dislocations also decrease the movement of dislocations caused by pileups or cell-structures.

2.2 Influence Of Environment: Oxidation and Creep

Operating at high temperatures is often a requirement for certain components, especially in the automotive industry, where high temperatures are necessary to increase engine efficiency and reduce emissions. This introduces the issue of selecting suitable materials for such applications, as well as understanding the possible phenomena that might occur. Two of the most important ones are *Oxidation* and *Creep*, two highly complex phenomena that severely affect performance and can lead to failure. This section has the purpose to briefly introduce the topic on a theoretical level within the scope of TMF applications and in accordance with what has already been discussed in regards to the different constitutive models.

2.2.1 Oxidation

Oxidation is a phenomenon that characterizes materials subject to high operating temperatures, and it is a term that includes different phenomena that are defined by the formation of layers of compounds such as oxides or carbides.

Oxidation is a chemical reaction in which a material reacts with oxygen to form oxides. This process typically occurs at elevated temperatures and is accelerated by factors such as high temperatures, presence of oxygen, and surface defects. Oxidation is driven by the reaction between the material's surface and oxygen molecules in the surrounding environment and it operates is different steps. The basis for the reaction is the phenomenon of diffusion in the solid, where oxygen is incorporated in the metal lattice within defects, those being caused by vacancies, interstitial atoms, point and surface defects. Adsorption of oxygen atoms onto the surface of the material occurs, facilitating the reaction between atoms of oxygen and the material's atoms form oxides. This phenomenon is exacerbated by higher temperatures.

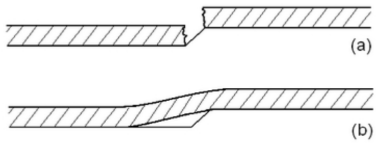

Figure 6: Oxide layer formation (b) and rupture (a).

At high temperature, oxidation results in the formation of an oxide scale on the surface. Normally, scales act as a barrier between gas and metal, protecting from

further oxidation. In TMF applications, where mechanical loads are paired with thermal loads, the continuous rupture of the oxide layer leads to potential issues causing crack nucleation and propagation. In turn, the surface exposed by the surface crack is oxidized and then fractured, repeating the cycle (Figure 6).

This is one of the leading factors that determines fatigue life at high temperatures, which is often considerably lower than fatigue life at ambient temperature. High temperature fatigue damage was shown to be caused by the growth of dominant fatigue cracks, the propagation of which results mainly from an interaction between fatigue and oxidation at crack tip. This phenomenon mainly concerns Low Cycle Fatigue, while higher frequency fatigue cycles are characterized by pure fatigue, due to the suppression of intergranular crack growth. It was shown that diffusion of oxygen is facilitated by constant tensile load [5].

2.2.2 Creep

Creep is the progressive time-dependent inelastic deformation under constant load and temperature for a prolonged period of time. It is a crucial phenomenon to keep into account when analysing thermo-mechanical fatigue, as it manifests itself at higher temperatures, in particular above a certain critical temperature. Creep occurs due to the movement of atoms or defects within the crystal lattice of a material.

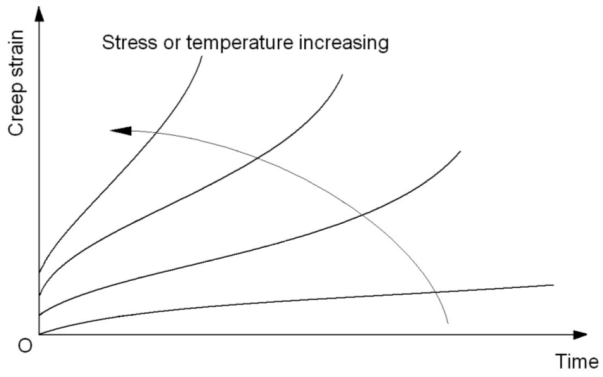

Figure 7: Creep strain over time as a function of temperature and stress.

At elevated temperatures, thermal energy enables atoms to overcome energy barriers and rearrange themselves, causing the material to deform slowly over time. This produces slow microstructural rearrangements, movements of dislocations, ageing and cavitation of grain boundaries. The primary mechanism responsible for this phenomenon is diffusion, where atoms migrate through the crystal lattice in response

to an applied stress. This movement of atoms allows the material to undergo plastic deformation even under constant stress.

Creep strain is often measured on bars subjected to constant uniaxial load that produces a curve that describes creep strain over time. The steeper the curve, the higher is creep strain over time, corresponding to a higher level of temperature with constant stress or, vice versa, higher stress at constant temperature.

The curve can be divided into three sections, defining different stages of creep:

1. The *primary creep stage* is characterized by a decreasing creep rate caused by hardening that inhibits dislocations motion, as dislocations rearrange and reach equilibrium positions. This is most relevant at lower temperatures.

2. *Secondary* or *steady-state creep stage* is characterized by an extended period that has a balance between work-hardening and recovery. The influence of stress on the secondary creep stage follows the *Norton* creep law, with the power law depending on ultimate tensile strength:

$$f(\sigma) = (\frac{\sigma_{max}}{UTS})^n \tag{1}$$

   Temperature influence on creep instead follows an *Arrhenius*-type relation:

$$f(T) = \frac{e^{-(\frac{T_{act}-T_m}{T_{max}})}}{e^{-\frac{T_{max}}{T_{mlt}}}} \tag{2}$$

   With T_m and T_{max} being mean and maximum temperatures, T_{mlt} being melting temperature and T_{act} being activation temperature [6].

3. *Tertiary creep stage* sees an acceleration of creep until fracture. This stage is characterized by an increase in strain rate and the development of localized deformation features. All three of these steps are represented in Figure 8

All these phenomena are common for most crystalline materials and happen at temperatures generally above half of the melting temperature, with the tertiary and secondary stages being more pronounced as temperature increases and failure point happens at lower values of stress.

The physical background of such behaviour reflects the processes that occur at a microstructural level, in particular:

- At lower temperatures, dislocations movement is dominated by the direction imposed by the *Burgers vector*, that describes magnitude and direction of atomic movements caused by the dislocations.

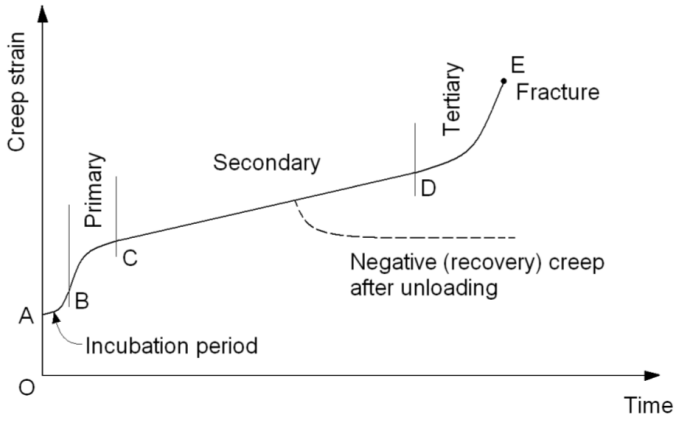

Figure 8: Creep strain over time, differentiating in primary, secondary, tertiary stage.

- At higher temperatures, *dislocation climb* is a recurring phenomenon, that being a movement of dislocations between parallel slip planes. Creep becomes more significant at higher temperatures because thermal energy facilitates atomic mobility and diffusion.

Creep phenomena require complex models and experimental tests specific to each material. In the scope of this thesis, creep is mainly discussed in accordance with the available constitutive models.

2.3 Plasticity and Visco-Plasticity Constitutive models

In order to analyse high temperature Low Cycle Fatigue, it is important to realistically simulate and predict material response to loading conditions, in particular in the case of Thermo-mechanical fatigue. The material works within the plastic field, due to the interaction between thermal and mechanical loads. The complexity of these conditions and the phenomena that might occur require specific models that can predict such phenomena when temperature exceeds certain threshold values. The purpose of this chapter is to present basic plasticity models where thermal phenomena are negligible and then go into detail with cyclic viscoplastic models. Among all models, a particular focus will be placed on the *Chaboche* model, the main reference of this thesis work when it comes to thermo-mechanical fatigue. The constitutive model applied in the FEA is based on the work of *Chaboche* and describes rate-independent elastoplasticity while elastic strains remain infinitesimal [1].

2.3.1 Classical Plasticity Theory

The theory of plasticity is used to calculate permanent deformations leaning on the *Continuum Mechanics* approach, where homogeneity is assumed on the entirety of the material. At its core, the theory aims to separate two main contributions, consisting of elastic and plastic strain:

$$\varepsilon = \varepsilon_e + \varepsilon_p \tag{3}$$

Where elastic strain is often modelled through the isotropic elasticity law:

$$\varepsilon_e = \frac{1+\upsilon}{E}\boldsymbol{\sigma} - \frac{\nu}{E}Tr(\sigma)\mathbf{1} \tag{4}$$

Plastic strain requires more complex models, mainly due to microstructural changes within the material, some of which have been detailed in this chapter. The purpose is to identify a relation between plastic strain and stress range through a *hardening function*:

$$\Delta\varepsilon_p = g(\Delta\sigma) \tag{5}$$

The classical *J2* plasticity theory, also known as the *Von Mises* yield criterion, is a widely used model for describing the plastic deformation of materials under various loading conditions. It is particularly useful for metals and other materials that undergo plastic deformation in a ductile manner. The theory is based on the concept of an equivalent stress, and it provides a simple and computationally efficient approach to capturing the yielding behaviour of materials.

The *von Mises* yield criterion is expressed in terms of the equivalent stress (σ_{eq}), which is a scalar measure of the stress state at a material point. For a three-dimensional stress state characterized by the stress tensor σ, the *von Mises* equivalent stress is given by:

$$\sigma_{eq} = \sqrt{\frac{3}{2}J_2} \tag{6}$$

With J_2 being the second invariant of the deviatoric stress tensor. The *von Mises* yield criterion states that plastic deformation occurs when the equivalent stress reaches a critical value. Mathematically, this can be expressed as:

$$f(\sigma) = \sigma_{eq} - \sigma_y \leq 0 \tag{7}$$

Where σ_y is the yield stress.

The *von Mises* yield criterion is widely used in engineering applications, especially in the context of finite element analysis, for predicting plastic deformation and failure in materials subjected to complex loading conditions. While it simplifies

the description of plastic behavior, it may not capture certain aspects of material response, such as anisotropy or specific strain rate effects, which are addressed in more advanced plasticity models like the one by *Chaboche*.

2.3.2 Plasticity Models

Plasticity models aim to capture the complex nonlinear behavior exhibited by materials under plastic deformation, including yielding, strain hardening, and the influence of loading history. The model of *perfect plasticity* is the simplest plasticity model, where the material behaves elastically up to a certain yield stress and then deforms plastically without strain hardening. It is characterized by a linear elastic region followed by a sudden transition to plastic deformation. In reality, a moltitude of factors must be taken into account, requiring the evaluation of models that predict material behaviour by including the effect of microstructural changes and cyclic loading.

Isotropic Hardening refers to a type of plastic deformation behavior exhibited by materials under stress, where the yield strength of the material increases uniformly in all directions as a result of prior plastic deformation. This phenomenon occurs regardless of the direction in which the initial deformation was applied. The concept of hardening and its mechanics was introduced in this chapter in terms of cyclic loading, and it is linked to an increase in dislocations density that in turn hinders their movement. When a material undergoes plastic deformation, its internal structure changes, causing dislocations to move and interact with each other. These dislocations impede the motion of other dislocations, thereby increasing the material's resistance to further deformation.

The isotropic hardening behavior of a material can be mathematically described using the isotropic hardening rule, which relates the increment of stress to the increment of plastic strain. The relationship is often expressed using an equation known as the *flow rule*, which governs how the stress evolves during plastic deformation. The general expression for most isotropic hardening models is in the form of Equation 8:

$$f = f_y(\sigma) - \Gamma(R) \tag{8}$$

$f = 0$ defines the flow surface, where material response is entirely elastic. f_y is the function of the yield criterion chosen and Γ is a function of the isotropic variable R. The isotropic variable is a scalar value that contributes to predict the size of the elastic domain. Figure 9 represents the size of the elastic domain in a isotropic hardening model as a function of the variables presented above.

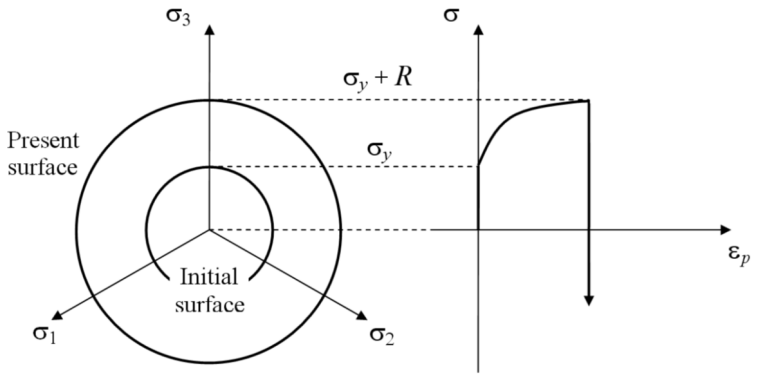

Figure 9: Size of the flow surface as a function of isotropic hardening parameters.

With the choice of the *Von Mises* flow surface model, the yield function is defined as:

$$\phi = |\sigma_{eq}| - R - \sigma_y \tag{9}$$

Where σ_y is the initial yield stress function and σ_{eq} is the equivalent stress according to *Von Mises*. Total strain flow is the sum of elastic and plastic flow:

$$d\varepsilon = d\varepsilon_e + d\varepsilon_p \tag{10}$$

With elastic flow as described in Section 2.3.1 and plastic flow described by different models.

The isotropic hardening variable can be expressed in the form of a sum of different contributions: a constant element, a linear function of plastic strain with a coefficient H and an exponential function of plastic strain with a coefficient Q_∞:

$$R_p(\bar{\varepsilon}^p) = R_e + H\bar{\varepsilon}^p + Q_\infty(1 - e^{-b\bar{\varepsilon}^p}) \tag{11}$$

Plasticity with isotropic hardening can be compared to a rheological model of stress with a spring and a friction element, as presented in Figure 10. E is Young's Modulus while R_p is the isotropic hardening variable.

Kinematic hardening, on the other hand, is a phenomenon in the plastic deformation of materials where the material undergoes permanent changes in its shape and orientation of the yield surface due to the history of plastic deformation, particularly under cyclic loading or non-proportional loading conditions. Unlike isotropic hardening, which involves a uniform expansion of the yield surface, kinematic hardening accounts for the asymmetrical nature of plastic deformation.

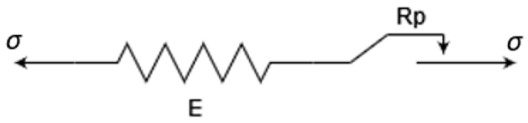

Figure 10: Equivalent rheological model, as a function of E and the isotropic hardening coefficient.

In kinematic hardening, the yield surface translates and rotates in the stress space as plastic deformation progresses. This translation and rotation capture the memory of prior plastic deformation history and affect the material's resistance to further deformation. In this case, the tensorial variable X is introduced, defining the position of centre of the flow surface.

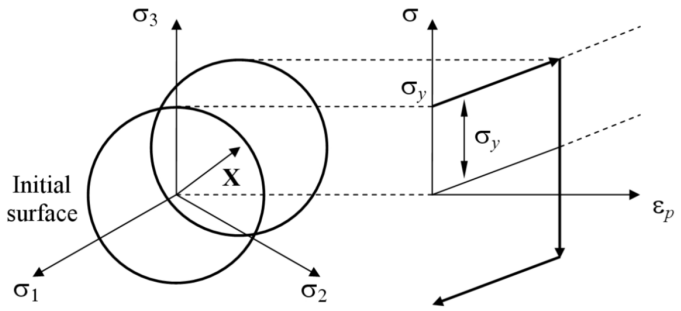

Figure 11: Size and position of the center of the flow surface as a function of isotropic hardening parameters.

Using the Von Mises criterion, the flow rule is in the form of:

$$\phi = |\sigma - \boldsymbol{X}| - R_p \tag{12}$$

The X variable can be expressed in terms of backstress α. The flow rule becomes:

$$\phi = |\sigma - \alpha| - R_p \tag{13}$$

With:

$$\dot{\alpha} = C\dot{\varepsilon}^p \tag{14}$$

Describing a linear kinematic hardening law according to *Armstrong and Frederick*, with C being the linear hardening modulus.

The equivalent rheological model therefore introduces two elements in parallel set to describe kinematic hardening, with the spring element being function of C (Assuming $\gamma = 0$ for the moment).

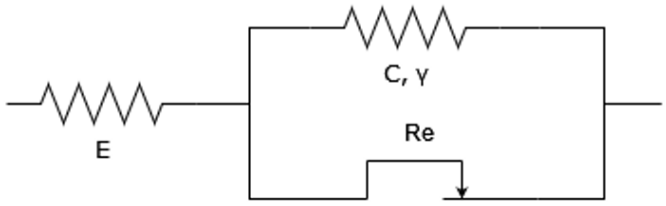

Figure 12: Equivalent rheological model, as a function of E, the constant R_e from the isotropic hardening variable and C.

Simple kinematic hardening models, however, are unable to define reverse loading and the effect of certain phenomena such as ratchetting.

Ratchetting is a phenomenon observed in materials subjected to cyclic loading under conditions of plastic deformation and creep. It involves the gradual accumulation of plastic strain over successive loading cycles, leading to incremental deformation of the material even when the applied stresses are below the yield strength. This phenomenon can result in permanent deformation or failure of the material over time. A solution is to include a term proportional to a dynamic recovery constant γ and a ratchetting function W_i.

$$\dot{\alpha} = C\dot{\varepsilon}^p - W_i\gamma\dot{\bar{\varepsilon}}^p\alpha \tag{15}$$

With W_i being a function described by different models, depending on the value of backstress and material constants. Unlike the previous one, this function is a non-linear kinematic hardening law, as it introduces an exponential term.

Isotropic hardening laws are effective in modelling *cyclic hardening* and *softening* and the *Bauschinger* effect, while kinematic hardening laws are effective in predicting *ratchetting* and *shakedown*. A *combined hardening* model includes both, with a flow rule expressed as:

$$\phi = |\sigma - \alpha| - R - \sigma_y \tag{16}$$

Including the isotropic hardening variable:

$$R_p(\bar{\varepsilon}^p) = R_e + H\bar{\varepsilon}^p + Q_\infty(1 - e^{-b\bar{\varepsilon}^p}) \tag{17}$$

As well as the backstress function from the kinematic hardening formulation:

$$\dot{\alpha} = C\dot{\varepsilon}^p - \gamma\dot{\bar{\varepsilon}}^p\alpha \tag{18}$$

2.3.3 Models for High Temperature - Viscoplasticity

Viscoplasticity models are used to describe the time-dependent deformation behaviour of materials under combined mechanical loading and thermal effects. These models are particularly relevant for materials that exhibit both viscoelastic and plastic behaviour, such as metals at elevated temperatures or subjected to cyclic loading.

The relevancy of such models is due to the existence of phenomena such as creep and oxidation, which are time and temperature dependent. It is common practice to add time dependent responses to the plasticity models already seen before.

Viscoplasticity laws are set to propose a formulation linking the evolution of viscoplastic strain with stress, as a function of a dissipation potential $\Omega = \Omega(\sigma_{eq}, T)$.

$$\dot{\varepsilon}_{vp} = \frac{\partial\Omega}{\partial\sigma} \tag{19}$$

The most important phenomenon that influences viscoplastic behaviour is creep, with its law described in Equation 20.

$$\sigma = (\frac{\dot{\varepsilon_{ss}}}{A})^{\frac{1}{n}} \tag{20}$$

A is a multiplicative factor while n is *Norton*'s exponent. This law describes stress decay during secondary creep, and n defines the slope of the curve on the $log(\dot{\varepsilon}) - log(\sigma)$ diagram describing flow rate over stress under creep. *Norton*'s creep law therefore describes the exponential relationship between strain rate and stress as a function of activation energy of creep and temperature.

$$\dot{\varepsilon}_{ss} = A_0\sigma^n e^{-\frac{Q}{RT}} \tag{21}$$

The equivalent rheological model in Figure 13 therefore introduces a viscous element characterized by the two constants of *Norton*'s law.

Figure 13: Equivalent rheological model, as a function of E, and A, n from Norton's law.

The diffusion phenomenon is the driving factor behind the formation of oxide layers on the surface. The *Arrhenius diffusion function* is derived from the *Arrhenius* equation, which relates the rate of a chemical reaction or diffusion process to temperature:

$$D = D_0 e^{-\frac{Q}{RT}} \tag{22}$$

Where D_0 is the pre-exponential factor, Q is the activation energy for the reaction, R is the gas constant and T is the temperature. Growth of the oxide layer is described by a parabolic law over time, with Q_{ox} being activation energy for oxidation.

$$h = \sqrt{K_0 e^{-\frac{Q_{ox}}{RT}}} \tag{23}$$

Hypothesizing that a *combined isotropic-kinematic hardening* state should be included, the isotropic hardening coefficient and the backstress function can be included as in the previous section.

The *isotropic hardening* variable:

$$R_p(\bar{\varepsilon}^p) = R_e + H\bar{\varepsilon}^p + Q_\infty(1 - e^{-b\bar{\varepsilon}^p}) \tag{24}$$

The *backstress* function from the kinematic hardening formulation:

$$\dot{\alpha} = C\dot{\varepsilon}^p - \gamma\dot{\bar{\varepsilon}}^p\alpha \tag{25}$$

The last phenomenon that requires modelling is the *recovery of hardening*, which is observed in materials undergoing plastic deformation, where there is a gradual reduction or recovery in the accumulated plastic strain and associated mechanical properties over time, especially during periods of rest or reduced loading. This phenomenon is particularly significant in materials subjected to cyclic loading, where recovery occurs due to climb of dislocations. In viscoplastic models, recovery of hardening is incorporated into the formulation through the evolution of the backstress function.

$$\dot{\alpha} = C\dot{\varepsilon}^p - \gamma\dot{\bar{\varepsilon}}^p\alpha - R\alpha \tag{26}$$

The complete Creep and Recovery Viscoplasticity model therefore includes all aforementioned contributions:
The *isotropic hardening* variable:

$$R_p(\bar{\varepsilon}^p) = R_e + H\bar{\varepsilon}^p + Q_\infty(1 - e^{-b\bar{\varepsilon}^p}) \tag{27}$$

Backstress function with *recovery* of hardening:

$$\dot{\alpha} = C\dot{\varepsilon}^p - \gamma\dot{\bar{\varepsilon}}^p\alpha - R\alpha \tag{28}$$

Norton's Creep law:

$$\dot{\varepsilon}_{ss} = A_0\sigma^n e^{-\frac{Q}{RT}} \tag{29}$$

The last contribution however comes from the *Chaboche* model, described in the next section, where all elements are compounded with one another, and a temperature rate term is included. This model will serve as the basis for this thesis work, necessary to characterize material behaviour in the analyses to come.

2.3.4 Unified Chaboche Model

The *Chaboche* model is a widely used material model in the field of computational mechanics to simulate the mechanical behavior of materials, particularly metals, under cyclic loading conditions. it incapsulates all models proposed above into a unified model for viscoplastic strains. *Chaboche* utilizes the formulations of *isotropic hardening* and *kinematic hardening*, but added a temperature-dependent term to the backstress function:

$$\dot{\alpha} = C\dot{\varepsilon}^p - \gamma\dot{\bar{\varepsilon}}^p\alpha + \frac{1}{C_i}\frac{\partial C_i}{\partial T}\dot{T}\alpha_i \tag{30}$$

Chaboche also introduced a further step for the *kinematic hardening* model from *Armstrong* and *Frederick*, by superimposing several models to improve prediction capabilities:

$$\dot{\alpha} = \sum_{i=1}^{M}\dot{\alpha}_i \tag{31}$$

By dividing the stable hysteresis curve in different segments, different sets of C and γ are used to improve cyclic material response. By including all contributions so far, the following equations are employed:
Stress:

$$\sigma = E(\varepsilon - \varepsilon^{th} - \varepsilon^{vp}) \tag{32}$$

Yield Function:

$$\phi = |\sigma - \alpha| - R - \sigma_y \tag{33}$$

Norton Type Power Law:

$$\dot{\varepsilon}^{vp} = \dot{\bar{\varepsilon}}^{vp} \frac{\partial \phi}{\partial \sigma} \tag{34}$$

With:

$$\dot{\bar{\varepsilon}}^{vp} = \langle \frac{\phi}{A_0} \rangle^n \tag{35}$$

Kinematic hardening with non-linear static recovery and temperature-dependent term:

$$\dot{\alpha} = C\dot{\varepsilon}^p - \gamma \dot{\bar{\varepsilon}}^p \alpha + R_i |\alpha_i|^{m_i - 1} + \frac{1}{C_i} \frac{\partial C_i}{\partial T} \dot{T} \alpha_i \tag{36}$$

With:

$$\dot{\alpha} = \sum_{i=1}^{M} \dot{\alpha}_i \tag{37}$$

and R_i, m_i being recovery coefficients.
Isotropic hardening:

$$R_p(\bar{\varepsilon}^p) = R_e + H\bar{\varepsilon}^p + Q_\infty (1 - e^{-b\bar{\varepsilon}^p}) \tag{38}$$

The equivalent rheological model according to the *Chaboche* model is detailed in Figure 14.

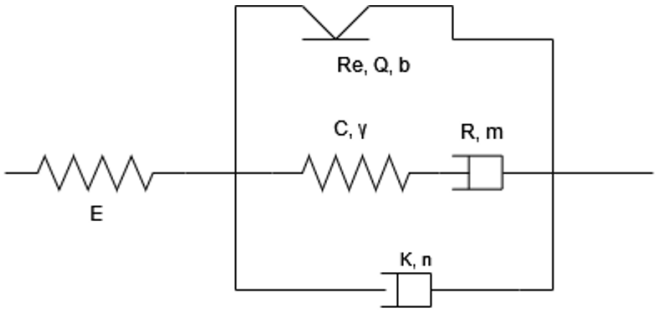

Figure 14: Equivalent rheological model according to Chaboche's constitutive model

For which:

- $K(A_0), n$ are time dependency factors.
- C, γ are nonlinear kinematic hardening factors.
- R_e, Q, b are nonlinear isotropic hardening factors.
- R, m are nonlinear static recovery factors.
- E is the linear *Young*'s modulus.

3 Damage Models

The core of TMF analysis is the estimation of fatigue life through analytical or experimental means. Decades of research were conducted with the purpose of defining accurate models to predict damage on components subjected to different loading conditions and, consequently, predict fatigue life.

Literature provides a wide array of models set to describe damage propagation with different approaches; models that are relevant to industrial applications, however, are limited in numbers, as often models are too sophisticated in their formulations or require experimental data often incompatible with industry needs. For this reason, empirical approaches or in some cases energetic approaches are often preferred to others. Two respective examples are the *Basquin-Manson-Coffin* model and the *Skelton* model, which will be discussed in this chapter.

A brief introduction on the concept of damage is however necessary. Damage in fatigue applications is a process of cycle-by-cycle accumulation in a component subjected to variable stress and strain. Loads are not large enough to cause immediate failure, but it occurs after a certain amount of cycles after damage reaches a certain threshold. *Palmgren-Miner*'s rule describes linear damage accumulation under variable amplitude load:

$$D = \sum_{i=1}^{k} \frac{n_i}{N_i} \tag{39}$$

With D being fatigue damage of the material, n_i the number of loading cycles applied at a i^{th} load level and N_i the number of cycles to failure at a certain load level. Failure is predicted when D reaches the value of 1; for different models the threshold values can be higher or lower depending on the load sequence. This is then paired with the $\sigma - N$ curve from the *Basquin* equation, returning the number of cycles:

$$N_f = \frac{C}{\sigma_a^m} \tag{40}$$

With C being a material constant and m being the slope factor of the curve.

The simplicity of this model, however, does not include thermal phenomena, including oxidation and creep. More complex models are often used for this purpose, one of them being *Neu-Sehitoglu* model for fatigue damage accumulation, which is a widely recognized approach used to predict the fatigue life and damage accumulation in materials subjected to thermomechanical loading conditions incorporating the effects of both mechanical and thermal loading on fatigue damage accumulation.

High temperature fatigue damage in *Neu-Sehitoglu*'s model consists of three parts: Mechanical fatigue damage, oxidation damage and creep damage.

$$D = D^{fatig} + D^{creep} + D^{ox} \tag{41}$$

The first contribution models damage resulting from cyclic mechanical loading as well as Thermal Fatigue, which both promote crack initiation and growth. The other two contributions model creep and oxidation phenomena. Oxidation (environment) damage is characterized repeated formation of an oxidation layer at the crack tip and its rupture. It is dependent on experimental parameters and the activation energy for oxidation. Creep damage is instead related to mechanisms such as void growth and intergranular cracking; it is at its worst when thermo-mechanical deformation is in phase, while oxidation damage is at its worst when in out of phase [7]. All contributions include material constants that characterize the material's behaviour under thermomechanical loading conditions as well as high temperature phenomena, all determined through experimental campaigns.

Within the scope of the thesis, it is difficult to keep into account the contribution of creep and oxidation due to absence of material data. As it was not possible to conduct experimental campaigns to collect said data, a different approach was necessary.

Therefore, the purpose of this chapter is to present different models designed with the end purpose of defining fatigue life. Unlike the models describe above, the focus is shifted towards uniaxial models that relate strain range directly to fatigue life in terms of fatigue cycles, such as the *Basquin-Manson-Coffin* model, rather than evaluating cumulated damage and crack propagation. This is done through different multiaxial models or criteria designed with the purpose of converting a complex multiaxial state into an uniaxial tensile state. The aim of this chapter is therefore to introduce models characterized by a simple formulation, easy implementation, and a minimal requirement of experimental parameters. This is done with the end goal of providing an analytical method for fatigue life estimation.

3.1 Multiaxial Models

As said in the introduction to the chapter, most damage models that aim to determine fatigue life through the estimation of cumulated damage are often incompatible with the industry needs. For this reason, several multiaxial criteria were designed to estimate fatigue life in LCF for mechanical components characterized by a complex stress state.

Unlike uniaxial stresses and strains, which often only characterize test subjects and experimental specimens, multiaxial tensile states define most real-life scenarios and applications. A common approach is to reduce the multiaxial tensile state to a uniaxial state, in order to be elaborated further for fatigue life estimation. Some of these models are detailed in this chapter and can be divided into two main categories:

- **Strain Based Criteria**: Developed to elaborate the different components of the strain tensor in order to obtain a single equivalent uniaxial value of strain amplitude. Some of them include *Von-Mises*, *ASME Code* and *Sonsino-Grubisic*.
- **Critical Plane Criteria**: Developed with the purpose of approaching quantities related to fatigue crack formation and propagations, analysing how normal and shear stresses and strain interact with oriented planes. These include the *Brown-Miller* model [5].

$$[\boldsymbol{\varepsilon_{ij}}] \rightarrow \varepsilon_{uniaxial,eq} \rightarrow N_f \tag{42}$$

This section details the different models that are employed in later chapter of the thesis and the basics of their functioning within the scope of this work.

3.1.1 Von Mises

The *von Mises* criterion is a strain-based model that computes strain amplitude by evaluating components of the strain tensor:

$$\varepsilon_{a,eq} = \frac{1}{(1+\upsilon)\sqrt{2}}\sqrt{[(\varepsilon_{xa}-\varepsilon_{ya})^2+(\varepsilon_{xa}-\varepsilon_{za})^2+(\varepsilon_{ya}-\varepsilon_{za})^2+\frac{3}{2}(\gamma_{xy}^2+\gamma_{xz}^2+\gamma_{yz}^2)]} \tag{43}$$

Where ε_{ia} are the normal strain amplitudes, $\gamma_{ij,a}$ are shear strain amplitudes and υ is the *Poisson* ratio. By extracting the components of normal and shear strains from a thermo-structural analysis conducted by a solver, it is possible to then utilize the single value of equivalent uniaxial strain amplitude to evaluate fatigue life as if the tensile state was uniaxial.

One drawback of the *von Mises* criterion is that it fails to distinguish between in-phase and out-of-phase loading conditions, producing the same result of fatigue life in both cases, which is often not representative of the reality. In cases where the amplitude of mechanical loads is negligible compared to the contribution of thermal loads, this drawback is not significant [5].

3.1.2 ASME Code

The *ASME Boiler and Pressure Vessel Code Procedure* is based on the *Von Mises* criterion, however it computes a component of strain amplitude by using the contribution of strain ranges calculated between two generic time instants between 0 and T that produce the maximum value of strain range:

$$t_1, t_2 \mid \Delta\varepsilon_i = \varepsilon_i(t_1) - \varepsilon_i(t_2) \rightarrow \Delta\varepsilon_{a,eq,max} \quad in \quad [0, T] \tag{44}$$

With uniaxial equivalent strain being:

$$\varepsilon_{a,eq} = \frac{1}{2} max(\frac{\sqrt{2}}{3} a) \tag{45}$$

With a including the contribution of strain amplitudes:

$$a = \sqrt{[(\Delta\varepsilon_x - \Delta\varepsilon_y)^2 + (\Delta\varepsilon_x - \Delta\varepsilon_z)^2 + (\Delta\varepsilon_y - \Delta\varepsilon_z)^2 + 6(\Delta\gamma_{xy}^2 + \Delta\gamma_{xz}^2 + \Delta\gamma_{yz}^2)]} \tag{46}$$

3.1.3 Sonsino-Grubisic

The *Sonsino-Grubisic* criterion assumes that fatigue life is related to the changing direction of principal strains and their interaction with surface deformations. This criterion evaluates elementary material planes on the surface, called *interference planes*, and their interaction with said strain components, by describing them through spherical coordinates θ, ϕ and their normal vector n. As a simplification, shear

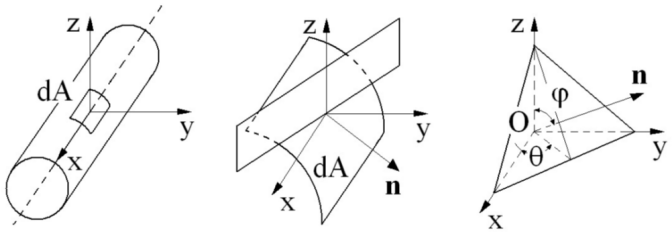

Figure 15: Interference planes

strains are calculated in the interference planes normal to the surface, corresponding to $\phi = 90°$. The criterion then evaluates shear strains as a function of spherical coordinate θ, expressed as such:

$$\gamma(\theta, t) = [\varepsilon_y(t) - \varepsilon_x(t)] sin(2\theta) + \gamma_{xy}(t) cos(2\theta) \tag{47}$$

This calculation is performed for a number of increments of θ ranging from 0 to 180°, which results in an array of shear strain values for each time increment. Afterwards, for each value of θ the maximum and minimum value of shear strain is calculated along the time discretization.

$$\gamma_a(\theta_i) = 0.5[max(\gamma(\theta_i, t)) - min(\gamma(\theta_i, t))] \tag{48}$$

The arithmetic mean of then returns a single value of shear strain amplitude:

$$\gamma_a = \frac{1}{\pi} \int_0^\pi \gamma_a(\theta) d\theta \tag{49}$$

Equivalent strain is therefore calculated as:

$$\varepsilon_{a,eq} = \frac{5}{4(1+\nu)} \gamma_a \tag{50}$$

3.1.4 Brown-Miller

The *Kandil-Brown-Miller* criterion [8], here referred to as *Brown-Miller* for brevity, aims to evaluate fatigue crack growth through cyclic shear strain and normal strain of the plane of maximum shear; the first contributes to crack nucleation while the latter favour their growth.

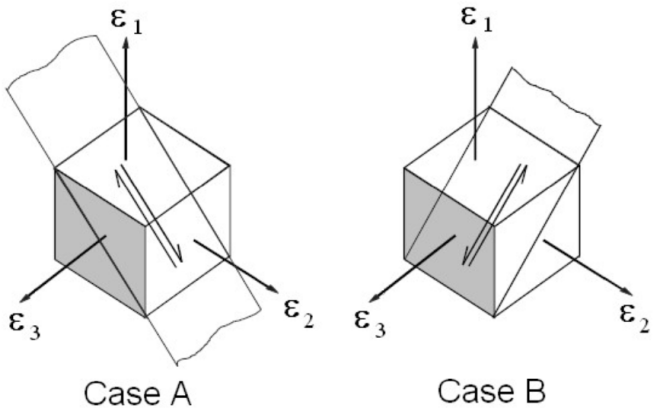

Figure 16: Different types of crack growth defined in the criterion

For this purpose, two cases of crack growth have been distinguished: The first (A in Figure 16) is typical of torsion loading, where shear stress acts on the free surface (surface in *grey*) in parallel direction to the length of the crack, with no contributions

perpendicular to the free surface (the grey arrows are parallel to the free surface), resulting in shallow cracks.

This case is caused by combined tension-torsion loading conditions or simple tension loading [5]. This is the most frequent case, and resulted in a criterion that proposes a value of equivalent plastic strain range:

$$(\Delta\gamma_{eq})^{\alpha} = (\frac{\Delta\gamma_{max}}{2})^{\alpha} + S(\Delta\varepsilon_n)^{\alpha} \tag{51}$$

With:

$$\frac{\Delta\gamma_{max}}{2} = \frac{\varepsilon_1 - \varepsilon_3}{2} \tag{52}$$

And:

$$\Delta\varepsilon_n = \frac{(1-\upsilon)\varepsilon_1}{2} \tag{53}$$

Where α and S are material constants, while ε_1 and ε_3 are the maximum and minimum principal strain according to *Mohr's circles*. For ductile materials, a simple and safer relation for ductile materials assumes $\alpha = 1$.

$$\varepsilon_{a,eq} = \frac{\Delta\gamma_{max}}{2} + S(\Delta\varepsilon_n) \tag{54}$$

The second case (B in Figure 16) is defined by shear stress that causes cracks to grow in depth and intersect the free surface (in *grey*) with an angle of 45°, with non-null shear stress components perpendicular to the surface. It can be caused by tension loading, and it is represented by:

$$\frac{\Delta\gamma_{max}}{2} = const. \tag{55}$$

Employing this model requires a modification of the *Basquin-Manson-Coffin* equation, which will be detailed in the Section 3.3 regarding Uniaxial Models.

3.2 Skelton Model

The Skelton model [9] has been developed with an energetic approach to fatigue life estimation, and requires a separate classification compared to other criteria as it uses a unique method compared to multiaxial criteria and uniaxial damage models.

This model analyses energy expenditure in terms of heat dissipated through a single cycle, which has been proved to be related to the area of a hysteresis cycle. By measuring this area, a link between dissipated energy and fatigue life can be made.

A stress-strain hysteresis cycle is a graphical representation of the relationship between stress and strain in a material subjected to cyclic loading and unloading. A relation that models cyclic response of a material within the plastic field is necessary, an example is the *Ramberger-Osgood* relation, in the form:

$$\Delta\varepsilon = \frac{\Delta\sigma}{E} + (\frac{\Delta\sigma}{A})^{\frac{1}{\beta}} \tag{56}$$

With E being the *Young Modulus*, A the cyclic strength coefficient and β the cyclic hardening exponent. Without delving excessively into the details of the model, the W coefficient known as the total energy expended at saturation can be defined from the *Ramberger-Osgood* equation as:

$$W = \sum_{i=1}^{N} \frac{\Delta\sigma_i \Delta\varepsilon_{p,i}}{1+\beta} \tag{57}$$

If the value of W is known for a specific material, it is possible to calculate the number of fatigue cycle by comparing it with the energy expenditure of a single cycle, directly related to the area of a single hysteresis cycle. The number of cycles to failure therefore is:

$$N_f = \frac{W}{w} \tag{58}$$

With w being the energy dissipated in a single cycle, which can be considered in practice equal to the area of a single cycle.

$$w = \oint \sigma d\varepsilon \tag{59}$$

In this manner, even if the complete history of the component until failure is not known, it is reasonable to approximate the contribution of a single cycle with the one from a single stabilized cycle, used as a representation of the whole history (Figure 17). The internal are of the cycle is therefore the sum of the positive (positive strain gradient) and negative (negative strain gradient) contributions along the hysteresis cycle following a clockwise rotation. By defining the hysteresis cycle as a generic function of a generic variable x, this can be summed up as:

$$\int_a^b dx = A^+ \tag{60}$$

$$\int_a^b dx = A^- \tag{61}$$

$$A_{hys} = A^+ + A^- \tag{62}$$

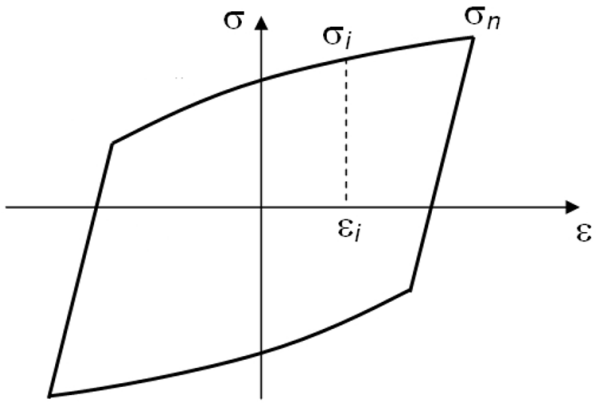

Figure 17: An example of a simple hysteresis cycle

One critical aspect of this model is the fact that thermal phenomena such as creep and oxidation as well as the contribution of mean stress are not taken into account, often producing overpredicting results. Research conducted by *Cristiana Delprete* and *Raffaella Sesana* [10] aims to improve prediction capabilities by including terms that describe mean stress and thermal phenomena. The new proposed formulation of the model becomes:

$$N_f = \frac{W}{w} f_{ms} f_{ht} \tag{63}$$

f_{ms} is the term related to mean stress in a given stabilized hysteresis cycle. A unique function for LCF isothermal regime is defined:

$$f_{ms} = \left[(1 + \eta \frac{\sigma_m}{\sigma_a})^h (1 + \xi \frac{\varepsilon_m}{\varepsilon_a})^k \right]^{-1} \tag{64}$$

Where ξ, η and h are coefficients calibrated through experimental tests.

- if $\sigma_m > 0$ or $\varepsilon_m > 0 \rightarrow f_{ms} < 1$ and fatigue life decreases
- if $\sigma_m < 0$ or $\varepsilon_m < 0 \rightarrow f_{ms} > 1$ and fatigue life increases

This is coherent with the physics of the component, as tensile mean stress has shown to be detrimental to fatigue life.

f_{ht} is the term related to high temperature working conditions, with the purpose of modelling creep and oxidation. Of the two, only creep was modelled, as oxidation was considered to be responsible for superficial crack nucleation only, rather than responsible for progressive propagation over time, that being the case for creep.

Starting from the *Norton* creep law, the influence of stress in the secondary creep stage is a power law depending on ultimate tensile strength and maximum tensile stress, while the temperature influence on creep is an *Arrhenius*-type relation depending on the activation temperature for creep. The complete formulation for the high temperature coefficient therefore is as follows:

$$f_{ht} = \{1 + \left[(\frac{\sigma_{max}}{UTS})^n \frac{e^{-\frac{T_{act}-T_m}{T_{max}}}}{e^{-\frac{T_{max}}{T_{mlt}}}} \right]^b \}^{-1} \tag{65}$$

With UTS being ultimate tensile strength, T_{mlt} being the melting temperature, T_m and T_{max} being mean and maximum temperature and T_{act} being the activation temperature for creep phenomena, approximately equal to 1/3 of the melting temperature. Last, n and b are material coefficients. This modification to the base *Skelton* model is set to improve the accuracy of results, requiring however experimental data from dedicated tests.

3.3 Uniaxial Models

Once a multiaxial tensile state has been reduced to an equivalent uniaxial value, it is possible to employ damage models specifically designed to evaluate fatigue life. The uniaxial damage model at the centre of this work is the *Basquin-Manson-Coffin model*, chosen specifically for its simplicity and wide availability of material data. This section focuses on the theory behind the models, as well as an overview of the influence that mean stress has on fatigue life estimation and the effect of temperature on the results. Calibration of experimental material data will not be discussed, as it is assumed that such information is already available before the start of the analysis.

3.3.1 Basquin-Manson-Coffin Model

The *Basquin-Manson-Coffin* model [11] (or BMC model in short) is an empirical method based on the strain-partitioning approach, which includes the separation of the contributions of elastic and plastic strain.

$$\Delta\varepsilon = \Delta\varepsilon_e + \Delta\varepsilon_p \tag{66}$$

Where $\Delta\varepsilon_e$ and $\Delta\varepsilon_p$ represent the elastic and plastic contribution of total strain respectively, both related to fatigue life. The elastic contribution to the equation was described by *Basquin*, and it characterizes HCF, where fatigue life is characterized by

a higher number of cycles (up to 10^6) and mostly elastic strains:

$$\Delta\varepsilon_e = \frac{\sigma'_f}{E} N_f^b \tag{67}$$

With σ'_f being the *fatigue strength coefficient* and b being the *fatigue strength exponent*. Both parameters are obtained through experimental tests in HCF regime.

The plastic contribution was instead investigated by *Manson* and *Coffin* for LCF applications, and describes plastic range through an exponential relation:

$$\Delta\varepsilon_p = \varepsilon'_f N_f^c \tag{68}$$

Where ε'_f is the fatigue ductility coefficient and c is the fatigue ductility exponent. Both are obtained experimentally through LCF tests.

Combining the two equation produces the complete *Basquin-Manson-Coffin* equation, describing fatigue life as a function of strain range in terms of amplitude:

$$\frac{\Delta\varepsilon}{2} = \frac{\sigma'_f}{E}(2N_f)^b + \varepsilon'_f(2N_f)^c \tag{69}$$

The simplicity and reliability of this model is its main strength, only requiring few

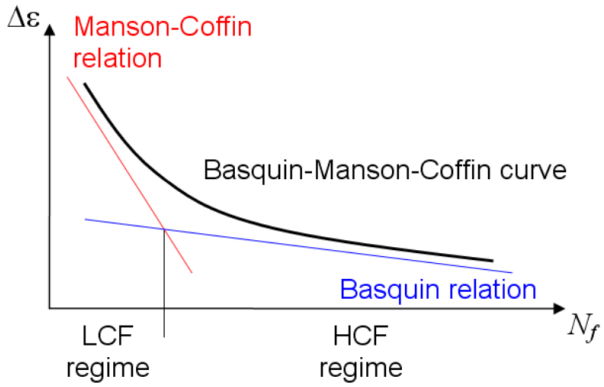

Figure 18: BMC curve on a log-log plot. The two contributions describe linear trends.

experimental parameters which have been widely documented for most material or are already available on company databases. Despite being a model designed for isothermal applications, it proved to be reliable even in the field of Thermo-mechanical fatigue, requiring however an estimation of a single equivalent temperature rather that a temperature history. The main weakness compared to more sophisticated models is the impossibility to predict certain TMF phenomena related to high temperature, such as creep and oxidation.

3.3.2 Basquin-Manson-Coffin Modified for Brown-Miller

This chapter described different multiaxial criteria capable of providing the results necessary for the execution of the BMC model, one of them being the *Brown-Miller* criteria. As was previously introduced in the dedicated section, this model requires a specific formulation of the BMC model.

As previously seen, *Brown-Miller* relates strain range to normal and shear stress, and their interaction with the interference planes.

$$\varepsilon_{a,eq} = \frac{\Delta\gamma_{max}}{2} + S(\Delta\varepsilon_n) \tag{70}$$

BMC model must be modified according to equation 71, introducing two coefficients, C_1 and C_2.

$$\frac{\Delta\gamma_{max}}{2} + S(\Delta\varepsilon_n) = \frac{\Delta\varepsilon}{2} = C_1\frac{\sigma'_f}{E}(2N_f)^b + C_2\varepsilon'_f(2N_f)^c \tag{71}$$

With:

$$C_1 = 1.3 + 0.7S \tag{72}$$

and

$$C_2 = 1.5 + 0.5S \tag{73}$$

With $S = 0.5$ if the *Poisson* ratio $\upsilon = 0.3$.

3.3.3 Influence of Mean Stress

The influence of mean stress is a non-negligible contribution to fatigue life estimation, as several studies have proved that a non-null value of tensile mean stress is detrimental to fatigue life, in opposition to a compressive state which often has the opposite effect. This section briefly introduces the fundamentals of the topic to provide the basic tools for future considerations.

Different approaches to mean stress have been explored in history, some of which including theories from *Goodman*, *Morrow* and *Smith-Watson-Topper* among many. The common philosophy among all is to find a relation linking mean stress σ_m or maximum stress σ_{max} to stress amplitude σ_a and a certain threshold limit, that being either *ultimate tensile strength* (UTS) or a certain fracture limit (σ'_f) with the purpose of defining a fatigue limit σ_D.

Smith-Watson-Topper approaches the issue with a geometric mean of maximum stress and stress amplitude:

$$\sigma_D = \sigma_a\sqrt{\frac{2}{1+R}} \tag{74}$$

With

$$R = \frac{\sigma_{min}}{\sigma_{max}} \tag{75}$$

While *Morrow* uses a threshold value of corrected fracture strength σ'_f corresponding to the parameter in the BMC equation:

$$\sigma_D = \frac{\sigma_a}{1 - \frac{\sigma_m}{\sigma'_f}} \tag{76}$$

In both cases, if mean stress in null, the fatigue limit defaults to the value of stress amplitude. To correctly employ such criteria, corrections to the BMC equation are necessary. If the base *Basquin-Manson-Coffin* model is in accordance to Equation 77:

$$\frac{\Delta\varepsilon}{2} = \frac{\sigma'_f}{E}(2N_f)^b + \varepsilon'_f(2N_f)^c \tag{77}$$

The *Morrow* criterion, for example, introduces a multiplicative term that includes mean stress:

$$\frac{\Delta\varepsilon}{2} = \frac{\sigma'_f}{E}\left(1 - \frac{\sigma_m}{\sigma'_f}\right)(2N_f)^b + \varepsilon'_f\left(1 - \frac{\sigma_m}{\sigma'_f}\right)(2N_f)^c \tag{78}$$

There are several different criteria proposed in literature, however only the *Morrow* criterion will be used in this work to account for the influence of mean stress.

3.3.4 Estimation of Equivalent Temperature

Basquin-Manson-Coffin model provides a convenient relation equivalent strains and fatigue life with the requirement of very few experimental parameters that, to this day, are widely available and documented, as well as easily obtainable with experimental campaigns. On the other hand, this simplicity means that the model is not designed to keep different temperature ranges into account. Estimating fatigue with varying temperature over time creates issues related to the estimation of an equivalent temperature that can replace the range of temperatures with a single value representative of its working conditions.

The choice of an equivalent temperature then becomes a central issue, as its choice influences material properties that in turn influence how the BMC curve behaves. In fact, all experimental parameters are highly dependent on working conditions and are obtained through separate test conducted at different fixed temperatures. For this purpose, different approaches have been compared and a new model has been proposed to try to find results that better represent target values.

The first method to estimate equivalent temperature is calculating a ***simple average*** of temperatures through every time instant.

$$T_{eq,avg} = \frac{\sum_{i=0}^{n} T_i}{n_i} \tag{79}$$

This is a simple method that allows to roughly estimate an average with a certain number of given values. This method, however, is susceptible to the number of time intervals. If the time discretization is not equally spaced as in Figure 19, or if the temperature history over time is not symmetrical, it is possible that a simple average could mis-represent the actual average.

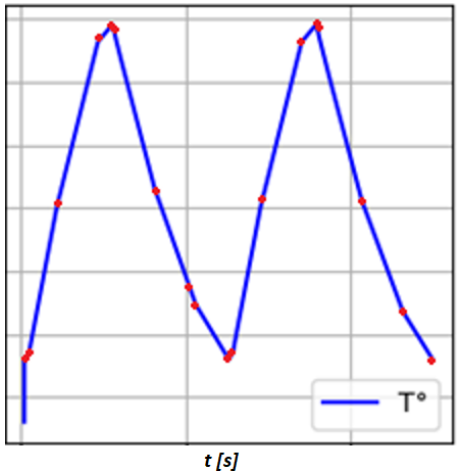

Figure 19: Example of temperature over time. Red dots represent interpolated increments. Data removed for confidentiality.

As we can see in Figure 19, it is possible to execute a linear interpolation between points identified by specific time instants. It is then possible to use this notion to calculate a different value of equivalent temperature by integrating the resulting curve.

This introduces the alternative method proposed, that being an estimation of equivalent temperature through ***integration with the trapezoid method***. The trapezoid method is a numerical integration technique used to approximate the definite integral of a function. It's based on approximating the area under the curve of the function by dividing it into trapezoids and summing up their areas. First, the time interval is divided into n subintervals of equal width, where a and b are the lower and upper limits of integration, respectively. Within each subinterval, the method approximates the curve by a straight line connecting the function values at

the endpoints of the interval. These straight lines form trapezoids when combined with the x-axis. The area of each trapezoid is calculated using the formula for the area of a trapezoid:

$$A_i = \frac{h}{2}(f(x_i) + f(x_{i+1})) \tag{80}$$

where h is the width of each subinterval, x_i and x_{i+1} are the x-values at the endpoints of the subinterval, and $f(x_i)$ and $f(x_{i+1})$ are the corresponding function values.

Finally, the areas of all the trapezoids are summed up to get an approximation of the definite integral:

$$\int_a^b f(x)dx \approx \sum_{i=1}^{n} A_i \tag{81}$$

This method provides more accurate results, as it better represents the actual average temperature. In fact, it calculates the average on the whole curve rather than on the single points. In this way, it is less likely that certain "ranges" of the time discretization that have time intervals much closer to each other (such as when there is a change in gradient) do not influence the average value excessively.

3.3.5 The Taira-Based Method

An alternative approach was also considered in this thesis, and a new potential model has been designed, based on the existing *Taira* damage model.

The approach followed by *Taira* includes several experimental tests to explore the correlation between thermal fatigue and isothermal low cycle fatigue at high temperature, to establish a method for life prediction in variable temperature fatigue by using data from isothermal low cycle fatigue [5] [12]. Due to fatigue, an increment of damage $\Delta\Phi$ is cumulated during one half of the plastic strain range is proportional to plastic strain and $\lambda(T)$, a function of temperature:

$$\Delta\Phi = \lambda(T)(\Delta\varepsilon_p)^n \tag{82}$$

Fatigue damage per cycle is given by the sum of $\Delta\Phi$ during heat-up ($T_1 \to T_2$) and $\Delta\Phi$ during cooldown ($T_2 \to T_1$). When cyclic temperature $\Delta T = T_2 - T_1$ is below a certain threshold value T_t, approximately equal to 1/3 of the melting temperature of material for cast iron and representative of the activation temperature for creep, the n coefficient is equal to 2, and:

$$\lambda(T) = \frac{1}{T_2 - T_1}\int_{T_1}^{T_2} \lambda(T)dT \tag{83}$$

With equivalent temperature being close to the mean temperature of the cycle between T_1 and T_2.

$$T_{eq} = \frac{T_1 + T_2}{2} \tag{84}$$

if ΔT is above the threshold value, the equation becomes:

$$\lambda(T_{eq}) = \frac{1}{T_t - T_1} \int_{T_1}^{T_t} \lambda(T) dT + \frac{\lambda(T_2)}{2} \tag{85}$$

With equivalent temperature being equal to the maximum temperature T_2 of the cycle.

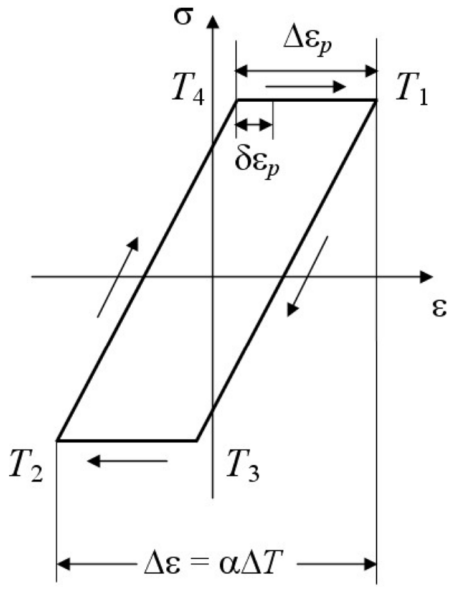

Figure 20: Stress-Strain diagram at different levels of temperature.

The damage model described was not used in this thesis work. However, the idea of using a threshold value of temperature to simulate certain physical phenomena has been applied with a similar interpretation, by extending the reasoning behind the model to each time increment. With the knowledge of temperature values at each time instant rather that the maximum and minimum values T_1 and T_2 only, the principle of imposing that a certain time instant has a value of temperature equal to the maximum temperature registered if the average of two subsequent increments is above the threshold T_{th} is the basis for this method. In short:

$$T_{eq,Taira} = \frac{\sum_{i=0}^{n} T_{i,eq}}{n_i} \tag{86}$$

With:

$$T_{i,eq} = \begin{cases} \frac{T_i + T_{i+1}}{2} & with \quad T_{i,eq} < T_{th} \\ T_{max} & with \quad T_{i,eq} > T_{th} \end{cases} \tag{87}$$

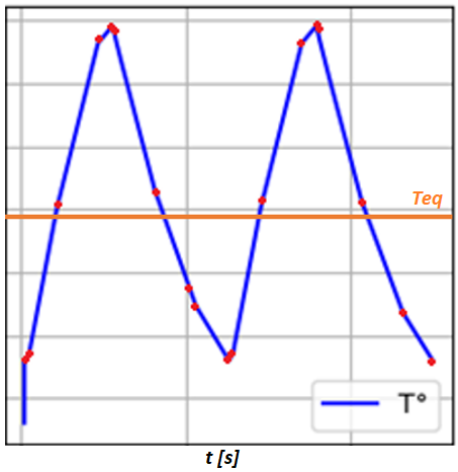

Figure 21: Example of temperature over time. Red dots represent interpolated increments, orange line represents threshold value T_{th}.

The necessity for such a method arises after certain considerations have been made regarding the accuracy of the proposed value of equivalent temperature: The assumption that an average of values in time is representative of the equivalent temperature implies that the results of the BMC model are equal to another analysis conducted at a constant temperature that is equal to the equivalent one. The result of this analysis is highly sensitive to temperature due to the fact that BMC parameters are dependent on this value. In general, higher temperatures up to a certain point allow for higher values of stress before failure due to the material being more ductile. This is true even for the case of variable temperature, where higher strains are observed at high temperatures due to thermal expansion. During a test cycle, however, there could be a long timeframe where temperature is low and strains are absent, but still decrease the overall average value of temperature of the cycle. By assuming a value of equivalent temperature that is too low, there is the risk of incorrectly estimating fatigue life as if a certain range of stress and strain had been achieved at a lower value, producing a more conservative estimation. For the way it is designed, this *Taira*-based model will almost always produce values of equivalent temperature that are higher of a simple arithmetic average, compensating for the issue described. Last but not least, the threshold temperature from the *Taira* model provides a mean to

include oxidation phenomena in fatigue life estimation, with it being a direct estimate of the activation temperature for creep phenomena.

This method, as detailed in *Chapter 8*, has shown promising results when compared to benchmark values and has been widely used in this thesis work, although requiring experimental future tests and comparisons to prove its accuracy. In the future, further validations of this method will be necessary and a more accurate comparison with the other two approaches and a given benchmark is required to prove its reliability.

4 Thermo-Mechanical Analysis

Thermo-mechanical analysis is a sophisticated engineering discipline that integrates principles from thermal and structural analyses to comprehensively investigate the coupled effects of temperature and mechanical loading on materials and structures. This multi-physics approach is paramount in understanding and predicting the behavior of materials subjected to varying thermal environments and mechanical stresses. Thermo-mechanical and thermo-structural analysis are particularly crucial in industries such as aerospace, automotive, and material science where components experience diverse operating conditions.

Thermo-mechanical analysis relies on the principles of *continuum mechanics*, which treat materials as continuous and deformable mediums. The analysis considers the interplay between mechanical deformation and heat transfer within a material or structure. It addresses the impact of temperature changes on material properties, thermal expansion, and the consequent effects on structural integrity. Numerical techniques, particularly the *Finite Element Method* (FEM), are integral to thermo-mechanical analysis. FEM discretizes complex structures into smaller elements, facilitating the solution of the coupled field equations. This approach allows for accurate simulations of real-world scenarios, capturing localized effects and providing insights into the thermal and mechanical response at different points within a structure.

4.1 Aim of the Analysis

The aim of this chapter is to conduct a *transient thermo-structural analysis* of components from an already commercialized engine. Transient analysis examines the time-dependent evolution of temperature and mechanical stresses and therefore provides results that describe the component's behaviour over a given period of time. It is therefore necessary that input data is managed accordingly to this requirement and that certain parameters are dependent on time. Most of the material at disposal (in terms of files, data and models) were kindly made available by *Dumarey Automotive Italia S.p.A.* and for the most part are derived from a previous TMF analysis that was conducted internally in 2019 on the same engine components for purposes similar to this work. The results of this analysis will be used as a benchmark and, for brevity, from now onwards it will be referred to as "*2019 Analysis*".

Thermo-Mechanical Fatigue analysis includes the process of simulating thermal and mechanical loads as well as estimating fatigue life. This thesis work focuses exclusively on the performance of a single component of the engine block, that being the turbine volute of the turbocharger, utilizing surrounding components as a mean

to provide accurate boundary conditions to the system.

4.2 Available Material

As briefly stated in the introduction for this chapter, all data necessary for the analysis was already made available, allowing this work to be mainly focused on the core of the issue of fatigue life estimation. Some elements, however, were significantly modified to fit the scope and purpose of the thesis. Before describing all available data, a brief description of the source material from which this data has been extracted is necessary.

4.2.1 "2019 Target" TMF Analysis

A report from 2019 conducted internally by colleagues at *Dumarey* has been used as a reference to extract target values for the methods and models proposed here. The report compares fatigue life estimation with traditional methods (Such as the estimation of plastic equivalent strains or "*%PEEQ*") with the commercial tool for fatigue life estimation *TFAT* applied to the aforementioned engine that will remain unnamed in this thesis for confidentiality reasons. The analysis was conducted on the entirety of the *engine block*, *cylinder head*, *turbocharger* and *after-treatment* but focused its results on the turbocharger, in particular on the *turbine volute* and fatigue life on its surface. The report identified critical points on the volute and evaluated life fatigue cycles, comparing the different methods, and evaluating their accuracy. The different points scrutinized and their target values will be detailed in a later chapter. The point to discuss here is in relation to the complexity of the 3D model and the changes that must be made to fit the scope of the thesis. The results from the *2019 analysis* were obtained by computing on the entire model, composed by hundreds of single components, requiring a significant amount of resources, which translate in dozens of hours of computation time. To make future analyses more flexible, several components not directly linked to the turbine volute were removed and boundary conditions were set at their place. This resulted in a 90% decrease in the number of elements, reducing computation time significantly but introducing a margin of error. This change requires a full rework of the mesh geometry as well as radical changes to the lines of code that describe the relations between different elements. Such changes will be detailed in the next section.

4.2.2 Available Data

Most data was acquired from the launch files of the 2019 analysis, and it includes:

- **Mesh Geometry files**: A mesh geometry, in the context of computational modeling and simulation, refers to the discretized representation of a physical domain using a collection of simple geometric elements. The file has the *inc.* format and it is designed to be used in *Hypermesh*. This file as it was available includes all components of the engine analysed in the *2019 report*.

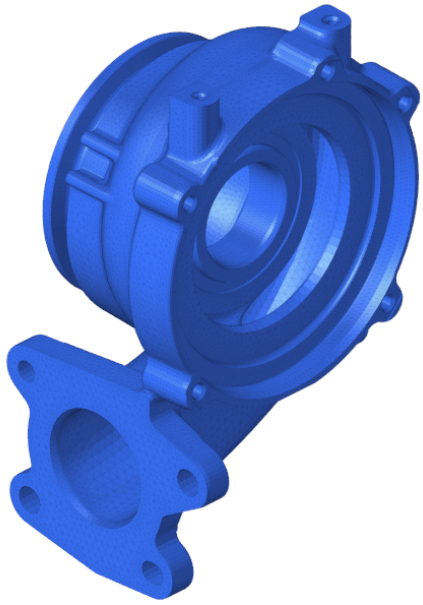

Figure 22: Mesh Geometry of the Turbo volute, isolated.

- **CFD Analysis results**: Results of the CFD analysis conducted on the whole engine. These results can be used to produce a temperature map even on a single element of interest.
- **Amplitudes over time**: A text file containing information regarding the time dependency of the output values of the temperature and HTC map produced by the CFD analysis.
- **Material data cards**: A text file containing material properties and their association to each component. There are different properties defined for thermal and for structural analysis, both for viscoplastic and *Chaboche* constitutive models.
- **Contact pairs file**: A text file containing information on the interaction

between contact surfaces of every element. Contacts behave differently in thermal and structural analysis and require changes for each.

- **Water jacket subroutines**: Pieces of code in *Fortran* language that aid the solver in computing the behaviour of water in the cooling ducts of the cylinder head.
- **Launch files**: The main launch file that calls back to every other file and defines all steps of the process.
- **Numerical target results**: Numerical results of the TMF analysis conducted by *Dumarey Automotive Italia* in 2019 on the same engine. Such values were used as a target and benchmark for this thesis work.

4.2.3 Available Resources

For the execution of this work, different resources necessary for obtaining the results preliminary to the analyses carried out were made available by *Dumarey Automotive Italia S.p.A.* These are listed and described below:

- **Altair Simlab**: A simulation and CAD environment with fluid dynamics analysis tools. The use of this software was limited to defining a mapping of gas temperature and heat exchange coefficient inside the turbine. This was possible through data provided by previous CFD analyses.
- **Hypermesh**: A CAE software with finite element simulation and modeling tools. The software where much of the preparatory work for the analysis was focused. Starting from a model of a "*Piston Head - Turbo - After-treatment*" group already complete with mesh, it was necessary to narrow down the scope of the analysis and prepare the model for subsequent thermal and structural analyses.
- **Abaqus (Dassault Systems)**: A finite element analysis software to simulate stress, deformation, heat exchange, and other phenomena. It was the software primarily dedicated to resolving thermal and thermo-structural analyses, and subsequently, through the extension of *Abaqus Viewer*, to post-processing data and acquiring the results necessary for the script's operation.
- **Anaconda - Spyder**: Anaconda is a distribution of the *Python* language aimed at simplifying the management of resources and tools, including *Spyder* which is a compiler developed in *Python* and dedicated to the *Python* language. It is the tool that allowed the script to be developed.

All these tools were used in various orders throughout the duration of the project, with the aim of continuously improving the accuracy of the initial model and better correlating it with the available numerical results.

4.3 CAD Model and FEM Analysis

Finite Element Analysis (FEA) is a powerful numerical technique used in engineering and applied sciences to simulate and analyse the behaviour of complex structures and systems under various loading conditions. It is a mathematical method that divides a complex physical system into smaller, simpler subdomains, known as finite elements, enabling the approximation of its behaviour through numerical computations. FEA has become an indispensable tool in the design, optimization, and evaluation of structures and components across a wide range of disciplines, including mechanical, civil, aerospace, and biomedical engineering.

At its core, FEA is based on the principle of discretization, which involves breaking down a continuous structure or system into a finite number of interconnected elements. Each element is represented by a set of mathematical equations that govern its behaviour, and the entire system is described by a system of algebraic equations. These equations are then solved numerically to obtain approximate solutions for the system's response to external stimuli, such as forces, pressures, or temperature changes.

4.3.1 CAD Model and Mesh Generation

The first step in FEA is to create a geometric representation of the structure or system being analysed. This involves defining the physical dimensions, shapes, and material properties of the components. Advanced computer-aided design (CAD) software is often employed for accurate and efficient geometry modelling.

Once the geometry is defined, it is discretized into smaller elements. The mesh generation process divides the structure into finite elements, such as triangles or quadrilaterals in 2D analysis or *tetrahedra* and *hexahedra* in 3D analysis. The accuracy of the analysis depends significantly on the quality of the mesh. Mesh quality is highly dependent on the size and density of elements. Smaller elements provide a more accurate representation of complex geometries and behaviours but come at the cost of increased computational demands. Element size must be carefully chosen to balance accuracy and computational efficiency. Local refinement can be applied to critical areas, ensuring a higher density of elements where necessary.

Tetrahedral meshes play a significant role in *finite element analysis* (FEA), particularly in three-dimensional simulations where they are used to discretize complex

geometries. Tetrahedral elements, commonly referred to as *tetrahedra*, are simple geometric shapes with four triangular faces, four vertices, and six edges. Their simplicity, combined with their ability to represent irregular and intricate structures, makes them a popular choice for a wide range of engineering applications.

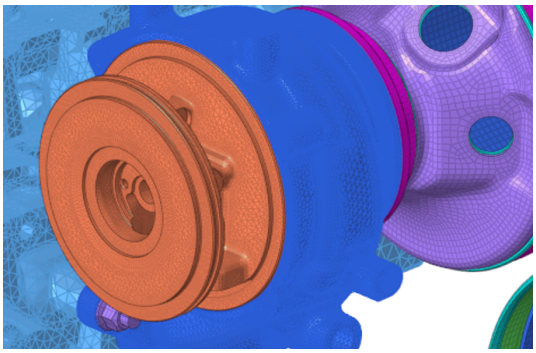

Figure 23: Component geometry with meshes made visible. Certain elements are hidden for confidentiality reasons.

A *tetrahedron* is the simplest 3D element, characterized by four nodes or vertices and four triangular faces. Each node represents a point in space, and the geometry within the tetrahedron is defined by linear interpolation between these nodes. Higher-order tetrahedral elements, such as quadratic or cubic tetrahedra, allow for more accurate representation of complex deformations by introducing additional nodes. the nature and order of these elements will play a key role in the preparation of different types on analyses.

First order elements are characterized by linear interpolation functions. This results in a relatively coarse representation of the solution compared to higher-order elements. First-Order Elements have nodes only at the vertices of each tetrahedron. **Second-order elements** have curved edges, allowing for more complex geometrical representation within each element. The interpolation functions are quadratic, providing a more accurate approximation of the solution compared to linear elements. Besides the vertices, they have additional nodes along the edges (called midside nodes), resulting in a total of 10 nodes per tetrahedral element in a second-order mesh.

This is particularly relevant in defining the difference between the type of meshes used in thermal and structural analysis. Each element of a mesh is defined in *Abaqus* by a label composed by two parts. The first part defines the type of element used (Diffusive or structural) and the second part defines the order of the element. For example, a **DC3D4** element is a 3D *diffusive* element (DC3) of the first order (D4).

In both thermal and structural analysis, first and second order elements are used. The difference, however, is found in the type of element.

- **Thermal analysis** uses *diffusive* elements, such as **DC3D4** (First order) and **DC3D10** (Second order). These elements are designed to model the diffusion of heat within a material or across different materials. Thermal analysis focuses on how temperature distributions evolve over time due to heat transfer mechanisms such as conduction, convection, and radiation.
- **Structural analysis** uses *structural* elements, such as **C3D4** (First order) and **C3D10** (Second order). Structural elements are intended to simulate the behaviour of mechanical structures subjected to loads and constraints. Structural analysis deals with stresses, strains, displacements, and deformations in solid bodies due to mechanical loads, including tension, compression, bending, and torsion.

In this case study, the mesh geometries for the components to be analysed were already available from the launch files of the *2019 analysis*. It was however necessary to make several changes to fit the scope of the project.

4.4 Preparation of Thermal Analysis

Materials respond to temperature variations through thermal expansion, phase changes, and alterations in thermal conductivity. Thermal Analysis examines how these responses influence material properties, such as *Young*'s modulus, thermal conductivity, and coefficients of thermal expansion. This knowledge is fundamental in predicting how materials will deform and conduct heat under different thermal conditions.
The files necessary to launch the analysis are listed and described here:

- **Mesh Geometry**: Mesh generation is not the focus of the work, but a model complete with Meshes was made available from which to start the analysis. The model provided is part of a set consisting of all engine components from cylinder head, turbo, and after-treatment, but it was necessary to modify the model to focus on the turbo volute and a few surrounding elements. Tetrahedral meshes are DC3D4 diffusive first order elements and DC3D10 diffusive second order elements. The "*.inc*" type file can be imported in *Hypermesh*, which was used to isolate the turbo volute, all surrounding components and their contact surfaces. All unnecessary components were deleted.

- **CFD analysis**: Results file of a CFD analysis of the flow inside the component, carried out at different engine speeds representative of two diametrically opposed regimes; the use of these files will be detailed in Section 4.5.
- **Time amplitudes**: File containing information on the amplitude of the quantities obtained in the gas mapping for each time instant. This is necessary to set a working regime during the analysis.
- **Material cards**: File containing the elastoplastic properties of materials, such as elastic modulus, *Poisson*'s ratio, $\sigma - \varepsilon$ curve, thermal expansion coefficient, and conductivity, all varying with temperature. Each material is then associated to a component. After the removal of all unnecessary components, the file was modified in a way that excluded all elements that were no longer necessary.
- **Contact Pairs File**: File containing information on contacts between model surfaces. In thermal analysis, it is important to define the bond between surfaces where conductive heat exchange occurs; in particular, pairs of surfaces were coupled with a "*Small Sliding*" contact. After the removal of unnecessary elements, this file was heavily reworked in a way that excluded contact pairs between elements that no longer existed.
- **Subroutine files**: Subroutine files for boiling water in the water jackets. Subroutines are *Fortran* language pieces of codes that work at runtime with the solver, perform actions in parallel with the solver, in this case, calculate convective exchanges of fluid in the cylinder head water jackets and model radiation phenomena (*Stefan-Boltzmann*).
- **Launch files for thermal analysis**: The main launch file containing the lines of code to be provided to the solver to specifically complete the thermal analysis. It contains information on initial data and environment, imports the aforementioned files, defines convective exchange surfaces, distinguishes the various steps of the analysis specifying the extent of discretization, and specifies the required outputs. It also defines the different steps corresponding to the two possible transient regimes, those being the Heat-up transient regime and the Cooldown transient regime, each repeated two times. After the removal of unnecessary elements, it was heavily reworked to exclude functions that were no longer required.

The **test cycle** used as the basis of the transient analysis was defined according to the internal specifications for experimental tests. The entity of time and temperature

measurements was removed for confidentiality reasons but in general terms the cycles follow the trend defined by:

- **Heat up transient regime**: repeated twice, with the second one being representative of the stabilized cycle. Also referred to as "*peak power*", it represents a situation where the engine works at high rpm and produces its peak power output.
- **Cooldown transient regime**: also repeated twice, with the second one being representative of the stabilized cycle. Also referred to as "*motored*", it represents a situation where the engine works at low rpm.

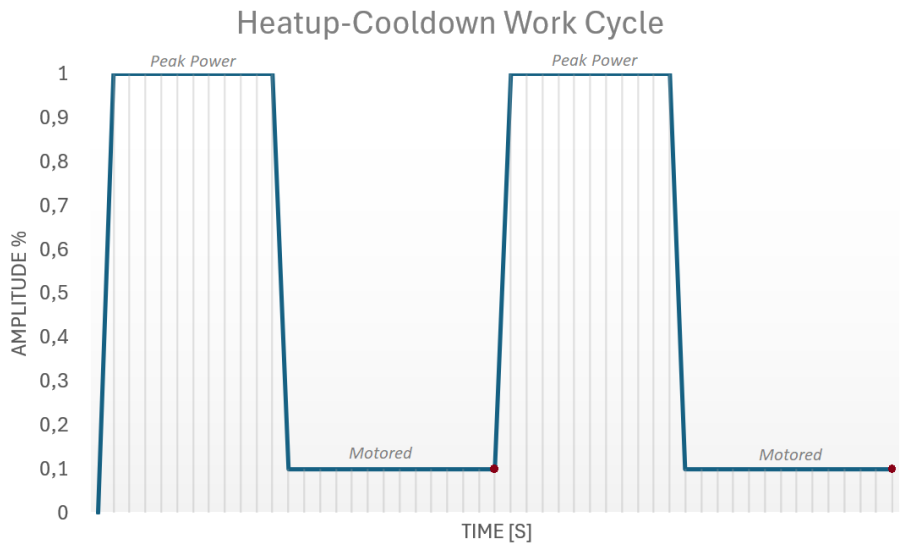

Figure 24: Heat-up - Cooldown cycle described in terms of normalized amplitude.

The first heatup-cooldown cycle will be ignored when computing TMF results, but it is necessary to prepare the stabilized cycle regardless of the initial conditions. The cycle of interest is therefore the second cycle which from now onwards will be referred to as "*Stabilized Cycle*".

Figure 24 is representative of the sequence of the two regimes over time. This graph was shown as a reference to better visualize the test cycle over time. It is important to note that this cycle is only representative of the working conditions of the engine. The actual input that defines how the gas behaves depending on time is given by the CFD analysis and the values of temperature and heat transfer coefficients (HTC) in each point, mixed with the values given by the "amplitudes" card, which

defines the normalized amplitude of said values over time, therefore defining the actual accurate test cycle over time.

4.5 Gas Mapping

An input required for the completion of the thermal analysis is the result of the CFD analysis computed along the surface of the volute, producing a set of values on every node of the surface.

The starting point is the definition of a surface of contact between the component and the exhaust gas. This is done through the functionalities of *Hypermesh*, allowing the user to extract and export a layer of tetrahedral meshes composed only of those elements in contact with the gas. Once this operation is done manually, the result is shown in Figure 25 and will be referred to as "*gas skin*". Once this is completed,

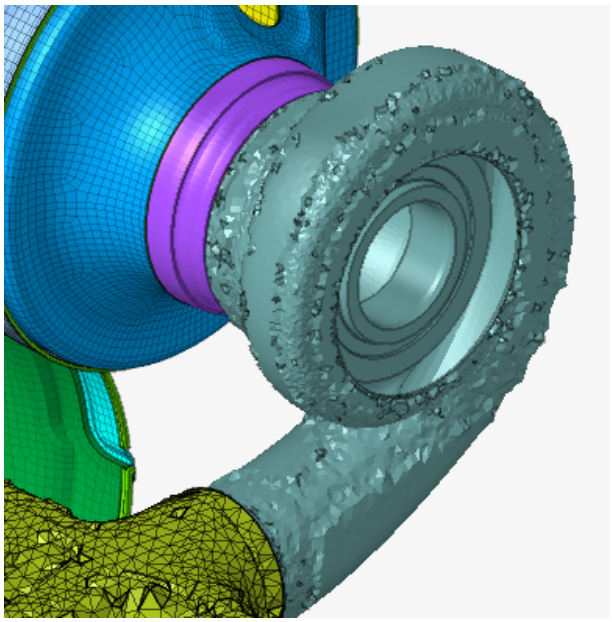

Figure 25: Gas skin.

Simlab is then used. Input data is composed by the "*gas skin*" and two different files, one from the "*peak power*" and one from the "*motored*" regime, that contain the results of previous CFD analyses on the same component. By applying these results exclusively to the component of interest, it is possible to extrapolate the "gas map" over the surface of the volute.

In other words, the values of temperature and HTC for every point on the surface are mapped and printed in two different files. Visualizing said values of temperature for the two different regimes produces Figure 26 and 27. Numerical data are confidential.

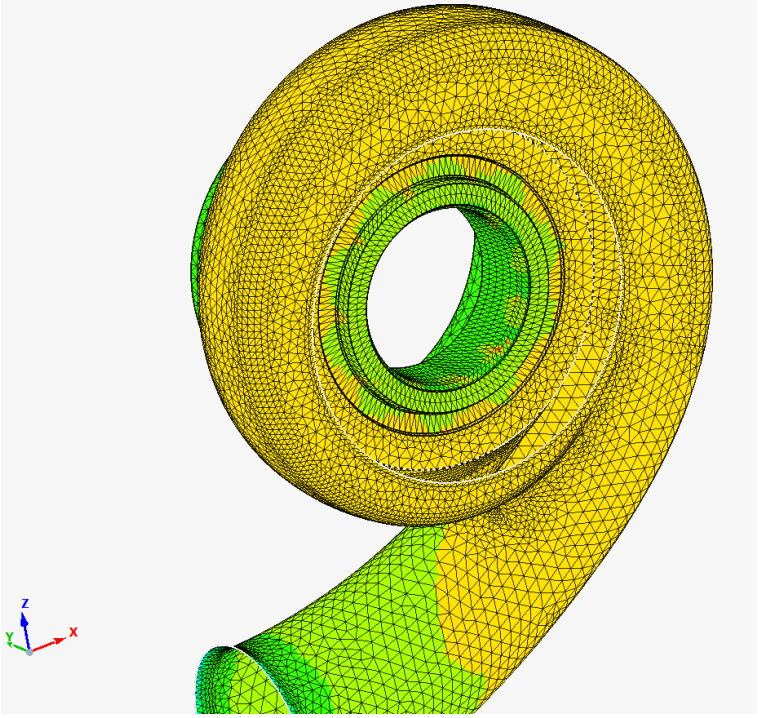

Figure 26: Temperature during heatup.

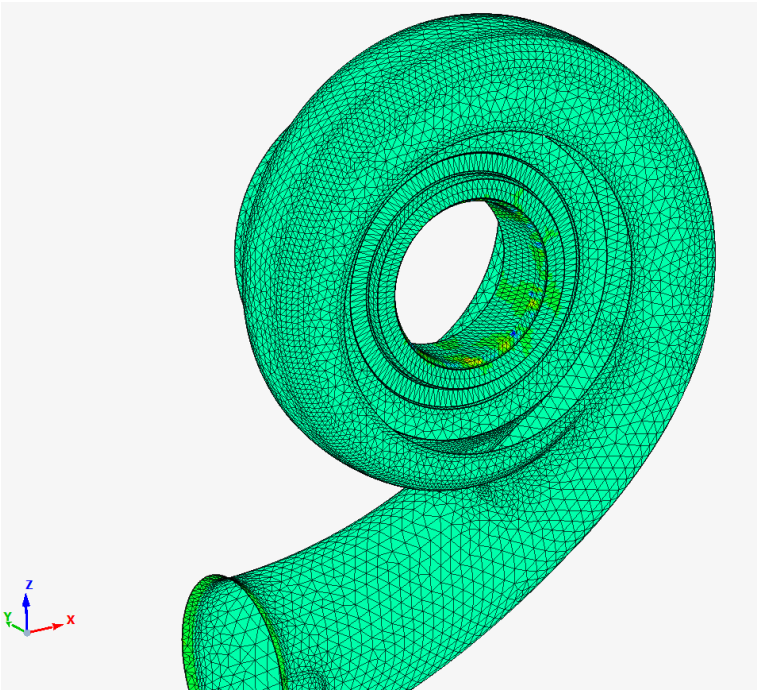

Figure 27: Temperature during cooldown.

For the heat transfer coefficients, results are shown in Figures 28 and 29 :

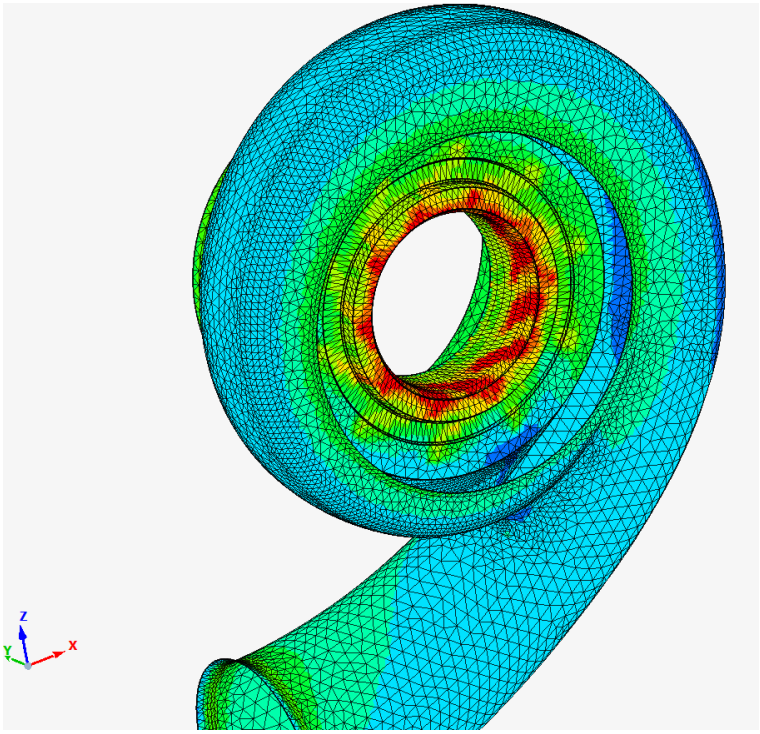

Figure 28: HTC during heatup.

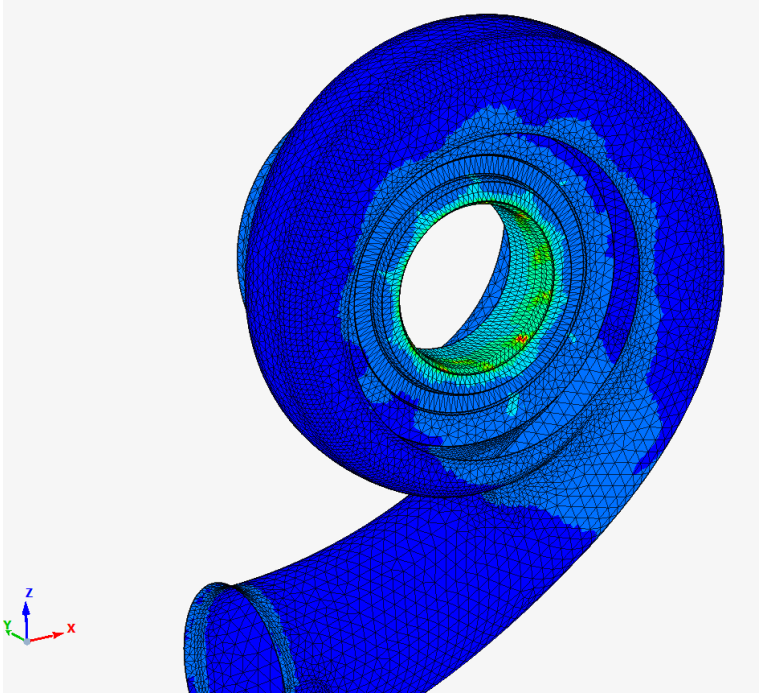

Figure 29: HTC during cooldown.

It is interesting to note already that the peaks in values of HTC are located in the cylindrical surface adjacent to the turbine blades, likely due to the consistent convective phenomena that occur in an area where gas is in close contact with the surface and in turbulent motion due to the present of the turbine blades.

Therefore, it is possible to predict that this area will be the one most susceptible to variations in temperature and could experience higher degrees of variation of temperature over time.

4.6 Thermal Analysis

Once all necessary files are gathered, *Abaqus* was used as a solver to compute the result of the transient thermal analysis. Once completed, the software returns a file with the "*.odb*" extension that can be interpreted by a post-processer to visualize results. For this purpose, *Abaqus Viewer* served as a post-processer to view results. This allows the user to visualize a heat map of the variable of interest superimposed on the geometry of the component for every time instant of the discretization.

For clarity, the only results shown in Figures 30 and 31 refer to the very last time

instant of the heat-up phase and to the very last instant of the cooldown phase:

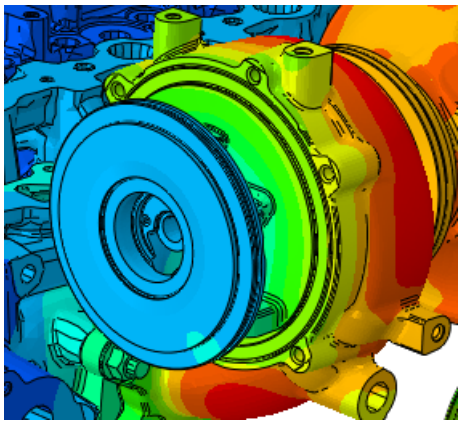

Figure 30: Temperatures at the end of Heat-up transient phase. Data removed for confidentiality.

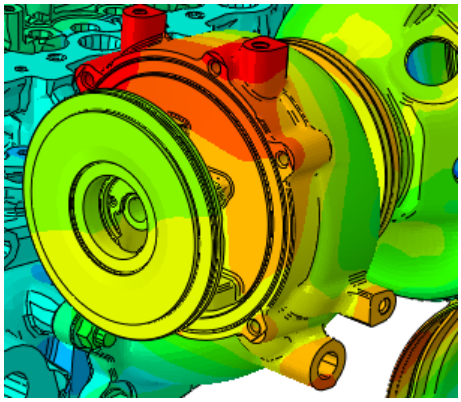

Figure 31: Temperatures at the end of Cooldown transient phase. Data removed for confidentiality.

Out of every component, the one that is of interest is the turbo volute in figure 32 and 33: The areas that are subjected to the highest variation in temperature are

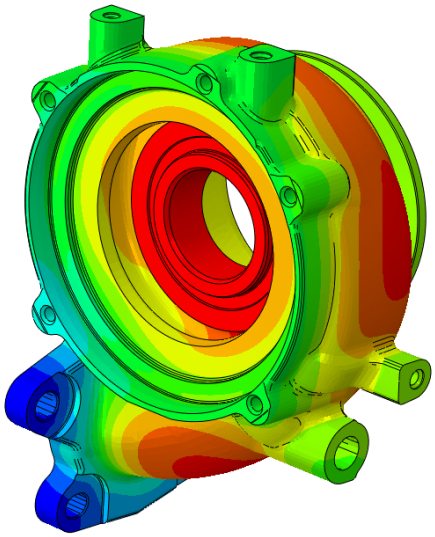

Figure 32: Temperatures at the end of Heat-up transient phase. Data removed for confidentiality.

the ones located on the inner surface of volute; particularly, the cylindrical surface adjacent to the turbine blades and the "tongue region" are characterized by higher temperatures at heat-up and lower temperatures at cooldown. These regions are expected to be among the ones subjected to the highest loads.

By isolating a single node in this region and by plotting temperatures, we can observe its variation over time in Figure 34.

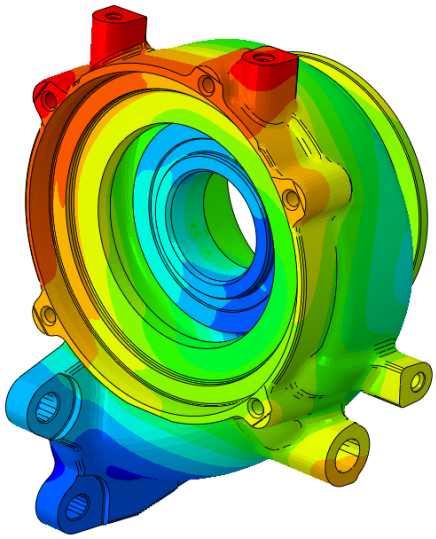

Figure 33: Temperatures at the end of Cooldown transient phase. Data removed for confidentiality.

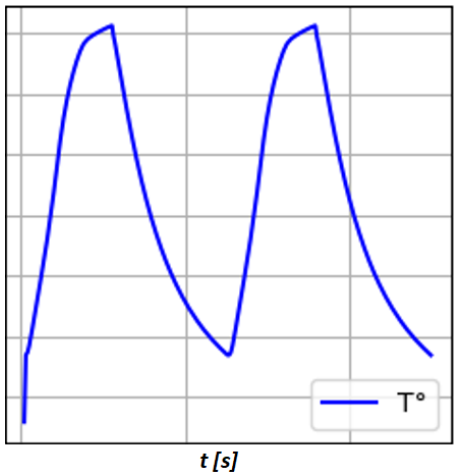

Figure 34: Temperatures over time as a result of thermal analysis.

4.7 Preparation of Thermo-Strucutal Analysis

Materials often exhibit nonlinear behaviour under combined thermal and mechanical loading. Nonlinear material models, accounting for phenomena such as plasticity, viscoelasticity, and phase transformations, are employed to accurately represent material response in TMF. These models are essential for capturing the intricate interactions within complex materials. In this case study, data files containing information with respect to elastic, plastic and viscoplastic material behaviour were made available, as well as a material card that contains the results of *Chaboche*'s constitutive model applied to the material of the turbo.

In the specific case of this analysis, the main source of stress for the component is represented by the cyclical trend of temperatures and the resulting deformations. The mechanical stress source is solely represented in this case by the pre-tensioning of the bolts on the head-turbo connection flange. However, this is a constant load that does not have a cyclical trend. In practice, therefore, the thermo-structural analysis is more oriented towards a purely thermal analysis. Nevertheless, in a professional context, the analysis is still commonly referred to as *thermo-structural* out of habit and for clarity.
The starting elements available for the analysis are detailed as they follow:

- **Mesh geometry**: Starting from the same geometry that was previously used in the thermal analysis, the model is modified in order to prepare the thermo-structural analysis. In particular:

    1. Constraints are added to the model to ensure its static equilibrium and boundary conditions. *Hypermesh* tools are utilized to define constrains in a specific direction. In particular, to constrain the system in a hyperstatic manner while still ensuring free deformation, a combination of constraints **A**, **B**, and **C** with different degrees of freedom has been employed. Constraint **A** is restricted along *X, Y, Z* axis; Constraint **B** is restricted along X and Z; Constraint **C** restricted along Z. Additionally, to simulate the presence of other components at the edges of the outermost elements of the assembly, an axial constraint (Dir. Y) has been applied to the surfaces of these elements theoretically in contact with other components that are actually excluded from the model. This allows radial sliding while imposing an axial constraint (see Figure 35).
    2. The type of finite elements composing the mesh is modified. While in the thermal analysis, diffusive elements DC3D4 and DC3D10 (first and second-order 3D diffusive elements) were used, in the structural analysis,

structural elements of type **C3D4** and **C3D10** (first and second-order 3D structural elements) are employed.

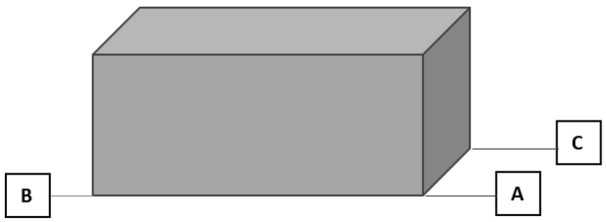

Figure 35: Schematics of engine block and location of its boundary conditions.

- **Material Properties Cards**: File containing the elastoplastic properties of materials, such as the elastic modulus, *Poisson*'s ratio, material properties, all varying with temperature. Each material is then associated with a component. In the case of a card based on the *Chaboche* constitutive model, the coefficients of the model are also reported, for example cyclic hardening, as well as the $\sigma - \varepsilon$ curves calculated with the model.
- **Contact Pairs File**: File containing information about the contacts between the surfaces of the model. In structural analysis, it is crucial for establishing the mechanical interaction between two surfaces and defining the zones of *Coulomb*'s contact where loads are transmitted. In particular, a distinction is made between *fixed contact* or *small sliding* contact, which allows relative movement between surfaces. It is important to ensure the stability of each component without any uncontrolled sliding.
- **Launch Files**: Main launch file containing the lines of code to be provided to the solver. It includes information about the initial data and environment, imports the aforementioned files, defines the convective exchange surfaces, distinguishes the various steps of the analysis by specifying the discretization entity, and specifies the required outputs. Unlike the thermal analysis, the total number of steps is 8, as it includes 4 preliminary steps dedicated to pre-tensioning the bolts and an initial heating aimed at activating the contacts between the surfaces.

4.8 Thermo-Structural Analysis

The output of the analysis carried out once again in *Abaqus* is a file with the extension '*.odb*' that can be interpreted in *Abaqus Viewer* for post-processing of the data. With

this result, the thermo-structural analysis phase ends, and we then proceed to the post-processing of the results.

Depending on the outputs requested in the launch file, it is possible to visualize a color-map for several different results, such as:

- **Stress components**: If requested, the solver can produce a color-map that describes stress components along *X, Y* and *Z* axis. This data can be then acquired for every node of interest and for every time increment. This numerical value is necessary for future calculations of fatigue life.

- **Equivalent stress**: The solver can produce the numerical result of equivalent uniaxial stress according to the *Von Mises* principle in every node for every increment of time.

- **Strain components**: If requested, the solver can produce a color-map that describes strain components along *X, Y, Z* axis. This data can be then acquired for every node of interest and for every time increment. Alternatively, the solver can calculate components of *logarithmic strain*, defined by Equation 88:

$$\varepsilon_l = ln\left(\frac{l_0 + \Delta l}{l_0}\right) \qquad with \qquad \varepsilon = e^{\varepsilon_l} - 1 \tag{88}$$

  Strain and Logarithmic strain are similar for smaller deformation but differ for deformations usually higher than 2%. This numerical value is necessary for future calculations of fatigue life.

- **Max. and Min. principal strains**: The solver can produce a color-map describing maximum and minimum principal strains according to *Mohr's circles*, those being the intersection of the circles with the x axis.

- **Temperatures**: Similarly to thermal analysis, temperatures in every node and for every increment of time can be visualized. This numerical value is necessary for future calculations of fatigue life.

In the case of thermo-structural analysis, visualizing data is an important component of post-processing, as it allows the user to have an instant visual feedback of potential failure points based on the requested output in order to make first-try assumptions about the quality of certain design choices.

Potential choices for values to acquire are equivalent stresses and strains, which provide information by compounding stress and strain components along the *X, Y* and *Z* axis and correlate well with the *Basquin-Manson-Coffin* model, and maximum

principal strains which in turn correlate well with the results of the *Brown-Miller* model, which is in fact dependent on the entity of maximum and minimum principal strain.

The method used to locate nodes of interest is detailed in Chapter 6 and Chapter 8; in the meantime, a visual representation of the results of thermo-structural analysis focused on *max. principal strains* are presented in Figures 36 and 37.

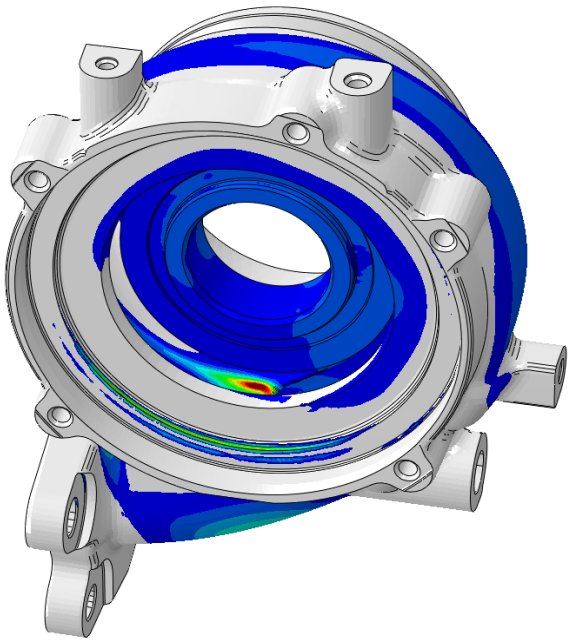

Figure 36: Max. principal log-strains ($LE_{Max,princ}$) at the start of the second heat-up step. Numerical data are confidential.

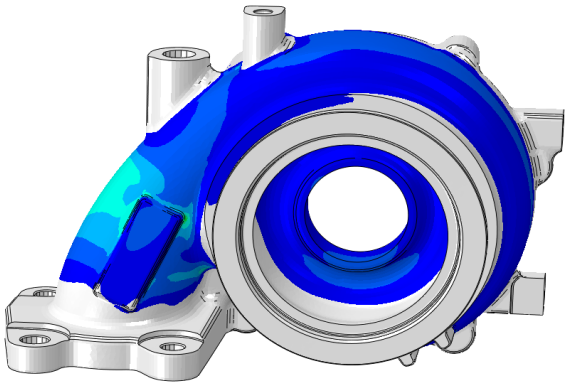

Figure 37: Max. principal log-strains ($LE_{Max,princ}$) at the start of the second heat-up step. Numerical data are confidential.

Another interesting choice for a visual evaluation of potential failure points is the estimation of *equivalent plastic strain*, calculated between the start and the end of a single stabilized cycle. This is a method commonly used in the industry, as it provides insight into those nodes that are characterised by permanent plastic strains over time rather than higher stresses or strain in a vacuum. This method is at the basis of the "*Variation of plastic equivalent strains*" or "%PEEQ" method which was mentioned earlier as a validation target and is detailed further in Chapter 6 and Chapter 8. Plastic equivalent strain in displayed in Figure 38 as an example.

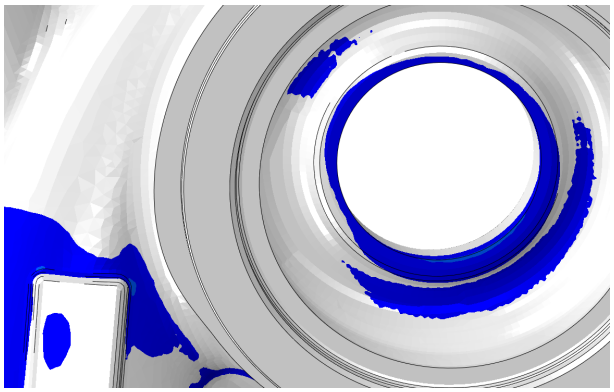

Figure 38: Residual Plastic equivalent strains (PEEQ) in a particular region. Numerical data are confidential.

5 Improvements on the base model

This chapter is dedicated to a brief introduction to different paths that can be followed to improve the accuracy of the simplified model employed in this thesis. Although results in terms of local stress and strain are expected to be in the same order of magnitude compared to the *2019 target analysis*, it is likely that significant differences may arise, bringing a level of uncertainty which has to be taken into account and, when possible, reduced. Increasing the complexity of the model, however, brings issues related to computation time which can end up being incompatible with the scope of this thesis. Trying different methods is however an interesting experiment to compare the effect of certain changes and evaluate the ones that are worth applying.

For each one of these methods, their feasibility will be analysed in Chapter 8 once numerical results have been gathered and actual comparisons are possible.

5.1 Introduction of New Elements

The obvious solution to improve model accuracy is to introduce elements that were previously removed from the complete engine model. Imposing proper border conditions on a simple model is a viable option to reduce computation time while simulating the presence of bordering components; however, it is unavoidable that the existence of a physical component affects nearby elements influencing local stresses and strains.

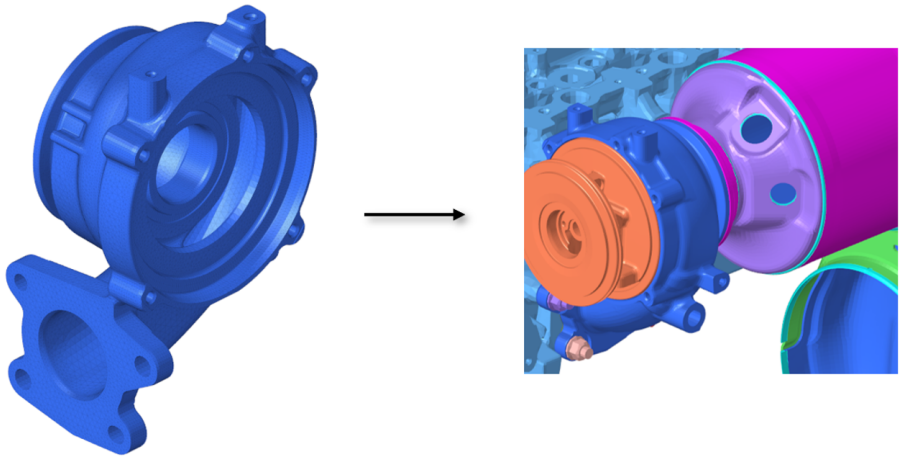

Figure 39: Improving the base model implies adding new neighbouring components.

A reasonable compromise between simplicity and accuracy is the introduction of few of the elements that are directly in contact with the turbo volute. These include

part of the cylinder head block, bolts that connect the flanges of the volute and the cylinder head, several gaskets separating adjacent elements, the bearing support interposed between the turbine and the compressor and the outlet cone that leads into the *after-treatment* assembly.

Introducing even more components could negatively affect performance, therefore the solution is to simulate their presence by imposing constrains at certain nodes. These conditions are designed in such a way to prevent axial displacement but still allow radial deformation and are located along the external surfaces of the two components.

- Constraint along axis Y on the on the outlet cone and bearing support, (displayed in orange in Figure 40). This prevents displacement along axis Y, simulating the compression caused by nearby components.
- Degrees of freedom without constraints along axis X and Z. This allows for radial displacement, to prevent the assembly from being excessively rigid (displayed in blue in Figure 40)

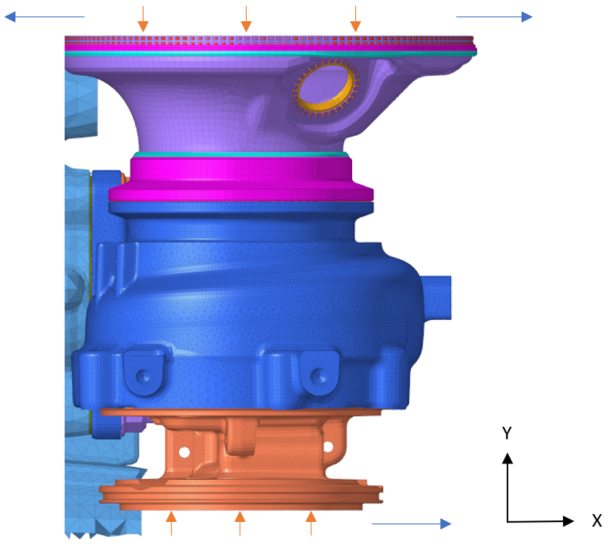

Figure 40: Visual representation of the axial constraints (in orange) and free radial displacement (in blue).

With this configuration, as the material expands, components are subjected to unconstrained radial displacement which is set to simulate the expansion or nearby

components. This is however an approximation, as it does not account for different gradients of temperature between elements, thermal conduction and axial displacements.

5.2 Increasing Mesh Density

In those cases where higher mesh density is not capable of capturing local stress and strain (for example singularities at small notches points) a solution is to increase mesh density for more accurate results.

This solution is effective but drastically increases the number of nodes of which the model is composed, increasing computation time exponentially. Therefore, applying this change to the entire modes is not possible even considering the benefits.

An easier solution that is often used in the industry is isolating the part of the model that causes issues and create a ***submodel*** with higher local mesh density. A new structural analysis focused on the *submodel* only is then launched without any further input than the "*.odb*" file that is produced by the complete structural analysis. In this way, the solver only computes on the *submodel* and uses the previous analysis simply to impose displacements as boundary conditions. Figure 41 represents an example of a *submodel* extracted from a component. The arrows indicate locations where displacements have been imposed as boundary conditions.

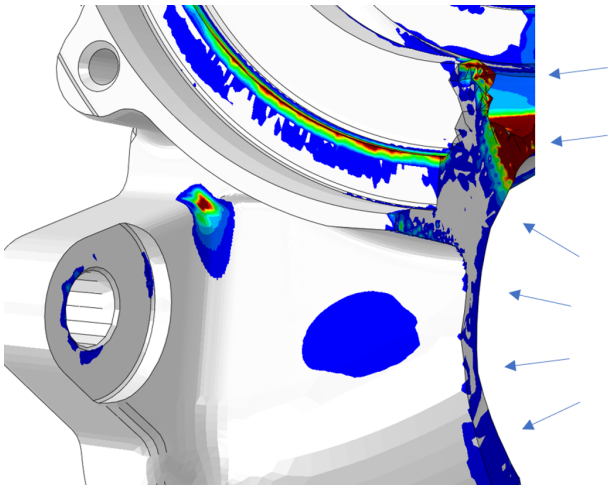

Figure 41: Detail of the submodel with displacements as boundary conditions.

This topic will be discussed further in Chapter 8, where a practical example of its use will be presented.

5.3 Increasing Time Intervals

The FEM analysis computes at its nodes by *discretization* is space and in time. The number of time increments directly influences computational cost, as the solver is required to complete more calculations in the same time interval. Usually, time increments are not equally spaced; that is because there could be time intervals where the output sees a higher degree of gradient change compared to others and require smaller increments to compute the gradient and interpolate between points with higher accuracy. An example of how time intervals are computed is presented in Figure 42, where temperature is simulated over time. It is possible to observe how time intervals are in fact not equally spaced.

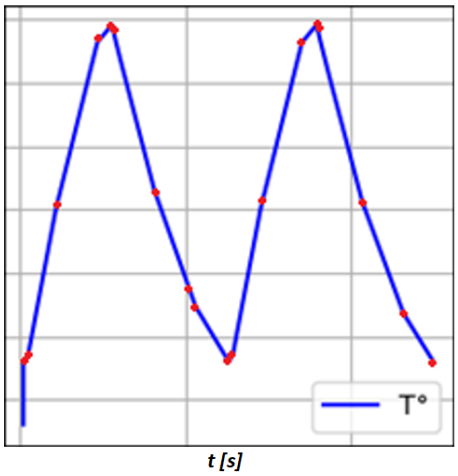

Figure 42: Fewer time intervals reduce computational cost bot may lead to inaccurate simulations.

A possible alternative is increasing the frequency of these increments or setting a fixed distance between two of them. This produces a more uniform distribution of temperatures over time. An example of this is in Figure 43, where distance between two time intervals has been imposed and the difference in shape between the previous case is evident.

However, for most traditional methods of estimation of fatigue life, such a change is not necessary. For example, if the user evaluates fatigue life through plastic equivalent strain, only the very last increment of a certain step will be observed and the progression of stress and strain over time will go mostly ignored.

In certain cases, however, such as the approach taken in this thesis work, having accurate results of stress, strain and temperature over time can significantly benefit

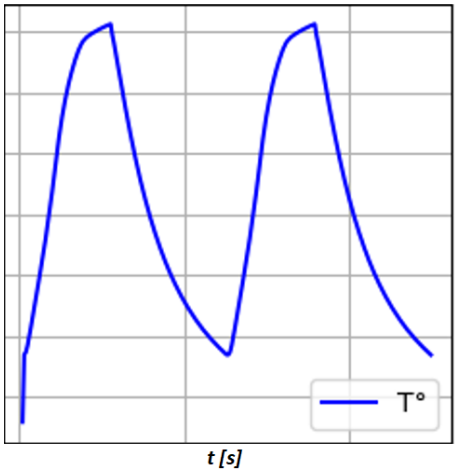

Figure 43: A higher number time intervals produces accurate results at the cost of higher computational cost.

accuracy. Calculating averages, evaluating threshold values, and estimating maximum and minimum values in a cycle often depend on the distance between time increments. This topic will be further explored in Chapter 8.

6 Data Post Processing

The purpose of the *post-processing* phase is to acquire results from thermo-structural analysis, import them in a post-processing software such as *Abaqus Viewer* and visualize them to evaluate the quality of said results or extract essential data for future steps. Some of them include:

- Receiving immediate feedback on potential issues on the design of a component, by observing local stresses and strains or tracking anomalies.
- Visualize physical displacement of the component over time or at a certain time instant.
- Acquire data files containing numerical results for future endeavours.

In the scope of this thesis, extrapolating data from a thermo-structural analysis is necessary for the correct functioning of the script and the execution of its calculations. As we will further discuss in Chapter 7, the approach taken when developing the script is to base itself on the acquisition of text files obtained as an output of the post-processing phase in *Abaqus Viewer*. These results are then used as a basis for all the calculations executed by the script, which in turn returns a numerical output and a number of visual plots.

In this chapter we will briefly explore methods used for data acquisition and evaluation of potential failure points, laying the foundation for future steps when results are available.

6.1 Evaluation of Critical Nodes

There are different paths that can be followed to process this data in order to obtain a reliable result. One option is to try and acquire a "field" containing every single node of the component, with the purpose of detecting what points are subject to higher values of stress and strain and could potentially lead to failure. Doing so requires the solver to produce an output file that gathers information about every single node, resulting in millions of lines of text with a file of an estimated size of several Gigabytes. Although a viable option, this requires a specific preparation of the *python* script, that must be optimized in order to complete its calculation in a time frame that could span several hours (as it is common with other commercial tools that estimate TMF). In the scope of this thesis, the preferred approach was different.

Instead of providing with a complete analysis of every node and therefore requiring development time dedicated to the optimization of the tool, most of the time was spent comparing and optimizing models leading a direct comparison between nodes that are known to be potentially critical from the *2019 target analysis*.

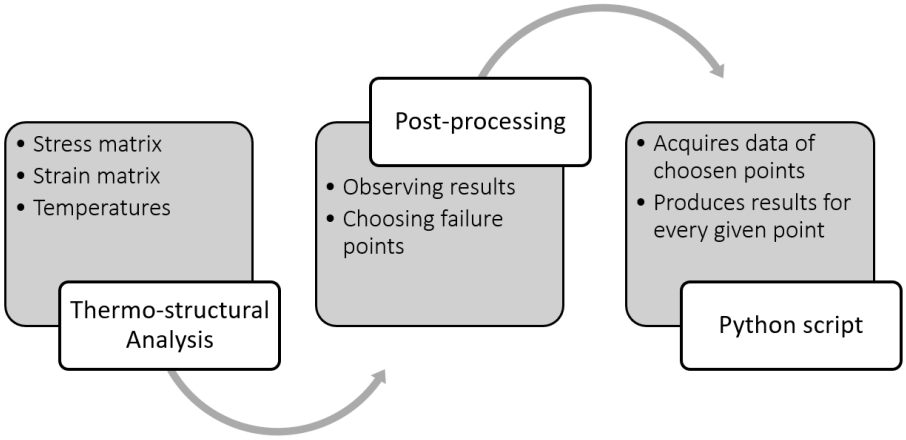

Figure 44: Typical workflow for TMF analysis, with the inclusion of the *Python* tool to be developed.

This produces a shift in the philosophy of the script; in this case, the user is more involved in the manual choice of what nodes should be analysed and only those few selected nodes will see numerical outputs. It goes without saying that the choice of said nodes becomes a crucial point, and selecting a node that is representative of a whole region becomes very important. This is why a few methods of "visual" fatigue life estimation have been employed, with the purpose of guiding the choice of the user towards nodes that immediately show more potential for failure.

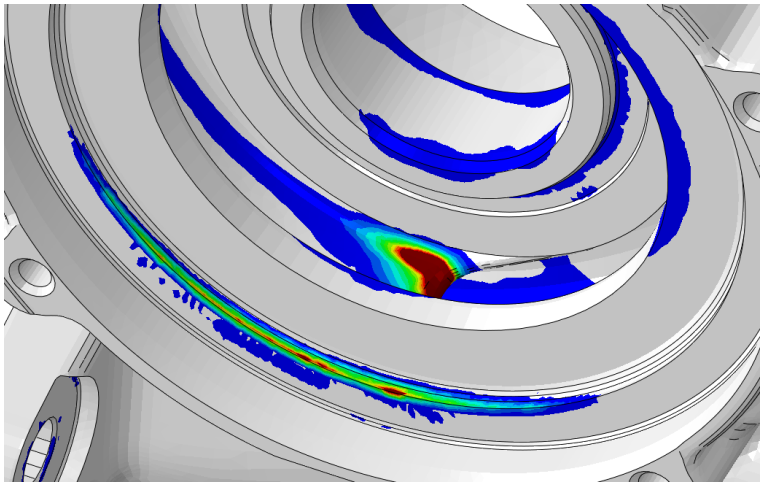

Figure 45: Evaluating the Delta of Plastic Equivalent Strain allows the user to identify potential failure points.

The main approach that was used for this purpose compares **plastic equivalent strains** between the very start and the very end of a stabilized cycle. It was therefore named "***Delta-PEEQ***" in this thesis work, although it is directly based on a method behind one of two target models that compares the percentage of plastic equivalent strain with a given target value to determine if a potential failure point is found.

The details of this method and an example of its use are discussed one again in Chapter 8. What is important to know at this point is that the user has the choice of what nodes to include and how many points are worth analysing. The basis behind this decision however comes from the visual feedback given by the post processer, such as the one in Figure 45.

6.2 Data Acquisition

The software allows the user to acquire results in different desired formats and in different shapes. The *FaLEsPy python* script was designed to acquire files (format *.txt*, *.rpt...*) containing results written in plain text. The way data must be formatted to be correctly interpreted by the script will be explored in Chapter 7, this chapter will instead focus on how the software displays and formats data.

Within the software interface, certain functionalities allow the user to manually filter certain time steps and acquire data in a specific time interval. Some of the data used by the script include:

- **Stress**: The solver computes the stress matrix in every node and for every

time increment. The stress matrix is composed by stresses along the three axis and the different combinations of shear stresses. When an output is required, these results are compiled in a text file according to Figure 46. For each node selected, stress components are organized as shown, and repeated vertically for each time increment.

$$\begin{Bmatrix} time & S^{(1)}{}_{11} & S^{(2)}{}_{11} & S^{(3)}{}_{11} \\ t_1 & \dots & \dots & \dots \\ t_2 & \dots & \dots & \dots \end{Bmatrix} \begin{Bmatrix} time & S^{(1)}{}_{12} & S^{(2)}{}_{12} & S^{(3)}{}_{12} \\ t_1 & \dots & \dots & \dots \\ t_2 & \dots & \dots & \dots \end{Bmatrix}$$

Figure 46: Stress matrix according to *Abaqus Viewer* outputs.

- **Strain**: The solver computes the strain matrix in every node and for every time increment. The principle is the same as the stress matrix, and it is displayed in Figure 47.

$$\begin{Bmatrix} time & E^{(1)}{}_{11} & E^{(2)}{}_{11} & E^{(3)}{}_{11} \\ t_1 & \dots & \dots & \dots \\ t_2 & \dots & \dots & \dots \end{Bmatrix} \begin{Bmatrix} time & E^{(1)}{}_{12} & E^{(2)}{}_{12} & E^{(3)}{}_{12} \\ t_1 & \dots & \dots & \dots \\ t_2 & \dots & \dots & \dots \end{Bmatrix}$$

Figure 47: Strain matrix according to *Abaqus Viewer* outputs.

- **Maximum principal strain**: The solver computes the value of maximum principal strain according to *Mohr*'s circles for each time increment. These results are compiled in a text file according to Figure 48.

$$\begin{Bmatrix} time & LEmax\ princ \\ t_1 & \dots \\ t_2 & \dots \end{Bmatrix}_1 \begin{Bmatrix} time & LEmax\ princ \\ t_1 & \dots \\ t_2 & \dots \end{Bmatrix}_2$$

Figure 48: Max. principal strains according to *Abaqus Viewer* outputs.

- **Temperature**: Values of temperature for each node and for each time increment are calculated and presented as in Figure 49.

As already mentioned, all this data is store in text and can be acquired by the *python* script which in turn extracts and elaborates information within itself. It is however responsibility of the user to correctly source this data. In fact, as we will

$$\begin{Bmatrix} time & T° \\ t_1 & \dots \\ t_2 & \dots \end{Bmatrix}_1 \begin{Bmatrix} time & T° \\ t_1 & \dots \\ t_2 & \dots \end{Bmatrix}_2$$

Figure 49: Temperatures according to *Abaqus Viewer* outputs.

further discuss in Chapter 8, the choice of what time intervals should be included can influence results. This brings back the topic of the *stabilized cycle* and the choice of a time interval which is representative of the operating conditions of the component.

Once the stabilized cycle has been isolated, data is ready to be acquired by the *python* script and used to produce results that aim to estimate thermo-mechanical fatigue. An example of how the stress-strain-time trend can be visualized along each axis is shown in Figures 50 and 51.

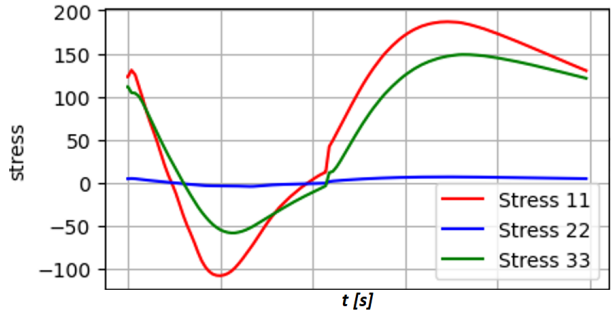

Figure 50: Normal Stress components in a generic node during a single cycle.

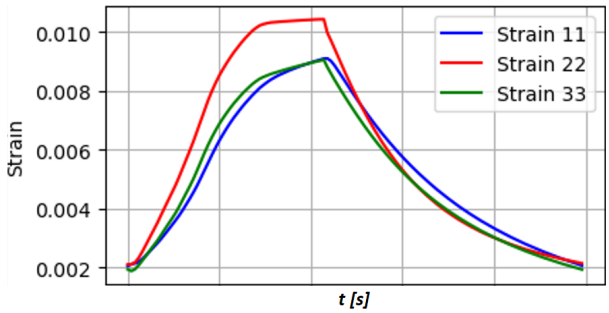

Figure 51: Normal Strain components in a generic node during a single cycle.

7 Script Development

The purpose of this thesis is to provide a method for the user to analytically evaluate fatigue life of components. The models applied have been already described in a previous chapter. What remains to be defined is the implementation of said models in a way that can be easily interpreted by the user and that produces reliable results. The solution is the development of a code in *python* whose purpose is to calculate said results and aid the user in their interpretation. The *python* script developed with this scope in mind was named *FaLEsPy* as in *Fatigue Life Estimator in Python*.

Figure 52: Simple logo designed for the FaLEsPy tool.

The code has been entirely developed in *Python* and it is organised in a series of directories to easily categorize different pieces of script or different modules. The main script is composed by around 1500 lines of code that handle callbacks to specific functions, do specific operations and handle the user interface. Inside subdirectories, specific modules contain specific functions to execute differ operations. Modules are pieces of code that can be called back in the main script in order to make the code more readable. The base of the script is the $main\_interface\_FaLEsPy$ script that contains all code regarding the interface and all the call-outs to the different functions or 'models'.

7.1 The Main Code

The main code is the executable necessary to launch the tool correctly. It was developed using the *Spyder* compiler and it uses some of the most common python libraries for several of its functions. Some of them include *matplotlib*, *NumPy*, *math*, *tkinter* and others. It is organized in different sections:

- **Initialization** section of the script with the purpose of importing required

libraries and set the directories from which the different secondary scripts and modules will be acquired.

- **Initialization of the user interface**, programmed in *tkinter*. At the very beginning of the script, the *root* window is initialized, and all elements are included afterwards throughout the script. The *main loop* of the *root* window is then closed at the very end of the script.
- **File browsing** section, dedicated to all functions related to the acquisition of input data. The script is capable of browsing directories to select data files and then saves numerical values internally as long as the script is operational. All data that can be acquired include stress, strain, temperature and material properties. The script is also capable of isolating the very last *stabilized cycle* in a time history.
- **Preparation** of *Basquin-Manson-Coffin* curve, where the script uses the *Basquin-Manson-Coffin* equation and material properties to plot the curve.
- **Execution of multiaxial models**, where equivalent strains are calculated for each model.
- **Fatigue** life calculations with the display of final results.

7.2 Secondary Scripts

The secondary scripts or "*modules*" are tasked with different operations regarding specific models, utilities, data input or output and others. They contain specific callbacks so that, when imported as libraries in the main code, they can be executed from it without being present in the code itself. Some of their functions are:

- **EquivalentTemperature**: *EquivalentTemperature* is a multi-purpose script that serves two main functions. The first is acquiring materials data. The second is interpolating this data based on the average temperature of a node. This is done with three different methods. The first is an *arithmetic average* of all temperatures over time. The second is an *integral average* of temperatures, more accurate in case the time discretization is not equally spaced. The third is the "*Taira-inspired*" method.
- **BasquinMansonCoffin**: *BasquinMansonCoffin* is a multi-purpose script with different module inside. It can acquire materials data (which have to be formatted in a specific manner), It can create BMC curves and it can find the

critical element by taking equivalent strain as an input. All of these functions are called through different models with different names.

- **FileManager_VM_BMC**: *FileManager* is a large script that is used to handle data, meaning that it reads and writes information regarding stress, strain and temperature. It has dedicated models for reading input "*.txt*" files, for "translating" them in the order that the script prefers and write them down in "*.txt*" files so that they are saved in an organized manner. It is not necessary to put input files in the same directory as the script, but all subsequent operations will produce text files inside the directory.

- **FindStabilizedCycle**: This script finds the last stabilized cycle by detecting a change in gradient of strain and assigning a flag with a number. The script then takes the last 2 "directions" identified by index 1 and 2 representing the stabilized cycle and discards the rest.

- **VonMises, ASME, SonsinoGrubisic, BrownMiller, Skelton**: Handle all calculations regarding their respective models. They usually take strains and stresses as inputs, returns equivalent strains or, in the case of the *Skelton* model, it returns cycle areas and fatigue life. It also acquires material properties from input files.

7.3 User Interface

The last part of the tool development was dedicated to the inclusion of a user interface designed using the *tkinter python* library. The purpose is to make the tool more accessible to the user, instead of requiring knowledge of a complex code and its inner workings. All the functionalities of the script are built upon a single window that serves as the main interface for every operation, from data acquisition to results.

The first quadrant of the interface in Figure 54 is dedicated to file browsing and specific preparation steps, with the "*Data Inputs*" section having dedicated buttons with the purpose of acquiring different types of files as well as locating the last stabilized cycle. Figure 53 summarizes the typical workflow for the script.

The "*Equivalent Properties*" section allows the user to select the preferred method for equivalent temperature estimation. At this stage, the script allows to calculate this temperature through arithmetic average, integral average with the trapezoid method as well as the *Taira*-based method introduced in this work. This temperature is then used to interpolate the values of material parameters for the BMC model at the desired value of temperature.

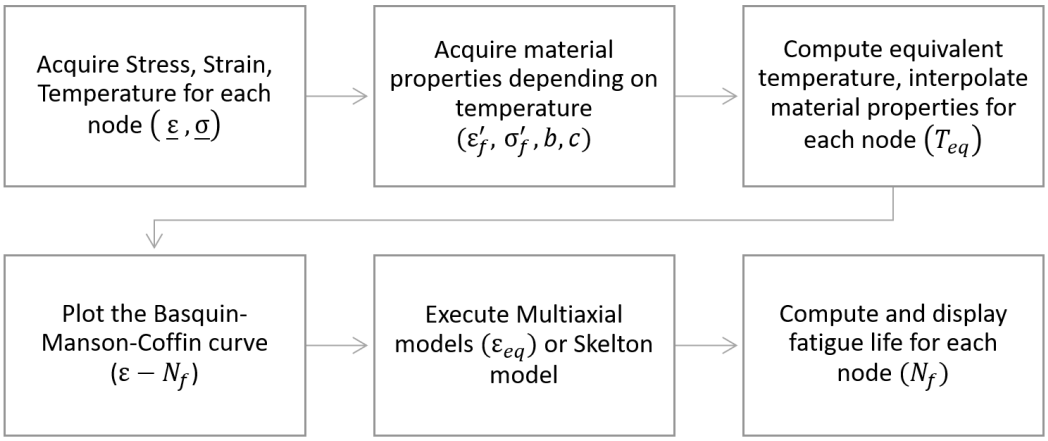

Figure 53: Complete workflow for the script.

The "*Basquin-Manson-Coffin*" section has the purpose of "preparing" the curve for future calculations. It uses the BMC equation described in Chapter 3 to link an array of fatigue life numbers (by default ranging from 1 to 100000 cycles) to specific values of strain. This is done as a function of the material parameters defined at the aforementioned equivalent temperature.

The second quadrant of the interface in Figure 55 displays a "console", where information on the execution of specific commands is displayed. Dedicated buttons allow the user to clear the content of the console or print its content into text file for future reference.

The third quadrant in Figure 56 is dedicated to the execution of multiaxial models and fatigue life calculations, done with the aid of the BMC curve plotted beforehand.

"*Multiaxial*" and "*Skelton*" models work differently from one another, where the first requires two steps to compute uniaxial strain and fatigue life, where the second directly computes fatigue life. "Show data" section opens a window to display stress and strain of a certain node, while the "*Results*" section displays fatigue life results for each node, similar to Figure 57.

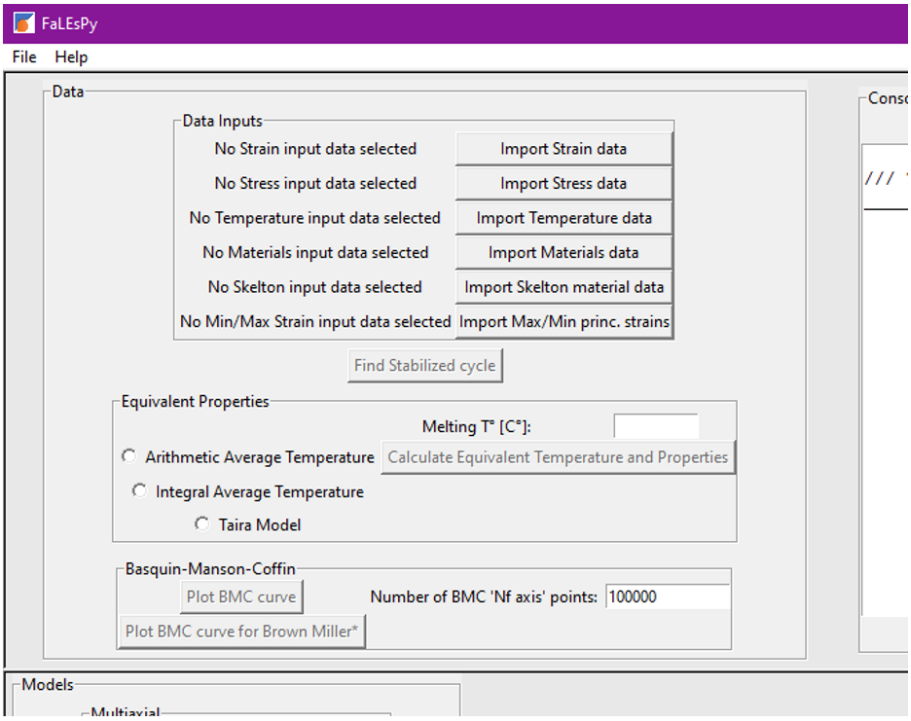

Figure 54: "*Data*" section of the script.

It should be noted that nodes are not associated with a label at this point, and they are displayed in the same order as the *Abaqus Viewer* output file, which has been observed to be in ascending order by *ID number*. The last quadrant in Figure 58 aids node interpretation: By including node IDs in the "*Node IDs*" section, the script then orders them in the same manner as *Abaqus Viewer* does, and displays them besides the values of fatigue life, allowing the user to recognize nodes by their ID.

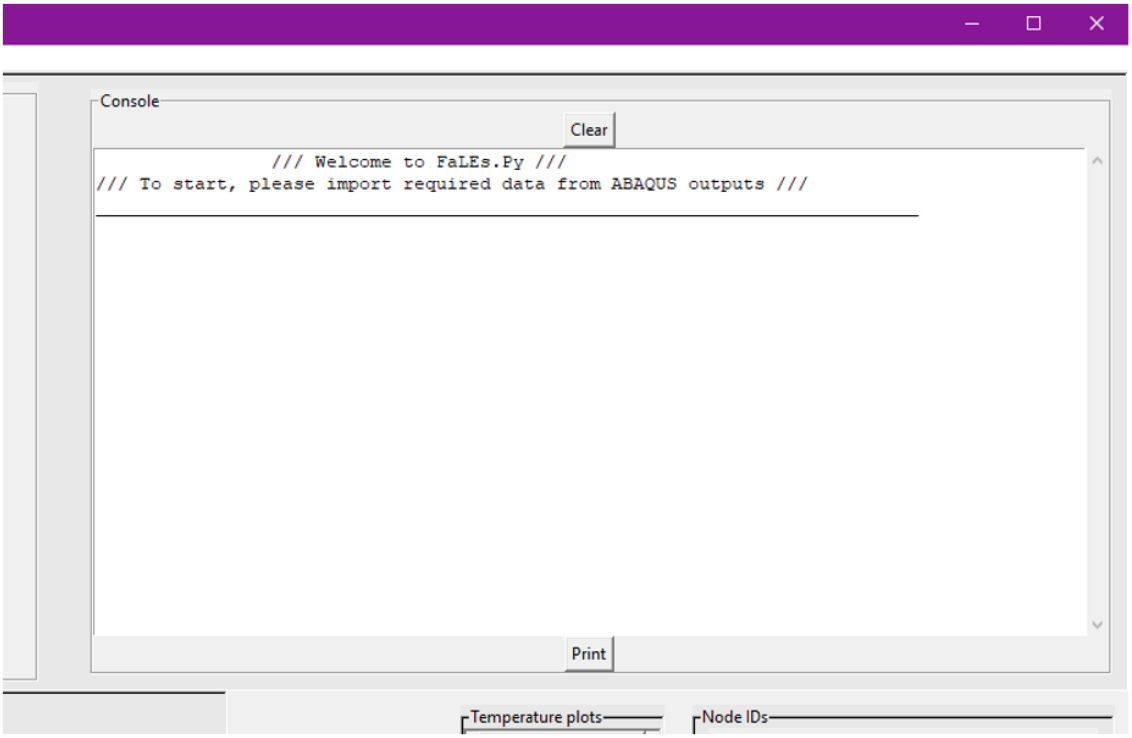

Figure 55: "*Console*" section of the script.

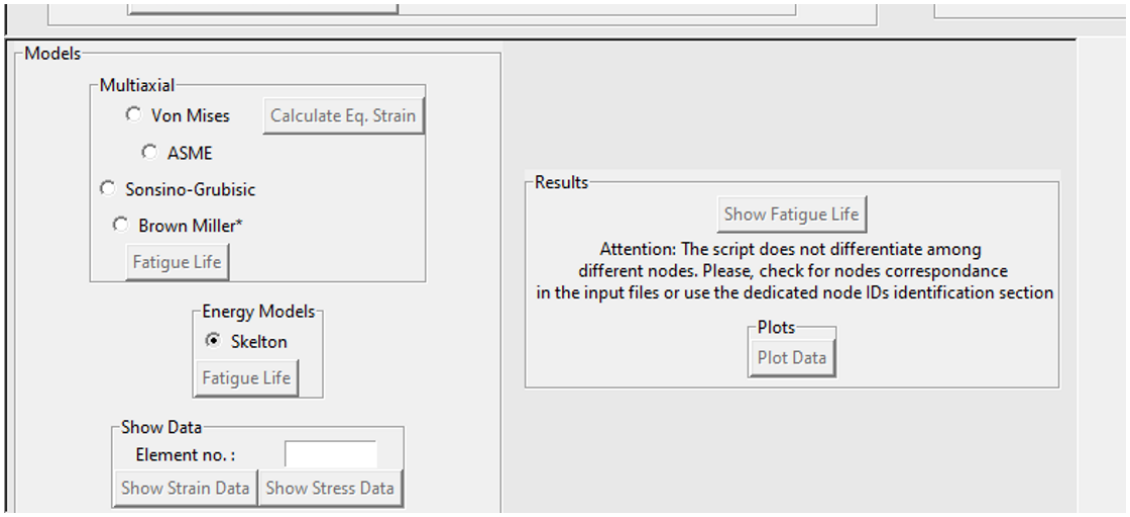

Figure 56: "*Models*" section of the script.

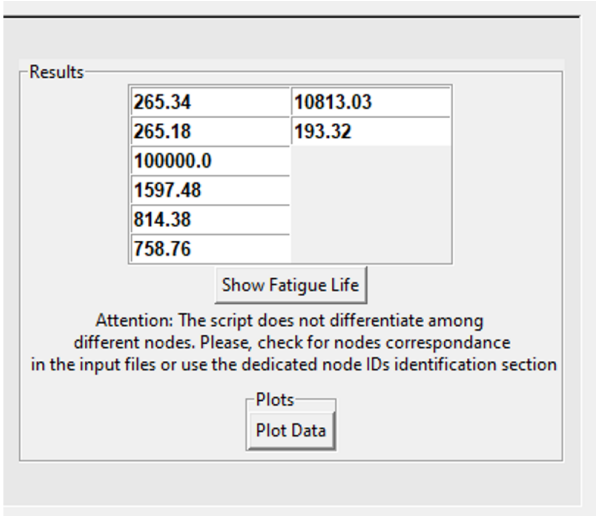

Figure 57: "*Results*" section of the script.

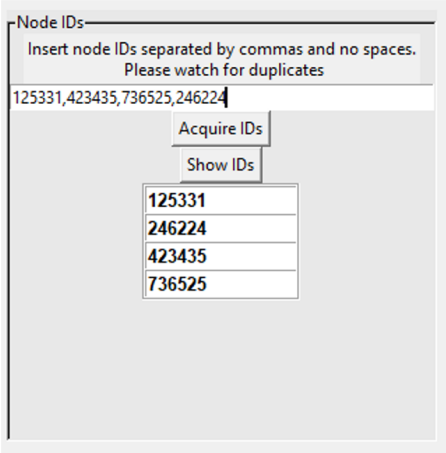

Figure 58: "*IDs*" section of the script.

8 Results

The previous chapters laid the foundations of the workflow that was followed throughout the duration of the thesis work, with the purpose of acquiring data regarding fatigue life of certain points of the component and compare results with the one presented in the aforementioned internal *2019 report*, which itself shows a comparison of fatigue life estimation between the %PEEQ method and *TFAT*.

This chapter focuses on applying the knowledge presented in Chapters 3 through 7 in order to achieve the desired outcome. The theoretical background of most topics has been already discussed, this part is instead focused on detailing the steps followed and the choices made to obtain numerical results.

The process of executing thermal and thermo-structural analysis has been discussed in Chapter 4 and all information necessary to understand the process behind it has been already detailed in said chapter. The only aspect worth pointing out is the starting point of the analysis, that being the starting mesh geometry that was used to gather the first batch of results. The model is composed of the turbo volute and few surrounding elements, such as the bearing support between the turbine and the compressor, a small part of the cylinder head block, a small part of the outlet cone and several gaskets connecting adjacent parts.

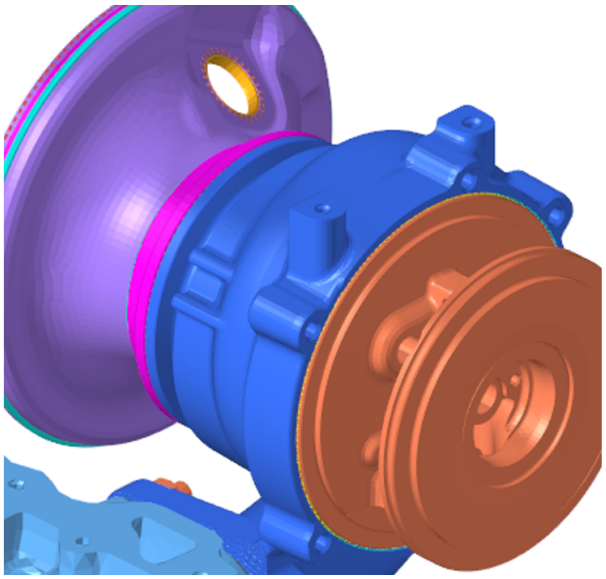

Figure 59: Mesh geometry of the *Head-Turbo-AT* assembly.

Chapter 3 detailed several different criteria, multiaxial and uniaxial, for the

estimation of equivalent uniaxial strain and fatigue life as well as the background of existing damage models. The models implemented within the script include:

- *Von Mises* model: It acquires the strain matrix over every time increment, returns a single value of equivalent uniaxial strain.
- *ASME Code*: Derived from *Von Mises*, it acquires the strain matrix and returns a single value of equivalent uniaxial strain.
- *Brown-Miller* model: Unlike other models, it requires the user to acquire the values of maximum principal strains and returns a single value of equivalent uniaxial strain.
- *Sonsino-Grubisic* model: It acquires the strain matrix over every time increment, returns a single value of equivalent uniaxial strain.
- *Skelton* model: It works uniquely compared to other models, it acquires stress and strain matrix, it calculates the area of a single hysteresis cycle and compares it with an experimental value. Returns the value of fatigue life cycles. It is the only model that does not require using any uniaxial model.

These different models have been chosen due to their purely analytical approach, not requiring further experimental data (with the exception of the *Skelton* criterion), and they have all been implemented in a way that allows the user to swich seamlessly among any one of them. Each one of them has their strengths and weaknesses and works better in different conditions. Therefore, the purpose of this comparison is not to produce the same result for each model but to observe which models seems to behave more reliably in a specific application. Once equivalent strain has been computed, uniaxial damage models show their purpose:

- *Basquin-Manson-Coffin* model (or BMC): It acquires equivalent strain and a single value of equivalent or average temperature of the cycle, from which material properties are derived. It returns a single value of fatigue life.
- *Basquin-Manson-Coffin* model modified for *Brown-Miller*: Almost identical to the base BMC, it uses a different equation specific to the correct functioning of the *Brown-Miller* model.

Chapter 3 also discussed the topic of estimating an equivalent average temperature of the cycle to make the use of the BMC model possible by providing a single temperature representative of the cycle. Throughout several tests, all three methods have been

compared among each other but the *Taira*-based model, designed specifically for this thesis work, has proved reliable in replicating target results more accurately. Therefore, from now onwards, by default it should be assumed that results have been gathered with an estimated equivalent temperature with the *Taira*-based method in order to effectively calibrate the different models for this case study.

Chapter 2 discussed different constitutive models and the effect of different physical and chemical phenomena depending on temperature. The model that is considered the basis for understanding high temperature phenomena is the *Chaboche* model, also widely used in the industry for its reliable results. Throughout several tests, *Chaboche* constitutive model proved to better correlate with target results and better simulate the effect of high-temperature phenomena. By default, it should be assumed from now onwards that results have been gathered with material properties calculated with the *Chaboche* constitutive model.
The workflow followed in this work can be summarized in a brief sequence of steps:

1. Design of the component and the mesh geometry.
2. Preparation and execution thermal analysis, extracting results.
3. Preparation and execution structural analysis, extracting results.
4. *Post-processing* phase, display results to visually evaluate potential failure points. Manually select nodes of interest and acquire stress, strain, temperature in the form of text files.
5. Import the text files in the script, set material properties, with a given equivalent temperature of the cycle.
6. fatigue life is estimated.

Figure 60 and 61 summarize the process with a visual approach. Figure 60 is focused on the "solver" side of the process, with a summary of thermo-structural analysis and its outputs, while Figure 61 is focused on the inner workings of the script. Once all data is available, results are displayed by the script interface, provided the tool has been used correctly. For each node chosen in the post-processing phase, the script returns a single value of fatigue life for any model selected.

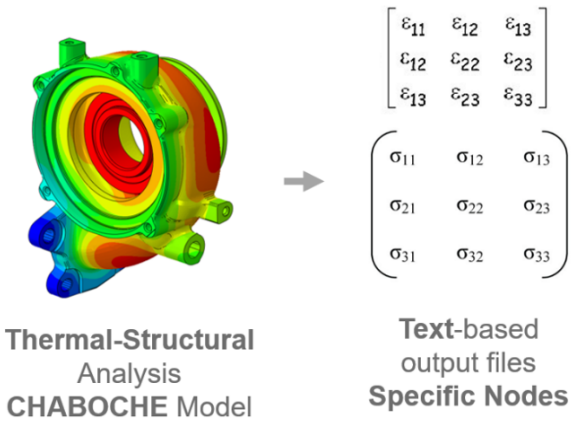

Figure 60: Stress and Strain data as *Abaqus* outputs.

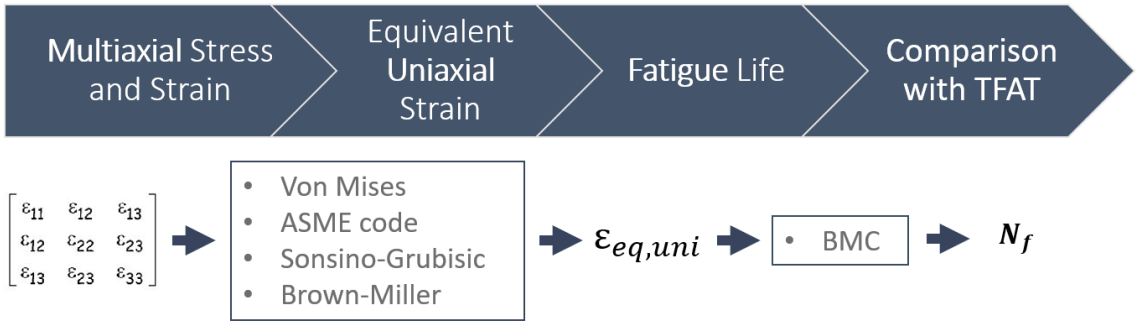

Figure 61: Sequence of actions executed by the script.

8.1 Data Collection Campaign

The results of the analysis have been gathered with the main goal of comparing different combinations of approaches and methods while evaluating the effectiveness of the improvements that have been proposed.

Results have been post-processed several times to collect information on every improvement or modification of the model, with the expressed purpose of comparing the behaviour of each model with varying conditions. Afterwards, these results are compared with the available *validation targets* in order to evaluate the accuracy of each prediction, in particular with the numerical results produced by the commercial software *TFAT* and with the estimation given by the *%PEEQ* Method (*Plastic Equivalent Strains*), both of which will be detailed shortly.

It is important to note that the main goal of this comparison is not to reach a perfect match with the target values from these two methods, as themselves are often subjected to varying degrees of uncertainty when compared with real-life scenarios, but to produce estimations that are comparable to such methods and that reflect the core meaning of these results. With this goal in mind, the main interest is to be able to effectively identify the most critical points of a component in order to predict failure and modify the design before involving more advanced pieces of software.

With regard to the different model improvements proposed in Chapter 5, and to the several models proposed, results of the data campaign can be summarized in a chart similar to Table 1:

Table 1: Example of fatigue life results table

	V. Mises	ASME	Sonsino	B. Miller	Skelton	time [h]
Original Model	-	-	-	-	-	-
New Model	-	-	-	-	-	-
Time Discr.	-	-	-	-	-	-
Submodel	-	-	-	-	-	-

This results table should then be repeated for each node analysed, giving a table of results for each method applied to each node at different stages of the model. Results are then compared with the validation targets and a brief description is given to the results, in terms of how much they resemble the target. In particular, a node can have its fatigue life estimation be either *Validated*, *Too Low* or *Too Safe*. This judgement is not given as based entirely on a numerical comparison but also accounts for the relative proportion among each other, meaning that, even if below a certain validation target, results are acceptable if they reflect the "logic" of the target compared to

each other. Such cases will be accordingly marked and a new validation target for that particular method should be estimated through further validations on different components. This topic will be further discussed in Chapter 9.

This work also provides information regarding the computation time roughly required for thermal and structural analysis. This can vary depending on the system used, but it should provide a reference by comparison.

The process described in Chapter 6 is followed, and results files for stress, strain and nodal temperatures are extracted from the "*.odb*" file obtained with the structural analysis. Data is then acquired by the *FaLEsPy* Python script and transformed into fatigue life results for each node chosen from the component and for every model proposed.

The choice of the nodes of interest is the first step that requires consideration, therefore the topic of accumulated plastic equivalent strain introduced in Chapter 6 is now detailed for this particular case study. In order to give an effective first estimation of fatigue life, it is important to choose these nodes in a way that includes all points that could potentially lead to failure. Predicting such points before having the results at hand could lead to an inaccurate analysis, even considering user experience. It is important to give a baseline method to try and identify these points. The approach used in this study is here named "*Delta-PEEQ*" method.

$$\Delta PEEQ = PEEQ^{step=8}_{time=end} - PEEQ^{step=7}_{time=start} \tag{89}$$

The "*Delta-PEEQ*" method is based on the very same validation target that uses plastic equivalent strains to identify failure points. In this case, the "*Delta*" in Equation 89 computes the increment of equivalent strain between the start and the end of the last stabilized cycle, visualized as the two red dots in Figure 62. In this case, *step 7* represents the second Heat-up transient regime while *step 8* represents the second Cooldown regime. This gives the user important information on what points in the components are subjected to higher plastic strains during the various cycles. A colour-map on *Abaqus Viewer* is then displayed to help identify potential critical nodes.

This type of preliminary visual analysis is standard in the workflow for thermo-structural analysis, and it is usually aimed at giving preliminary results before further work is done on the component. This step is what the "*PEEQ*" method is based on. From this point, we will take it a step further to try to compute fatigue life analytically. From this study, certain points have been detected.

- **A: "Tongue Region"**. The first node of interest is that in the so-called Tongue Region. This region is located in a precise space on the internal surface of the

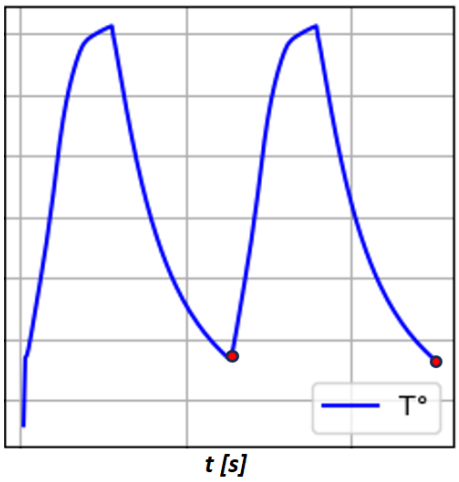

Figure 62: Start and end of the stabilized cycle are highlighted by a red dot. Axis data removed for confidentiality reasons.

volute. This node is indicated as the most critical point in both *TFAT* and the *PEEQ* method and therefore is the main point of comparison for this study.

- **B: "Flange Region"**. Another node if interest is located at a notch near the flange that links the cylinder head block and the turbo. Thus, it has been named as "*Flange*" region. This node has supposedly not been recognized as critical by any other validation target, however further researched proved that the mesh geometry used for this study presents differences in design particularly for this point compared to the CAD model which was the basis for the analysis previously done in *TFAT*. This introduces a degree of uncertainty that we must accept at this stage, as it was not possible to recover the mesh geometry for the original design.

- **C** and **D**: "**Bearings Upper**" and "**Bearings Lower Regions**". Two nodes of interest are located in the internal region of the turbine that holds the rotor blades. These two points sit near the edge of the internal cylindrical surface that represents the point of highest temperature of the whole component. The node **C** is indicated in *TFAT* as a potential critical point. The node **D** slightly safer in *TFAT* compared to C and it is above the threshold value. These two nodes have been named "*Upper Bearings Region*" and "*Lower Bearings Region*" in this work.

- **E: "Rectangular" Region**. The last node of interest is located at a notch on

the external surface of the volute. This node was not detected in *TFAT*, but it was analysed in the *PEEQ* target analysis, and deemed safe. This node was named "*Rectangular region*" in this thesis work.

The region that was not included in the analysis is the surface of the circle that is facing the compressor. Despite high plastic equivalent strain, this surface is in a compressive state which hinders cracks growth. All the nodes of interest are highlighted in Figure 63. Table 2 summarizes the nodes analysed in this study and their respective target

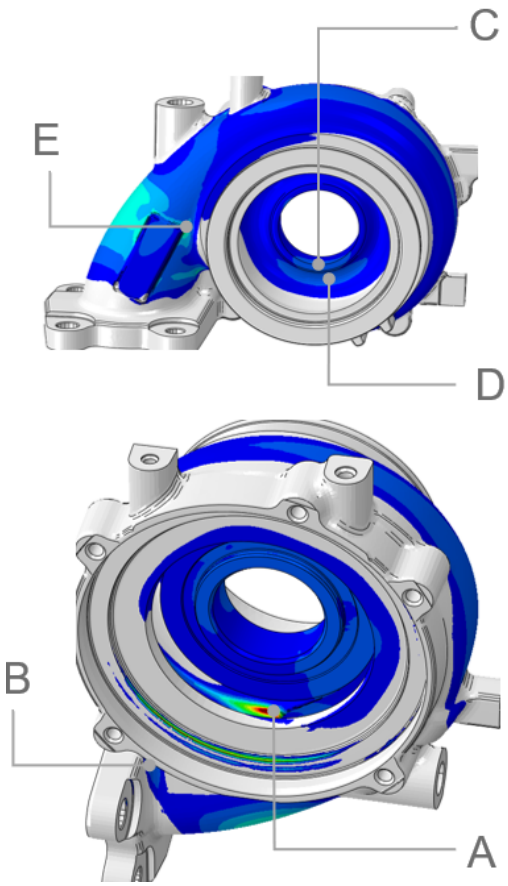

Figure 63: Locations of the nodes analysed; these points represent the focus of this thesis work.

values, obtained from the internal *2019 analysis* conducted on the same component. In the case of the *TFAT* analysis, a set of numerical values representative of the fatigue life of each point was given. This analysis mainly proved that the failure

was caused by fatigue in the *tongue region*. The other node of potential interest is the *Upper Bearings Region* which resulted in a value of life cycles slightly below the threshold value, which is experimentally obtained as the number of cycles to cause failure. Numerical results have been rounded to multiples of 50. The *PEEQ* analysis is presented in the report as a comparison to the *TFAT* method, and it compares the percentage of equivalent strain with a threshold percentage that leads to failure (Indicated as 'Thr.' in Table 2). As this is outside our scope, no numerical values are associated with this method and only the terms "*Safe*" and "*Not Safe*" are used to indicate the outcome of the estimation.

Table 2: Target results obtained from the internal 2019 Analysis, conducted on the same component

	A:Tongue	**B**:Flange	**C**:Upper	**D**:Lower	**E**:Rect.	Thr.
TFAT	**50**	-	2100	2500	-	**2250**
%PEEQ	**Not Safe**	-	Safe	Safe	Safe	**5% PEEQ**

Figure 64, Figure 65 and Figure 66 include a close-up of all the regions involved: These regions are characterized by the highest value of residual plastic strain, indicated by their colour ranging from yellow to red. Numerical values have been removed due to secrecy reasons.

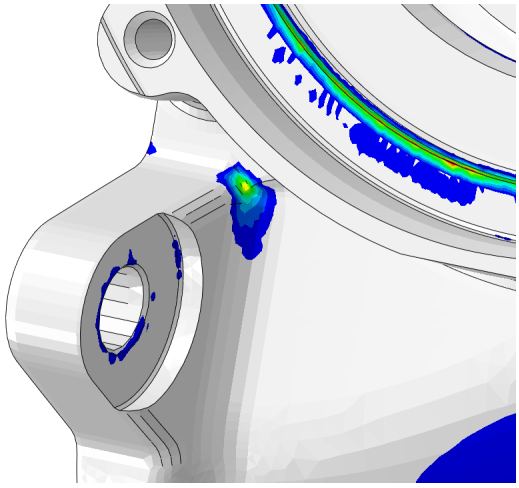

Figure 64: *PEEQ* in the *Flange Region*.

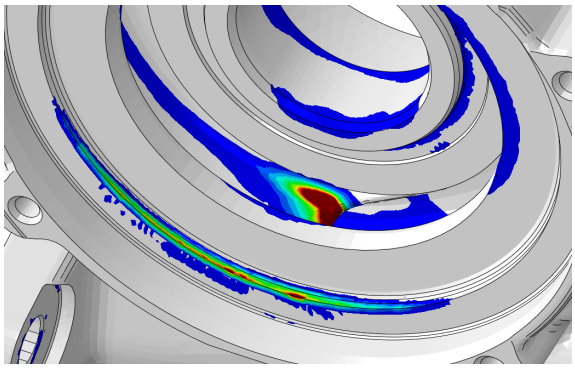

Figure 65: *PEEQ* in the *Tongue Region*.

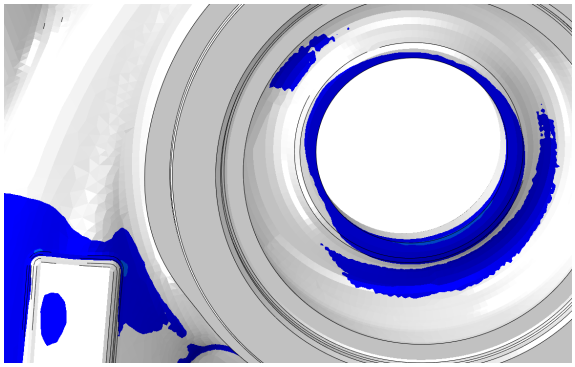

Figure 66: *PEEQ* in nodes **C**, **D** and **E**.

With this premise, data gathered from the thermo-structural analysis of the model can be presented. The thermal and thermo-structural analysis have been conducted on a mesh geometry that includes the turbo component and some of the surrounding elements. This was done to roughly simulate boundary conditions while at the same time reducing computation time.

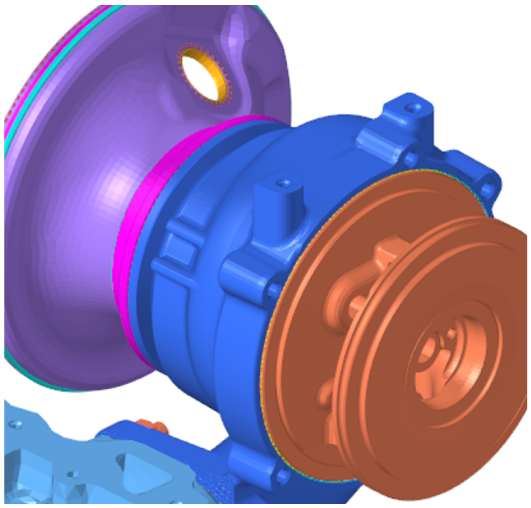

Figure 67: Mesh Geometry and the components included in the assembly.

Two different analyses have been conducted with this model, mostly identical with the main difference being the use of elasto-plastic material property cards as an input for *ABAQUS* in the first case, and the use of a *Chaboche* material property card for the material of the turbo. Between the two, the results from the *Chaboche* model only will be analysed and discussed in this chapter, as it showed more reliable results as well as reflecting better the nature of the phenomena involved. Data has been compiled in Figure 68

With results at hand, every node of interest can be commented individually and a comparison between the different models can be made:

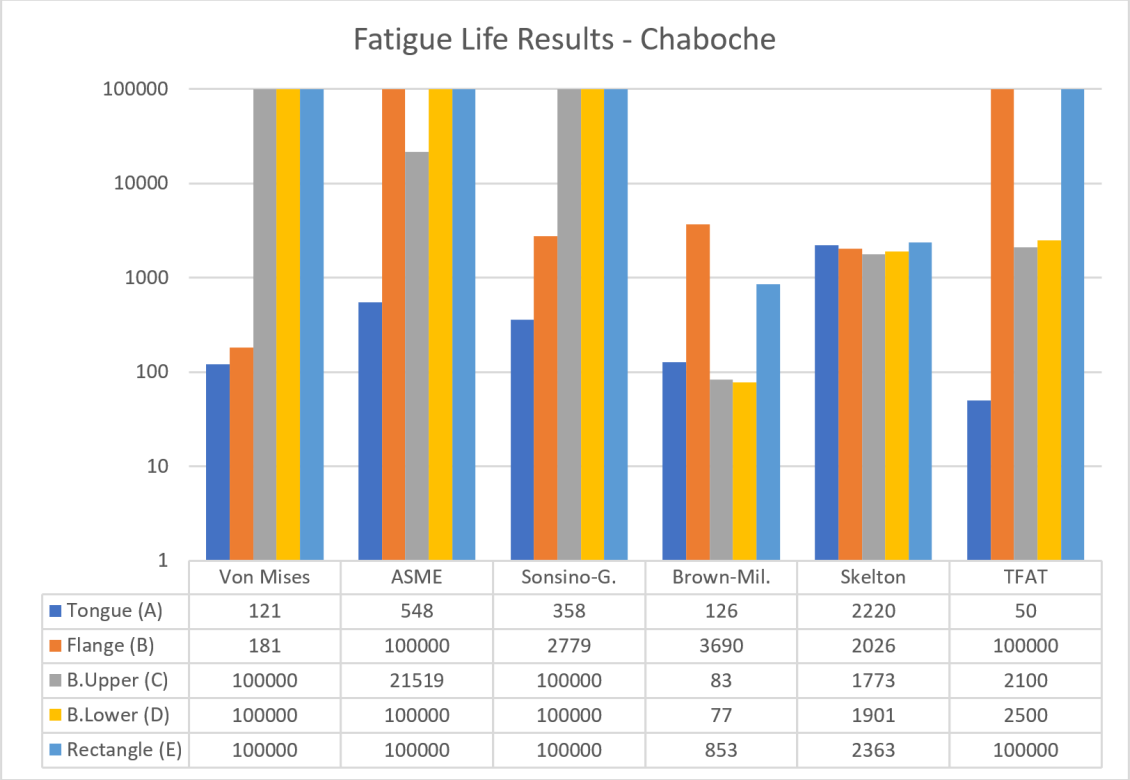

	Von Mises	ASME	Sonsino-G.	Brown-Mil.	Skelton	TFAT
Tongue (A)	121	548	358	126	2220	50
Flange (B)	181	100000	2779	3690	2026	100000
B.Upper (C)	100000	21519	100000	83	1773	2100
B.Lower (D)	100000	100000	100000	77	1901	2500
Rectangle (E)	100000	100000	100000	853	2363	100000

Figure 68: Fatigue life results of first analysis.

- **Tongue Region A**: Almost every model correctly identifies the Tongue Region as the critical point of the component. *Von Mises* and *Brown-Miller* produce the most conservative estimation, while *Sonsino-Grubisic* and *ASME* are characterized by a much higher value compared to the target, despite still recognizing it as critical compared to other nodes. *Skelton* is the only model that does not seem to replicate the same logic of others.

- **Flange Region B**: : The Flange Region produced interesting results. *Von Mises* is the only model that seems to identify this region as potentially critical, similarly to the Tongue region. To some degree, the same applies to *Sonsino-Grubisic* but with a wider margin. The other models do not seem to replicate the same result. More details about the Flange Region will be discussed shortly.

- **Upper Bearings Region C**: The Upper Bearings Region represent the second lowest value of fatigue life cycles according to the *TFAT* target values. However,

this analysis does not seem to replicate this result with the same level of nuance. In fact, the only model that identifies this point as critical is the *Brown-Miller* model and, to some extent, the *Skelton* model. The latter, however, requires some comments regarding its accuracy that will be presented shortly.

- **Lower Bearings Region D**: This region follows the same line of reasoning as the Upper Bearings Region, with a larger value of cycles. Compared to the previous node, this was not flagged as critical in the *TFAT* target analysis.

- **Rectangle Region E**: The Rectangle Region was identified both in the *TFAT* target analysis and the *%PEEQ* analysis as not critical, and this is result is consistent with the results obtained. *Brown-Miller* is the only model that produces a value lower than the threshold of 2250 cycles, although significantly higher compared to the other nodes.

In general, the two models that have shown more promise are the *Von Mises* and the *Brown-Miller* criteria. Although with a different magnitude of number of cycles, both methods seem effective at identifying the *Tongue Region* as the critical point of the component, to some extent even the *Sonsino-Grubisic* model seems to capture the same logic as *Von Mises* but with a wider margin. This data is very encouraging. It proves that most models are indeed capable of replicating the core result of their target analysis, that being that the tongue region could potentially be a source of issues and a point for crack nucleation and growth. This also proves that a simplified, mostly analytical approach to thermo-mechanical fatigue and its complex phenomena is viable, and the complex phenomena of TMF can in fact be reduced to a simpler and less time-consuming analysis, to some degree. The same cannot be said about the *Skelton* model that, as described in Chapter 3, takes into account the area of the hysteresis cycle to extract fatigue life. In this case, results appear more erratic, and it is possibly due to the complexity of the component and the wide difference among tensile states.

In fact, by acquiring hysteresis cycles of different nodes, it was observed that in some cases, nodes characterized by lower overall strain and equivalent plastic strain describe hysteresis curves with a larger internal surface, representative of dissipated energy. The relationship between dissipated energy and fatigue crack growth is an entirely different topic that requires further studies, and it was not possible to conduct them in the scope of the thesis, also due to the lack of experimental data.

A possible development to aid the solution of this issue is implementing the model proposed by *Sesana* and *Delprete* [10] that was previously discussed in Chapter 3. However, it was not possible to conduct experimental test to acquire the data required

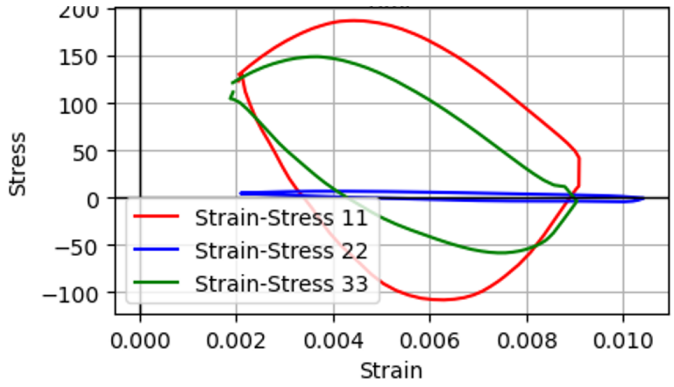

Figure 69: Example of hysteresis diagrams computed for each component of normal stress and strain.

by the model. Thus, at this stage it is not possible to implement improvements to the *Skelton* model and the result must be accepted as is, with the prospect of future studies and developments.

The last point to discuss is the matter regarding the **Flange Region B**; as previously stated, with further research it was noted that certain differences are present between the model used for the *2019 target analysis* and the current model that produces this result. As it was not possible to re-create the same geometry 1 to 1, and the current model repeatedly flagged this region as potentially critical, this degree of uncertainty had to be accepted and the Flange Region was noted as the second point that could potentially lead to failure.

This is however a reasonable result. Notches points are known in structural mechanics to often the cause of failure and crack growth. With the high level of strain and stress registered in this point, which is the second highest behind only the tongue region, it is reasonable to assume that it could potentially lead to failure and that a change in design is required. Although not much is known about what design choices have been made to the model before the completion of the *2019 TFAT analysis*, it is reasonable to believe that this region was modified to prevent this risk from happening. Thus, although distant from the validation target, the results obtained regarding the flange region should not be entirely discarded as incorrect.

Despite results being encouraging, there is still ground to improve upon. In fact, even if the tool successfully identifies the *Tongue Region* as critical, it still provides uncertain results when it comes to different nodes. The *Upper* and *Lower Bearings Region*, in particular, require further analysis. The *TFAT* target analysis regards it as a slightly critical region, with much higher values of fatigue life cycles compared

to the Tongue Region. Most models, however, do not seem to be able to recognize this nuance or, on the opposite side, regard it as critical; such is the case of the *Brown-Miller* model. The "*Bearings*" region, as it was called, is an area adjacent to the turbine blades that is subject to the highest shift in temperature in the whole component. Proof of this is the result of the gas mapping done in Chapter 5, which shows high values of heat transfer coefficient, especially during heat-up. A callback to this notion is presented in Figure 70.

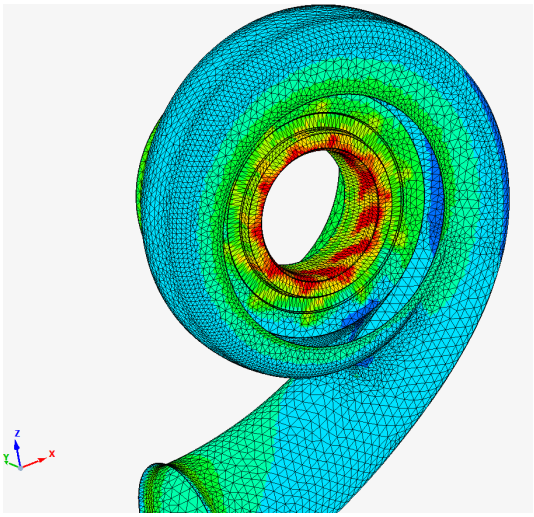

Figure 70: The "Bearings" region is characterized by high values of HTC, therefore heat exchanges are more substantial.

It is therefore possible that an area that is subjected to thermal expansion to such a degree is also influenced by the simplification of this model. The rest of the chapter is therefore dedicated to improving the base model to try to obtain more accurate results.

8.2 Influence of Model Improvements

With numerical results readily available, it is now possible to apply some of the changes proposed in Chapter 5 and evaluate the quality of said results when compared to the target and with each other. The purpose of this study is to evaluate a reasonable trade-off between more accurate results and low computational cost. For each case, said aspects will be discussed by comparing data and a verdict on the feasibility of each upgrade will be given.

8.2.1 Model Improvements and Heat Transfer Coefficients

The main strength of the first mesh geometry used for the thermo-structural analysis is the fact that, compared to the complete design that includes air intake manifold, the engine block, turbo and after-treatment with every accessory included, it provides a faster way to simulate the original analysis that produced the *2019 TFAT results* that are used here as validation targets. There is however a trade-off between performance and fidelity, coming from the fact that in this simplified model more than 90% of the elements are not included. Boundary conditions and the influence of nearby elements are necessarily different from those imposed in the 2019 analysis and this is a limitation that has to be taken into account. It is reasonable to assume, however, that not all components have a significant influence on the Turbocharger itself, due to lack of proximity between the parts. This allows the exploration of further options to try and improve the accuracy of the model without sacrificing computation time. By comparing the results of this new analysis with the result of the thermal analysis from 2019, it is then possible to verify that the results resemble each other in order to have a proper setup for the subsequent structural analysis.

The first change includes **modifications to the base model**, and it brings several changes. The cylinder head block has now been extended to better represent constraints and mitigate the effect of their proximity to the turbocharger. Also a few elements of the after-treatment have been included to better simulate boundary conditions and contact among elements. Boundary conditions have been adjusted

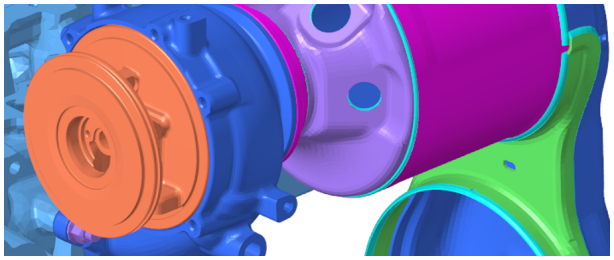

Figure 71: The New Model includes additional bordering components.

accordingly, once again granting radial displacement while imposing an axial constraint. A complete thermo-structural analysis has therefore been conducted with this new model applied.

The second change is in regards to the temperature field along the surface of the component. By comparing the result of this thermal analysis with the one from the *2019 report* notable differences have been observed in the region previously identified as "*Upper and Lower Bearings Region*", that being the region adjacent to the rotor

blades of the turbocharger. It was observed that the minimum temperature in this region was lower compared to the same region in the *Target 2019 analysis*, while peak temperatures seem always accurate. It is not possible to define with absolute certainty what the primary cause of this discrepancy is, however, it is reasonable to assume that the cause resides in the simplification of the model compared to the entire engine. In fact, even if the input CFD analysis is the same, the geometry of the entire assembly, its boundary conditions and the influence of nearby components are different. The absence of certain elements compared to the target analysis likely caused certain areas of the component to reach lower temperatures during cool-down. The same thing applies to the "original" model, but to a higher degree due to the model being even simpler. A practical solution to this issue was found by isolating the interested region and modifying the heat transfer coefficients contained in the input files of the analysis.

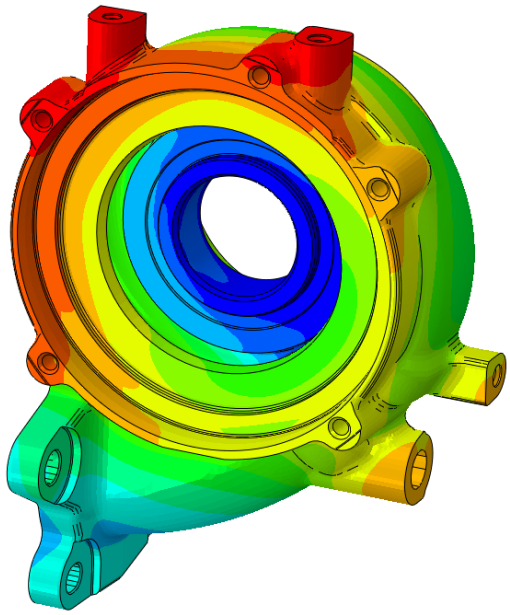

Figure 72: Temperature field in the original model.

This way, the following structural analysis can compute results obtained from a temperature field that more closely resembles the target one, regardless of how this result was achieved. Although partial, this is a simple solution to produce a reliable structural analysis that better reflects the one from the target.

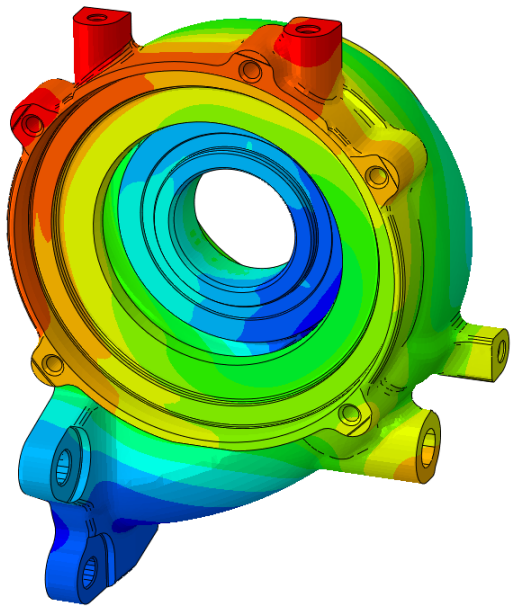

Figure 73: Temperature field in the modified model (new HTC).

Figure 74 compiles numerical results. At first glance, it is possible to observe and comment on the differences with the previous modrl. Most nodes saw differences in the fatigue life results that are evident but not significant in the scope of thermo-mechanical fatigue analysis. That is the case for node E where values are shifted by around 10% at the most, which seems to confirm that the node is to be considered safe.

The main difference is found in the node A, tongue region, and nodes C and D in the internal region adjacent to the rotor blades.

- **Upper and Lower Bearings Region (C and D)** saw the most interesting result. The combined effect of an improved model and a temperature range that resembles the target analysis more closely, caused the results of the structural analysis to be impacted in a way that effectively reduces the strain range in said region. This inevitably produces higher values of fatigue life cycles compared to the previous case. *Brown-Miller* showcases this in an effective manner. This is coherent with our target results, where the *Upper Bearings* node is significantly safer than the *Tongue Region* and closely followed by the *Lower Bearings Region*. Considering that such results have been computed starting from a thermal analysis that is now more representative of the actual target, this is an

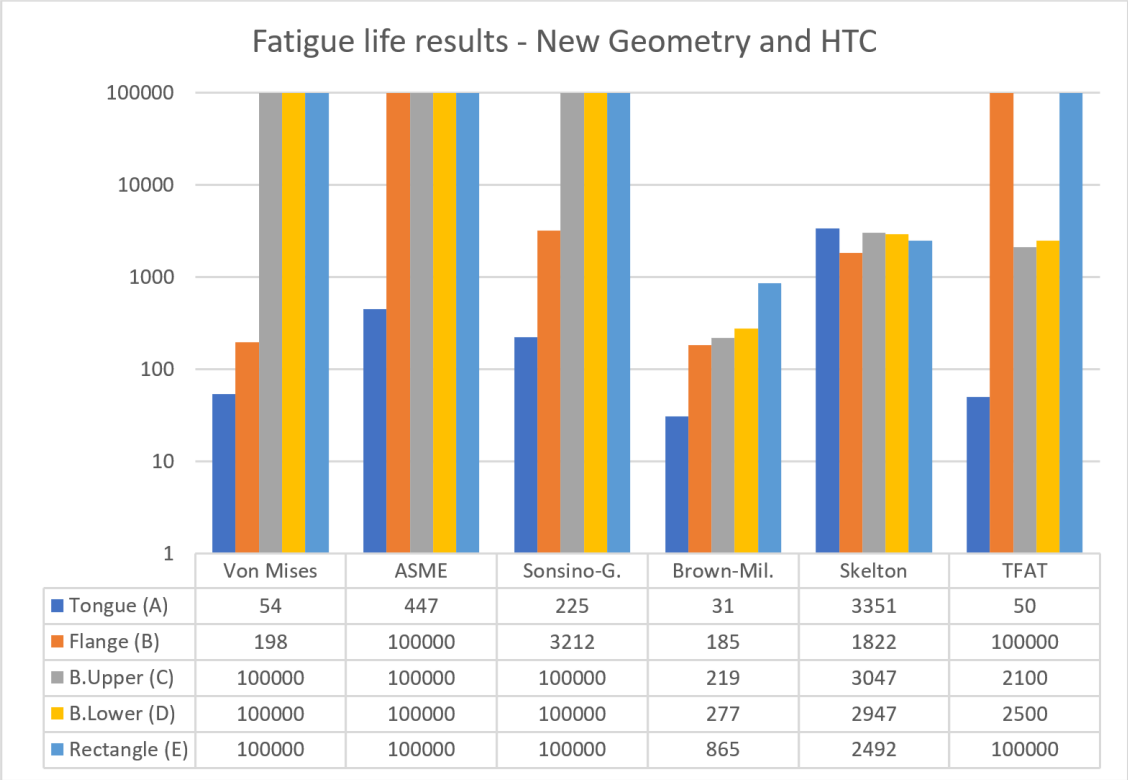

	Von Mises	ASME	Sonsino-G.	Brown-Mil.	Skelton	TFAT
Tongue (A)	54	447	225	31	3351	50
Flange (B)	198	100000	3212	185	1822	100000
B.Upper (C)	100000	100000	100000	219	3047	2100
B.Lower (D)	100000	100000	100000	277	2947	2500
Rectangle (E)	100000	100000	100000	865	2492	100000

Figure 74: Numerical results after changes are applied.

encouraging outcome, showing that results are pointing towards the targets as we introduce improvements that more closely resemble the *2019 target analysis*. For this reason, these changes will be adopted and used as standard for the next steps of the study.

- **Tongue Region (A)** also shows positive results. Not only it remains the critical region of the model, but the number of cycles computed with *Von Mises* and *Brown-Miller* decrease compared to the base model to the point of almost exactly replicating the target values.

Despite the tongue region being partly affected by the change in temperature fields, it saw a decrease in fatigue life cycle while the **C** and **D** nodes which saw an increase. Both these results are coherent compared to the target. This shows that the changes applied were effective in replicating target results, and the effort to more closely resemble the target analysis is proving beneficial. Data is more accurate, but the

general result was unchanged. Nodes that were critical with the previous approach remained critical as well as safer nodes remained safe.

The increase in the number of elements also influenced computation time, in a way that is still manageable in the usual workflow but noticeable and not negligible: This introduces a trade-off between a more accurate and complete analysis and an

Table 3: Focus on fatigue life results for the Tongue Region, with the introduction of the New Model

A: Tongue R.	V. Mises	ASME	Sonsino	B. Miller	Skelton	time [h]
Original Model	121	548	358	126	2220	$2 + 8$
New Model	54	447	225	31	3351	$3 + 9$
Time Discr.	-	-	-	-	-	-
Submodel	-	-	-	-	-	-

increasing computation time that can severely affect the workflow of the analysis engineer. As it was shown, however, it is often worth investing more time to prevent excessive simplification which in turn produces uncertain or misleading results.

8.2.2 Increasing Number of Time Intervals

The next step in improving model accuracy is selecting a certain number of time intervals that provide better results at the cost of higher computation time. The necessity for this reasoning comes from the inner workings of this type of analysis. A *Finite Elements Analysis* requires a discretization in space for stationary conditions and a time discretization for transient states. The solver computes not only at every element of a mesh but also for every time interval. Therefore, the accuracy of a transient analysis is dependent on the number of time intervals present. More intervals provide more uniform data over time but require more processing power. This becomes particularly important in this case study, where results are particularly sensitive to changes to the average temperature of the stabilized cycle. A distribution of time intervals not suitable for the case study could significantly impact said values and introduce a certain degree of uncertainty to the results.

The solution implemented here is to significantly increase the amount of time intervals included in the analysis. It must be noted that this is not standard procedure; despite advantages, this choice can increase computation time significantly in a way that is often not compatible with the user workflow. This should be however interpreted as a one-time experiment aimed at obtaining more precise results and evaluate cost and benefits if this is ever applied in a real scenario.

In order to modify the number of time increments the launch file for the thermal and structural analysis should be edited. In the previous case, the analysis was launched with a set frequency. It means that the thermal analysis will produce a result for every time instant where there is a significant change in gradient. It means that the solver will compute data for thermal analysis only at specific time instants and the structural analysis will acquire them and interpolate said values if necessary. The frequency setting only samples those specific time instants. For example, setting the frequency as 5 makes it so the solver only samples every 5 increments. Therefore, the Temperature-Time graph interpolates a certain amount of time instants which are not equally spaced. This helps reduce computation time as increments are smaller where the temperature gradient is higher and vice-versa. However, for our specific application, this approximation can cause issues, especially if certain parts of the curve have larger increments compared to others.

A first solution could be to increase the number of increments by modifying the number associated with the command. By setting the value to 2 the solver will sample every 2 increments and increase the density of points in time. The number of intervals or "*frames*" increases. However, it was observed that for time intervals where temperature increases steadily the intervals are still too large for our purpose.

An alternative is to set equally spaced increments by defining time intervals so that the solver will sample and interpolate values at pre-defined time instants. Intervals of **2 seconds** have been defined and the analysis produces a transient analysis where results are computed at a uniform time discretization. This is beneficial to certain models that require a comparison between temperature at a certain instant in time and a threshold temperature, such as the proposed "*Taira*-inspired" model for estimating equivalent temperature. The resulting temperature trend over time is represented in the Figure 76 compared to the original discretization in Figure 75.

Having an equally spaced distribution of temperature over time ensures that the equivalent temperature is representative of the reality and allows for a more accurate representation of material properties. The same applies to stress and strain, that are equally computed at every time instant.

With this in mind, thermal and structural analysis are once again executed, and results are acquired and used in the script. Numerical results are compiled in Figure 77:

This change produces differences in the results which are to be considered more accurate. This, however, came at the cost of much higher computation cost. This can vary depending on the system, but it was observed that increasing the number of increments from 32 to 250 resulted in an increase in computation time by at least 4 times as seen in Table 4.

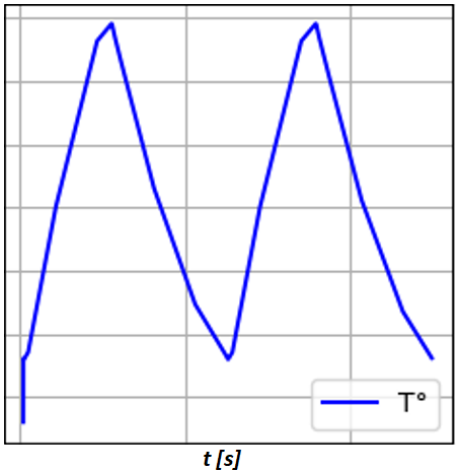

Figure 75: Temperature over time with a discretization with set frequency 5.

This computation time can be prohibitively high, especially for more complex models and therefore this level of detail is not compatible with the requirements of an analysis engineer. However, for this case study, a one-time analysis is useful to produce more accurate results for the comparison with the target values.

Table 4: Focus on fatigue life results for the Tongue Region, with the introduction of the new Time Discretization

A: Tongue	V. Mises	ASME	Sonsino	B. Miller	Skelton	time [h]
Original Model	121	548	358	126	2220	$2+8$
New Model	54	447	225	31	3351	$3+9$
Time Discr.	45	304	161	29	3076	$8+30$
Submodel	-	-	-	-	-	-

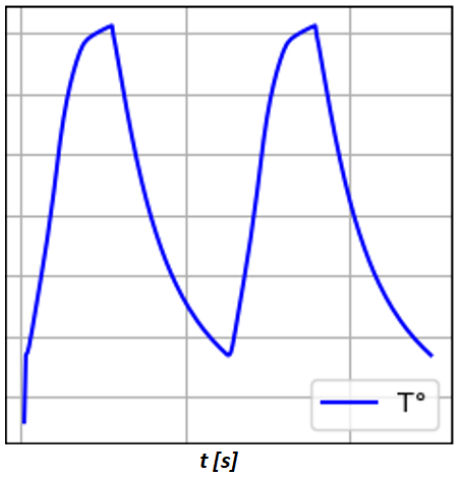

Figure 76: Temperature over time with a discretization with set time intervals 2s.

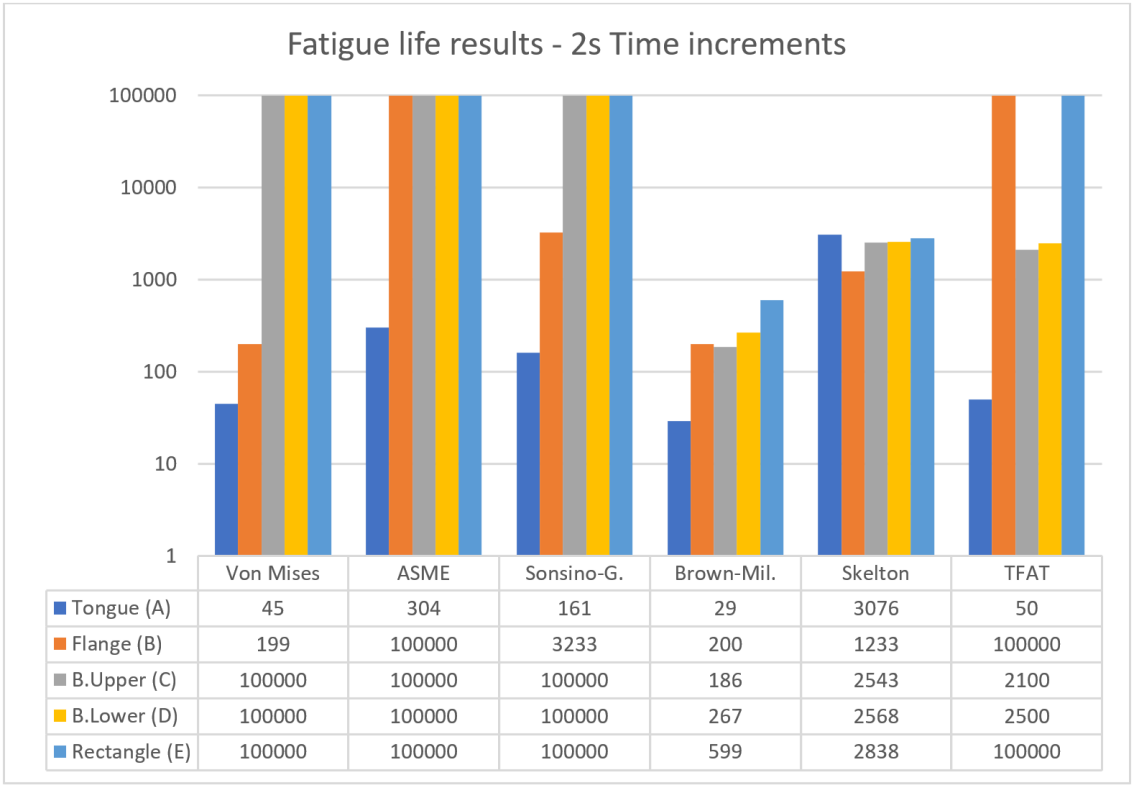

	Von Mises	ASME	Sonsino-G.	Brown-Mil.	Skelton	TFAT
Tongue (A)	45	304	161	29	3076	50
Flange (B)	199	100000	3233	200	1233	100000
B.Upper (C)	100000	100000	100000	186	2543	2100
B.Lower (D)	100000	100000	100000	267	2568	2500
Rectangle (E)	100000	100000	100000	599	2838	100000

Figure 77: Numerical results after changes in time intervals.

8.3 Node Mapping and Data Scatter

To conduct an accurate analysis, it is necessary that all points located in a certain region produce similar values of fatigue life cycles, to prevent arbitrary fluctuations in result depending on user choice. A further study has been conducted in order to verify that all nodes located in a certain region produce results that do not differ excessively among each other.

The way this study was conducted was no different from the standard procedure followed so far, with the only exception being that the nodes selected, and the data exported is relative to several nodes in the same region instead of a single node from different regions. An example is presented in Figure 78, where several points in the same region have been selected in order to produce a node map with a certain spread in fatigue life values. The purpose is to observe if a data spread is present in certain areas of the component and if it is necessary to take action to prevent unwanted fluctuations with results.

Data has been collected for 8 different nodes in each region and a scatter graph was

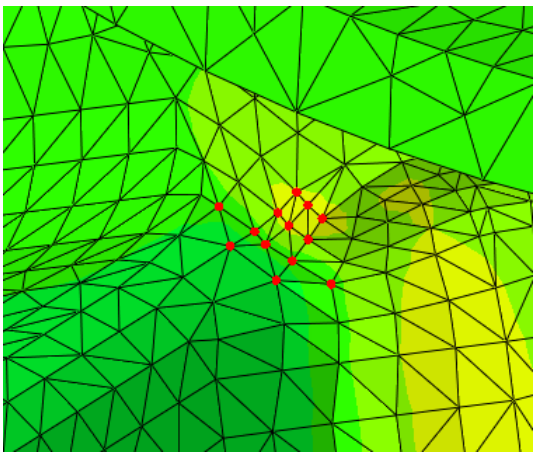

Figure 78: The selection of nodes in a particular region creates a "node map" of the region.

used to compare the spread of values. Among all models, *Brown-Miller* has been chosen as a reference model to conduct the test, as it produced the most conservative results of all the models proposed, allowing us to appreciate even smaller differences of life cycles even in non-critical points. Results have been gathered for each region analysed and they have been detailed in Figure 79.

It is evident that the region that is causing issues is the *Flange Region (B)* where nearby nodes produce different results as they are characterized by varying values of

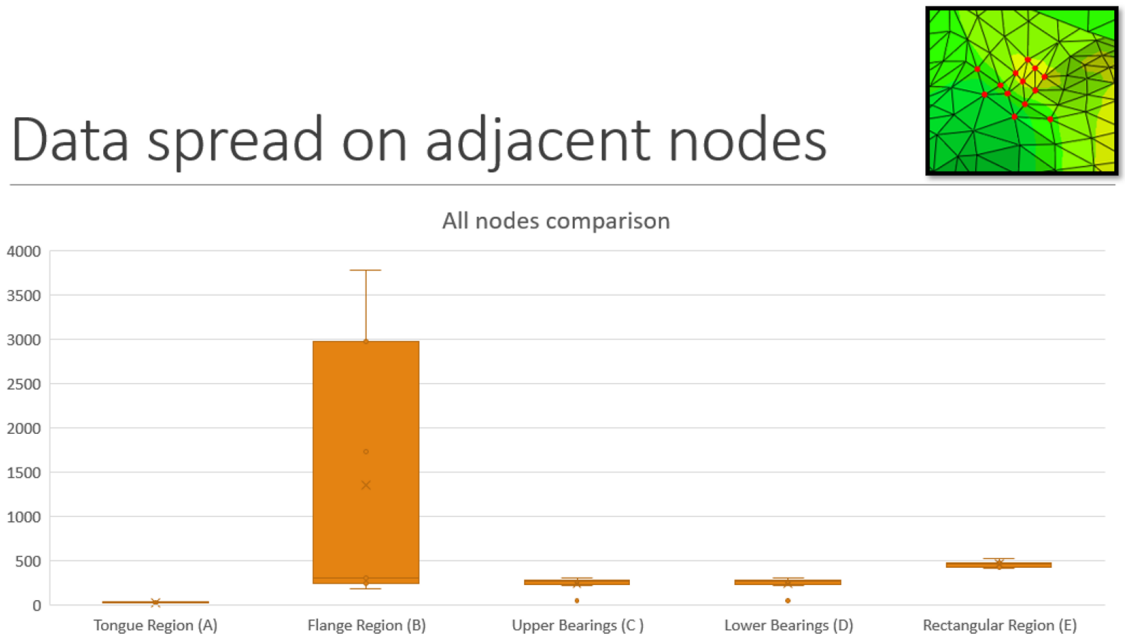

Figure 79: Data spread of node maps in different regions.

strain in the area surrounding the notch. Points that are further from the "core" of the region tend to produce higher values of fatigue life. This could be due to different factors, one of them being spikes or outliers in areas characterized by a complex geometry or, in this case, a notch.

To prevent this, a proposed solution was to create a **submodel** of the flange region with higher density of meshes. This required some extra work with the launch files and the mesh geometry of the component. This approach was introduced in Chapter 5 as a useful method, employed in the industry, to conduct more accurate local analyses with higher mesh density, without impacting computational cost. In practice, the work done during this thesis included extracting the *flange region* and a small surrounding volume from the complete mesh geometry by masking excess elements, closing the geometry so that the new model represents an enclosed volume, increasing local mesh density and launching a structural analysis with this new reduced model labelled as a *Submodel*.

What the solver does is use the results from the previous structural analysis, that includes all data regarding the complete model, and apply known displacements at the borders of the *submodel* as boundary conditions. Stresses and Strains are then computed as normal and an "*.odb*" file is returned. This can then be used once again

in the post-processer to extract data.

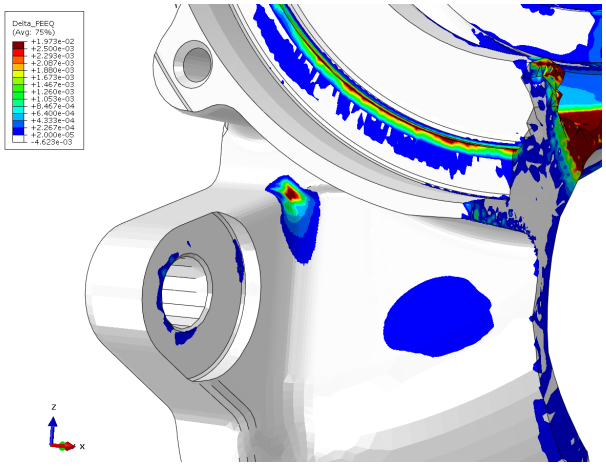

Figure 80: Detail of the *Submodel* extracted from the component.

In this case, for the purpose of this study, 8 nodes have been selected in the flange region of the *Submodel*, in the vicinity of the point that recorded the highest amount of "*Delta-PEEQ*", or variation of plastic equivalent strain. The script then acquires said results and returns fatigue life cycles at every point. It is now possible to make a direct comparison between these two sets of nodes and observe data spread in Figure 81.

It is evident that increasing mesh density heavily mitigates the issue, as a higher node density allows the user to select different nodes inside the critical area of a region and reduces the consequences of choosing different nodes. The minimum value among all nodes remains approximately the same, but the effect of committing human error in the choice of a node has been mitigated, although not entirely removed. In retrospect, this result also possibly explains the outlier in the value of cycles observed in the original model, where the *Brown-Miller* model predicted 3690 cycles to failure, well above the "safe" threshold. It is likely that the node selected in the region corresponds to one of the nodes on the upper half of the spread, although the original "*.odb*" *Abaqus* output file was no longer available to verify this suspicion.

This study demonstrates that, in components that are characterized by notches with a particularly complex shape, results become quite sensitive to user error and could potentially produce inaccurate results. It is therefore recommended that users conduct further analysis in area of this kind, in order to identify the point of minimum fatigue life in a region characterised by complex geometry. In extreme cases, if spikes in values are detected, working on mesh density represents a reliable solution although

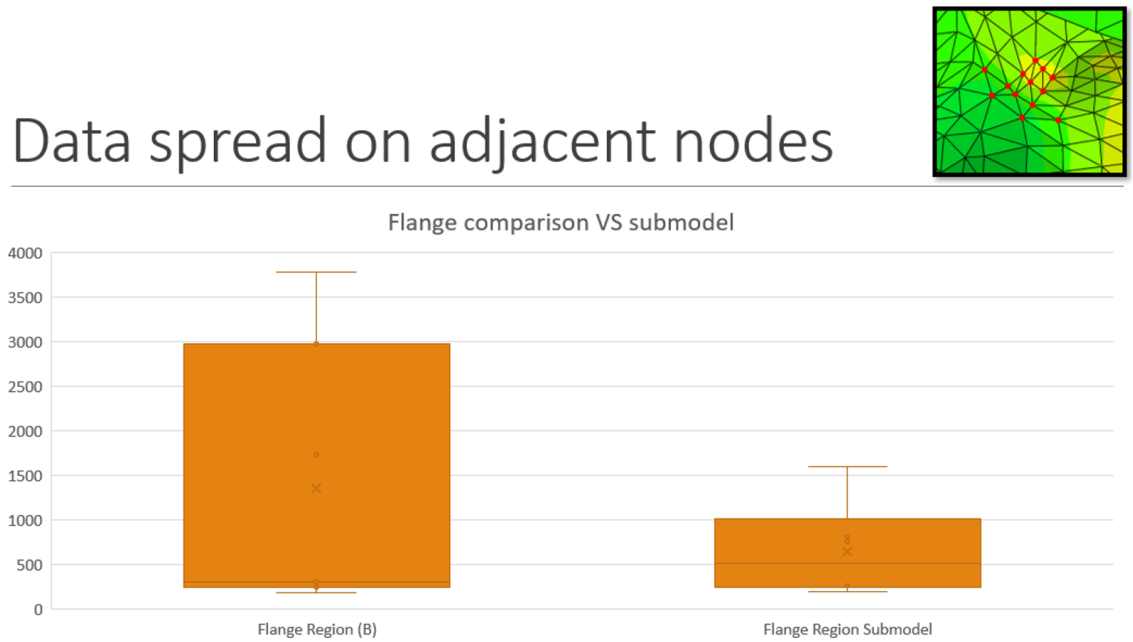

Figure 81: Data spread comparison between base model and *Submodel*.

time consuming. Numerical results that include fatigue life data from the submodel in the *Flange Region* are summarized in Table 5.

Table 5: Focus on fatigue life results for the Flange Region, with *B. Miller* applied to the *Submodel*

B: Flange	V. Mises	ASME	Sonsino	B. Miller	Skelton	time [h]
Original Model	181	∞	2779	3690	2026	$2+8$
New Model	198	∞	3212	185	1822	$3+9$
Time Discr.	199	∞	3233	200	1233	$8+30$
Submodel	-	-	-	193	-	$1+6$

As we can observe, the inclusion of this analysis does not change the minimum value of fatigue life cycles in a certain region significantly, but it is a viable option to reduce uncertainty when operating on components characterized by complex geometry. In this case, the issue could have been solved more easily by simply mapping several nodes in the same region and choosing the lowest value, without creating the *Submodel*. It is however up to the user to decide which case requires such an intervention, depending on their experience and resources available.

9 Conclusions

This thesis work has focused on the development of a simplified finite elements model of a turbocharger volute with the purpose of reproducing the results obtained in a TMF analysis previously conducted at *Dumarey*, here named '2019 Target Analysis', and calibrate the damage models proposed here with the numerical results of the target analysis expressed in terms of fatigue life cycles. As detailed from Chapter 4 to Chapter 8, the process started from the execution of thermo-structural transient analyses and then explored different approaches to fatigue life estimation with the expressed purpose of replicating results obtained by commercial software with results from the *FaLEsPy* Python tool. This chapter draws different conclusions on the quality of the results obtained and evaluates prospects of future developments.

9.1 Comparison

Results have shown that the leading factor that influences the accuracy of a model is the quality of its boundary conditions, which in this case are directly related to the number of components that are in contact or in near proximity to the element of interest. Therefore, the final result that will be used as a point of discussion in this conclusion is the one obtained from the "improved" model, with set time intervals of 2 seconds.

For the sake of brevity, *Von Mises* model and *Brown-Miller* model will be compared with the 2019 target values, as they seemed to provide more information than others. Results are shown in terms of fatigue life cycles, with the exception of the '%PEEQ' method that analyses plastic strains as a percentage; as it is outside the scope of this study, results from this method are simply labeled as 'Safe' or 'Not Safe'. Threshold values (*Thr.*) indicate a number of cycles or a percentage of plastic strain that causes failure according to experience or experimental tests. Results are summarised in Table 6.

Table 6: Fatigue life results in terms of cycles, comparison with targets.

	A:Tongue	**B**:Flange	**C**:Upper	**D**:Lower	**E**:Rect.	Thr.
TFAT	**50**	∞	2200	2500	∞	**2250**
%PEEQ	**Not Safe**	-	Safe	Safe	Safe	**5%**
V.Mises	**45**	199	∞	∞	∞	-
B.Miller	**29**	200	186	267	599	-

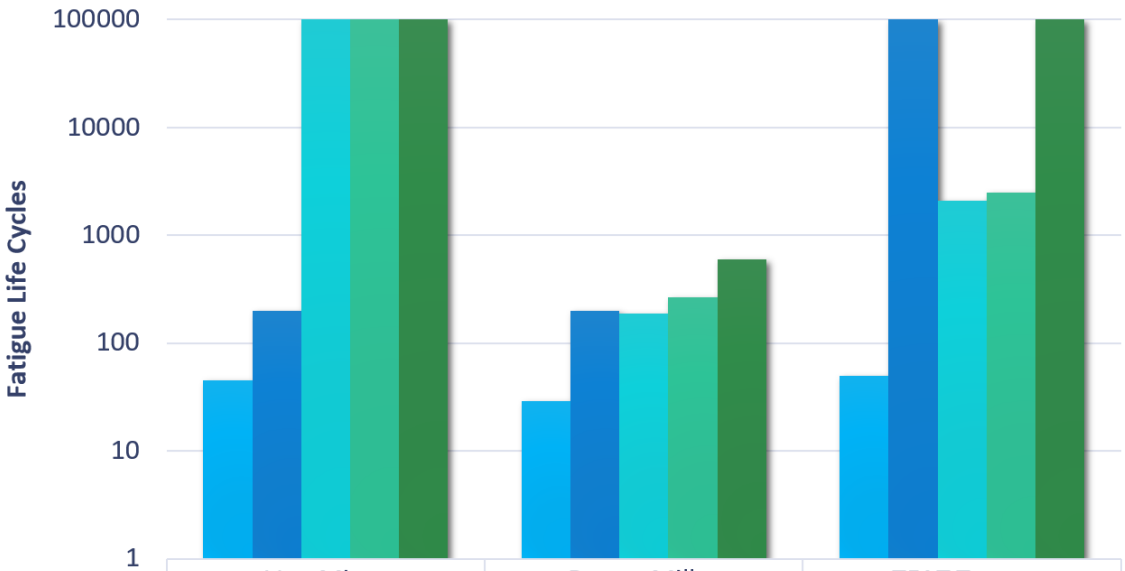

	Von Mises	Brown Miller	TFAT Target
A: Tongue	45	29	50
B: Flange	199	200	100000
C: Upper	100000	186	2100
D: Lower	100000	267	2500
E: Rect.	100000	599	100000

Figure 82: Final fatigue life results in terms of life cycles.

Models behave differently from one another; they do however display similarities as they both succeed in identifying the *Tongue Region* as a potentially critical region. The same cannot be said about other points, where the nuances off each model stand out. *Von Mises* seems to prioritize the *Flange Region*, as it is characterized by higher components oh shear stress and strain that heavily impact equivalent strain. However, it is not capable to identify the Upper *Bearings Region (C)* as critical. The same cannot be said about the *Brown-Miller* model, which not only correctly identifies the *Tongue region*, but also shows more nuance in identifying the *Flange region* and it even underlines the difference between the C and D nodes. This result is in line with the *TFAT target analysis*, where the D region is considered safe but slightly higher that the C region. This is a promising result. Despite showing values well below the target threshold, the *Brown-Miller* criterion seems to replicate the same logic of the *TFAT* analysis.

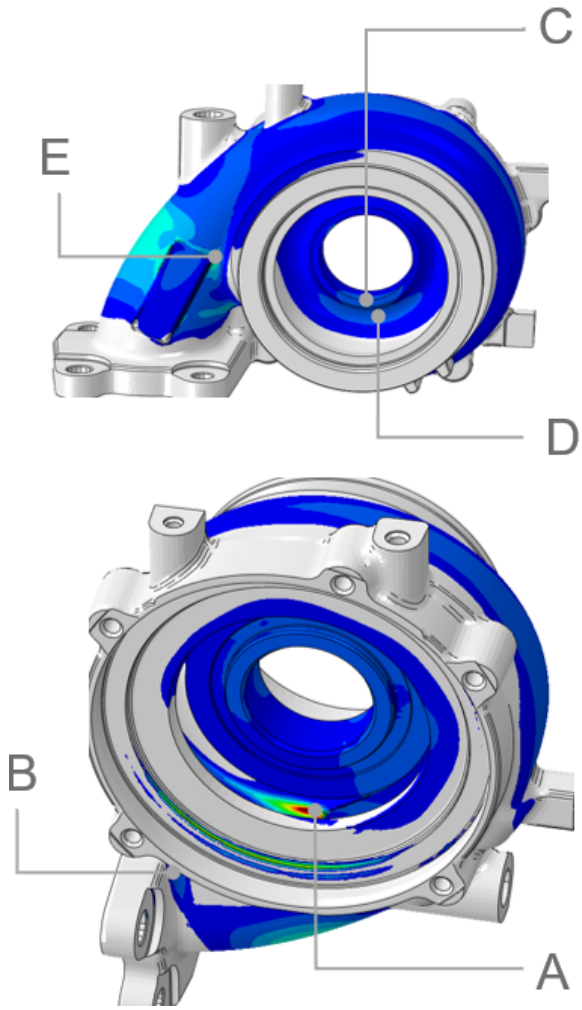

Figure 83: Overview of the different nodes analysed.

Results from *Von Mises* and *Brown-Miller* are isolated in Table 7 and 8 and compared with different model improvements as detailed in Section 8.2 and Chapter 5. Computation time is also indicated in terms of hours elapsed during the analysis from start to end.

Table 7: Fatigue life cycles results at nodes with Von-Mises, for different model improvements introduced in Chapter 5.

Von Mises	**A**:Tongue	**B**:Flange	**C**:Upper	time[h]
Original Model	**121**	181	∞	$2+8$
New Model	**54**	198	∞	$3+9$
Time Discr.	**45**	199	∞	$8+30$
TFAT	**50**	∞	2200	-
%PEEQ	**Not Safe**	-	Safe	-

Table 8: Fatigue life cycles results at nodes with B. Miller, for different improvements introduced in Chapter 5.

B. Miller	**A**:Tongue	**B**:Flange	**C**:Upper	time[h]
Original Model	**126**	3690	83	$2+8$
New Model	**31**	185	219	$3+9$
Time Discr.	**29**	200	186	$8+30$
Submodel	-	193	-	$1+6$
TFAT	**50**	∞	2200	-
%PEEQ	**Not Safe**	-	Safe	-

It is evident that *Brown-Miller*, unlike any other criterion showcased in this work, displays results in an entirely different range of values, those being comprised between 29 cycles of the *Tongue Region* and around 600 cycles of the *Rectangular Region*. Such values are significantly lower than the validation targets used in TFAT, however they should not be discaded as incorrect. The focus for future studies and validation should be set towards calibrating the model in a way that allows the user to identify a correct threshold value representative of failure. As an example, a possible threshold value for *Brown-Miller* with regards to the results obtain in this work might be set between 200 and 400 cycles. At this point in time the choice is almost arbitrary, but future validations with different components and threshold values should allow the user to pinpoint a precise threshold value of cycles specific to this model.

Computational cost is another topic that is worth discussing briefly. The charts compare the time roughly required for each method to complete an analysis comprised of both thermal and thermo-structural parts. It is intuitive to grasp how an increase in complexity increases computational cost, with the benefit of more accurate results. Not all methods are, however, equal.

The use of a *Submodel* is quite common in the industry, and it is often deemed necessary for an in-depth analysis of an issue with a component design. Thus, even if in this case differences seem negligible, the usefulness of this tool should not be discarded. The downside is however the requirement not only of computational resources but manual input from the user, who is required to modify the geometry and increase mesh density. Therefore, the use of this method and its usefulness is the result of a case-by-case study.

The method that proved to be the most detrimental in terms of computational cost is the increase in the number of *time increments*, which marginally improved results but required more than an entire day to just produce a structural analysis. This is potentially incompatible with the workflow of an analysis engineer, especially if potential issues which might require a restart are taken into account. Obviously, the case presented here represents an extreme, where intervals have been determined for every two seconds (alternatively, setting a lower value of frequency such as 1 is a possible approach). It is possible to find a compromise between accuracy and cost, but it would require further testing. For the moment, it can be assumed that the standard frequency of 5 (indicating that the solver produces a single result every 5 increments) used in the default analysis is accurate enough to be suitable for this type of study.

Having a more accurate representation of the complete models remains the best approach for this type of analysis, and this study proved that representing the assembly in a complete manner should be the priority. It must be noted that this is often the case in the industry: in fact, the *2019 target analysis* conducted using *TFAT* was done on a complete assembly that includes all engine components. The only reason that the current model was reduced to a few components was to fit the scope of the thesis, due to limitations in the resources available. With this in mind, it is possible to draw some conclusions on the results of this work.

The last point to discuss is in regards to the estimation of *equivalent temperature* for the isothermal LCF cycle. As was previously discussed, the necessity for a single value of equivalent temperature required the choice among different methods of equivalent temperature estimation, ranging from a simple mean temperature to the proposed *Taira*-Based model presented in Chapter 3. All methods proposed did not completely alter the main result of the analysis, but numerical values saw significant differences, with certain methods producing more conservative results compared to others. Among all, only the *Taira*-Based method was used here as it provided results that better resonated with the target values. Although seemingly arbitrary, it should be noted that the spirit of this comparison is to calibrate the different models with the purpose of replicating the target results. The number of cycles in the tongue region

was used as the main target, and the *Taira*-based method proved to be slightly more accurate compared to others; only numerical values from this method were presented here, to avoid polluting the results with an excessive amount of data. Therefore, the choice of this method is coherent with the main purpose of this specific comparison. It should be noted that this path does not invalidate other methods for equivalent temperature estimation, but further validation tests are required to support their relative usefulness to this type of analysis.

9.2 Verdict

To give perspective on the quality of the results it is important to understand the purpose of this tool and the scope of its use. The main objective of this script developed in *Python* is to provide the user with a tool for a first-try thermo-mechanical analysis applied on certain nodes of a component. Applying damage models designed to work with constant temperature with an almost entirely analytical approach requires accepting a certain level of uncertainty with fatigue life results; however, numerical data proves that this method is a viable approach for situations where very few information is available about the material and the component, and it proves itself especially accurate when it comes to identifying leading failure points. Although models based on experimental data are significantly more accurate and are capable to capture the nuances of different potentially critical point, as well as involve phenomena like creep and oxidation, experimental campaigns are not often available and, if they are, they involve added expenses aimed at obtaining the required data.

This works then serves two main purposes. First, from an industry perspective, it serves as a benchmark for upcoming thermo-mechanical analyses and a tool that aids the workflow of an analysis engineer. Second, it serves as a comparison to further study the use of analytical methods and their viability compared to models based on experimental data. Results show that different models behave quite differently from one another, however they almost always succeed in identifying the leading failure points, although often describing different amounts of fatigue life cycles. That is the case of the *Brown-Miller* criterion, an often conservative model, that in this case study proves particularly conservative in its results. However, if we choose to focus on the relative proportion of fatigue life results rather than the absolute values compared to the target analysis, it gives useful information on how certain critical points behave compared to one another. This result, although interesting, requires further validation on different components in order to define a threshold value that works for the *Brown-Miller* criterion.

Most models showcased in this work show the similarity of being able to effectively

identify the single most critical point of the component, that being the *Tongue Region* located in the internal surface of the turbo volute. The usefulness of this result should not be understated given the scope of this tool, as it proves that, despite limitations, it is effective in providing immediate feedback on a certain point of interest of a component, without resorting to experimental campaigns or time-consuming analyses.

In regards to the *FaLEsPy* tool, it represents a very useful element in the workflow dedicated to thermo-mechanical analysis. It places itself after the completion of the structural analysis for a new component and it serves the purpose of immediately help identify design changes to implement before proceeding with more sophisticated and time-consuming tools. With a simple and intuitive interface and an integrated guide on its use, it allows for immediate results provided that input data are correctly formatted. The time required from the completion of the thermo-structural analysis to the final fatigue life estimation is around 15-30 minutes depending on the user, most of which is spent on post-processing in *Abaqus Viewer*.

In conclusion, the results obtained are encouraging. The simplification of complex phenomena with an analytical approach has surely shown weaknesses related to its inaccuracy when trying to capture the nuances of complex phenomena, but at the same time has proved to be capable to replicate target results where it most matters, that being the identification of failure points. This tool has shown to be capable to distinguish safe region from the ones that have the potential to nucleate fatigue cracks. The tool's capabilities and the way it is designed allow for easy implementation of further upgrades and it benefits its future prospects. The main trait of being characterized by almost entirely analytical models could be overcome in the future by implementing more complex damage models that incorporate experimental data, extending the horizons of possibilities for future applications.

References

[1] et al. Laengler Frank. "Investigation of Application-Specific Phenomena to Improve the Lifetime Assessment for Turbine Housings of Turbochargers." In: *Procedia Engineering* 10 (2011), pp. 1163–1169 (cit. on pp. 3, 11).

[2] et al. Borges M.F. "Effect of Kinematic Hardening Parameters on Fatigue Crack Growth." In: 106 (Apr. 2020), p. 102501 (cit. on pp. 4, 5).

[3] Gary Halford. *Low Cycle Thermal Fatigue*. Technical Memorandum. NASA, 1986 (cit. on p. 5).

[4] et al. Mahmoudi A. H. "An Application of Chaboche Model to Predict Uniaxial and Multiaxial Ratcheting." In: *Procedia Engineering* 10 (Jan. 2011), pp. 1924–1929 (cit. on p. 5).

[5] Andrea Vercelli. "Design Methodologies for High Temperature Low Cycle Fatigue of Engine Components". PhD thesis. Politecnico di Torino, Apr. 2011 (cit. on pp. 9, 23, 26, 34).

[6] Prof. Thomas Seifert. *Thermomechanical fatigue life prediction methods for high temperature components in combustion engines – Training at GM*. Sept. 2018 (cit. on p. 10).

[7] et al. Su X. "Thermal Fatigue Analysis of Cast Aluminum Cylinder Heads." In: *SAE Transactions* 111 (2002), pp. 418–424 (cit. on p. 22).

[8] M. W. Brown and K. J. Miller. "A Theory for Fatigue Failure under Multiaxial Stress-Strain Conditions." In: *Proceedings of the Institution of Mechanical Engineers* vol. 187 (June 1973), pp. 745–755 (cit. on p. 25).

[9] T. Vilhelmsen R. P. Skelton and G. A. Webster. "Energy criteria and cumulative damage during fatigue crack growth." In: *International Journal of Fatigue* vol. 20 (Oct. 1998), pp. 641–649 (cit. on p. 26).

[10] Cristiana Delprete and Raffaella Sesana. "Proposal of a New Low-Cycle Fatigue Life Model for Cast Iron with Room Temperature Calibration Involving Mean Stress and High-Temperature Effects." In: *Proceedings of the Institution of Mechanical Engineers, Part C: Journal of Mechanical Engineering Science* vol. 233, no. 14 (Mar. 2019), pp. 5056–5073 (cit. on pp. 28, 89).

[11] S.S. Manson., ed. *Thermal stress and low cycle fatigue.* New York, NY, USA: McGraw-Hill Press., 1966 (cit. on p. 29).

[12] S. Taira, ed. *Relationship between thermal fatigue and low-cycle fatigue at elevated temperatures.* West Conshohocken, PA, USA: In: Fatigue at elevated temperatures, edited by Carden A. E. McEvily, A. J. and Wells. ASTM STP 520, ASTM International. p. 80-101, 1973 (cit. on p. 34).